

ULTRAWIDEBAND - ULTRAWIDEBEAM SYNTHETIC APERTURE RADAR SIGNAL PROCESSING AND APPLICATIONS

Viet Thuy Vu

Blekinge Institute of Technology
Doctoral Dissertation Series No. 2011:13
School of Engineering



**Ultrawideband-Ultrawidebeam
Synthetic Aperture Radar
Signal Processing and Applications**

Viet Thuy Vu

Blekinge Institute of Technology doctoral dissertation series
No 2011:13

Ultrawideband-Ultrawidebeam Synthetic Aperture Radar Signal Processing and Applications

Viet Thuy Vu

Doctoral Dissertation in
Applied Signal Processing



School of Engineering
Blekinge Institute of Technology
SWEDEN

2011 Viet Thuy Vu

School of Engineering

Publisher: Blekinge Institute of Technology,
SE-371 79 Karlskrona, Sweden

Printed by Printfabriken, Karlskrona, Sweden 2011

ISBN: 978-91-7295-219-5

ISSN 1653-2090

urn:nbn:se:bth-00512

Abstract

This dissertation presents practical issues in Ultrawideband - Ultra-widebeam (UWB) Synthetic Aperture Radar (SAR) signal processing and crucial applications developed on UWB SAR. In the context of this dissertation, UWB SAR refers to the SAR systems utilizing large fractional bandwidth signals and synthesizing long apertures associated with wide antenna beamwidths. On one hand, such specific systems give us opportunities to develop unique applications. On the other hand, signal processing for data collected by these systems is very challenging and therefore requires much effort due to their characteristics. The research results presented in this thesis are divided into two parts: signal processing and application.

In the signal processing part, the tools supporting the UWB SAR system design and evaluation are introduced. They include an Impulse Response Function in UWB SAR imaging (IRF-SAR), azimuth and range resolution equations for UWB SAR, and a definition of UWB SAR quality measurements. Pre-processing, processing and post-processing for UWB SAR are also topics that will be examined in the signal processing part. The processing is here defined by SAR algorithms. With this definition, the pre-processing refers to RFI suppression approaches whereas the post-processing implies apodization or sidelobe control methods.

In the application part, Ground Moving Target Indication (GMTI) is selected for study due to its interest to both military and civilian end-users. The GMTI technique developed for UWB SAR relates to the moving target detection by focusing technique which can be combined with the space-time processing such as Displaced Phase Center Antenna (DPCA) and Space-Time Adaptive Processing (STAP).

Preface

This dissertation summarizes my studies within the field of Ultrawideband-Ultrawidebeam Synthetic Aperture Radar - Signal Processing and Applications. The work has been performed at the Department of Electrical Engineering, School of Engineering, at Blekinge Institute of Technology, Karlskrona, Sweden. The CARABAS-II and LORA data provided by the Swedish Defence Research Agency (FOI) have been mainly employed in the research works. The dissertation consists of three main parts and each main part is divided again into subsections:

Part I - Tools for UWB SAR System Design and Evaluation

- A** An Impulse Response Function for Evaluation of UWB SAR Imaging.
- B** On Synthetic Aperture Radar Azimuth and Range Resolution Equations.
- C** Definition on SAR Image Quality Measurements for UWB SAR.

Part II - UWB SAR Data Pre-processing, Processing and Post-processing

- A** RFI Suppression in Ultrawideband SAR Using Adaptive Line Enhancer.
- B** A Comparison between Fast Factorized Backprojection and Frequency-Domain Algorithms in UWB Low Frequency SAR.
- C** On Apodization Techniques for Ultra-wideband SAR Imaging.

Part III - Applications of UWB SAR

- A** Detection of Moving Targets by Focusing in UWB SAR – Theory and Experimental Results.
- B** Fast Detection of Moving Targets by Focusing in UWB Low Frequency SAR.
- C** Integrating Space-Time Processing into Time-Domain Backprojection Process to Detect and Image Moving Objects.

Acknowledgments

It is a pleasure to thank those who made this thesis possible. First of all, I would like to thank Dr. Sven Johansson, Prof. Hans-Jurgen Zepernick and Prof. Mats Pettersson for giving me the opportunity to be a PhD candidate at Blekinge Institute of Technology. I acknowledge the help that I got from my supervisor Prof. Hans-Jurgen Zepernick, especially at the beginning of my research, and kind support throughout this dissertation work. I owe my deepest gratitude to my supervisor Prof. Mats Pettersson for his continuous guidance. He has made available his support in a number of ways. Without his knowledgeable supervision, it would not have been possible to bring this dissertation to an end. I would like to show my gratitude to my colleague Thomas Sjögren for the helps, the knowledge and experience sharing. It is an honor for me to thank the KK-Foundation for financing this research project, the Swedish Defence Research Agency, Saab Bofors Dynamics, Saab Electronic Defence Systems and RUAG Space for their cooperation. I am indebted to my former and present colleagues at the Department of Electrical Engineering for the necessary assistance and for providing a great work atmosphere. I highly appreciate the students for their collaboration in the research projects.

Let me express my hearty gratitude to my parents, Khang Vu and Tua Khieu, my sisters Hai Vu and Phuong Tran, and other family members for their immense support and encouragement. Finally, my warmest thanks go to my wife Van Nguyen for her loving and generous support.

*Viet Thuy Vu
Karlskrona, 8th December 2011*

Publication list

Publications included in this thesis

Part I is published as:

V. T. Vu, T. K. Sjögren, M. I. Pettersson, and H. Hellsten “An impulse response function for evaluation of ultrawideband SAR imaging,” *IEEE Trans. Signal Processing*, vol. 58, no. 7, pp. 3927–3932, 2010.

V. T. Vu, T. K. Sjögren, and M. I. Pettersson, “On synthetic aperture radar azimuth and range resolution equations,” *IEEE Trans. Aerosp. Electron. Syst.*, accepted for publication.

V. T. Vu, T. K. Sjögren, M. I. Pettersson, and A. Gustavsson, “Definition on SAR image quality measurements for UWB SAR,” in *Proc. SPIE Image and Signal Processing for Remote Sensing XIV*, vol. 7109, Cardiff, UK, Sep. 2008, pp. 71091A1–71091A9.

Part II is published as:

V. T. Vu, T. K. Sjögren, M. I. Pettersson, L. Håkansson, A. Gustavsson, and L. M. H. Ulander, “RFI suppression in ultrawideband SAR using adaptive line enhancer,” *IEEE Geosci. Rem. Sens. Lett.*, vol. 7, no. 4, pp. 282–286, 2010.

V. T. Vu, T. K. Sjögren, and M. I. Pettersson, “A comparison between fast factorized backprojection and frequency-domain algorithms in UWB low frequency SAR,” in *Proc. IEEE IGARSS’2008*, Boston, US, Jul. 2008, pp. IV-1284–IV-1287.

V. T. Vu, T. K. Sjögren, and M. I. Pettersson, “On apodization techniques for ultra-wideband SAR imaging,” in *Proc. EURAD’2009*, Rome, Italy, Sep. 2009, pp. 529–532.

Part III is published as:

V. T. Vu, T. K. Sjögren, M. I. Pettersson, A. Gustavsson, and L. M. H. Ulander, “Moving targets detection by focusing in UWB SAR - Theory and

experimental results," *IEEE Trans. Geosci. Remote Sensing*, vol. 48, no. 10, pp. 3799–3815, 2010.

V. T. Vu, T. K. Sjögren, and M. I. Pettersson, "Fast detection of moving targets by focusing in Ultra-wideband SAR," in *Proc. IEEE RadarCon'2009*, Pasadena, US, May 2009, pp. 1–5.

V. T. Vu, T. K. Sjögren, and M. I. Pettersson, "Integrating space-time processing into time-domain backprojection process to detect and image moving objects," in *Proc. IEEE IGARSS'2010*, Honolulu, US, Jul. 2010, pp. 4106–4109.

Other publications

Licentiate dissertations:

V. T. Vu, "Practical considerations in ultrawideband synthetic aperture radar," *Licentiate dissertation*, Blekinge Institute of Technology, Karlskrona, Sweden, Nov. 2009, ISBN 978-91-7295-171-6.

Papers in journals:

V. T. Vu, T. K. Sjögren, and M. I. Pettersson, "Phase error calculation for fast time-domain bistatic SAR algorithms," *IEEE Trans. Aerosp. Electron. Syst.*, revised for publication.

T. K. Sjögren, V. T. Vu, M. I. Pettersson, A. Gustavsson, and L. M. H. Ulander, "Moving target relative speed estimation and refocusing in synthetic aperture radar images," *IEEE Trans. Aerosp. Electron. Syst.*, accepted for publication.

V. T. Vu, T. K. Sjögren, and M. I. Pettersson, "Ultrawideband chirp scaling algorithm," *IEEE Geosci. Rem. Sens. Lett.*, vol. 7, no. 2, pp. 694–698, 2010.

Papers in conference proceedings:

V. T. Vu, T. K. Sjögren, and M. I. Pettersson, "SAR imaging on ground plane using fast backprojection," in *Proc. IEEE RadarCon'2012*, Atlanta, US, May 2012, submitted for publication.

V. T. Vu, T. K. Sjögren, and M. I. Pettersson, “Fast factorized backprojection algorithm for UWB bistatic SAR image reconstruction,” in *Proc. IEEE IGARSS’2011*, Vancouver, Canada, Jul. 2011, pp. 4237–4240.

T. K. Sjögren, V. T. Vu, and M. I. Pettersson, “2D apodization in UWB SAR using linear filtering,” in *Proc. IEEE IGARSS’2011*, Vancouver, Canada, Jul. 2011, pp. 1689–1692.

V. T. Vu, T. K. Sjögren, and M. I. Pettersson, “Space time adaptive processing for moving target detection and imaging in bistatic SAR,” in *Proc. IEEE IGARSS’2011*, Vancouver, Canada, Jul. 2011, pp. 2829–2832.

V. T. Vu, T. K. Sjögren, and M. I. Pettersson, “Fast backprojection algorithm for UWB bistatic SAR,” in *Proc. IEEE RadarCon’2011*, Kansas City, US, May 2011, pp. 431-434.

V. T. Vu, T. K. Sjögren, M. I. Pettersson, and P. A. C. Marques, “Application of moving target detection by focusing technique in civil traffic monitoring,” in *Proc. IEEE IGARSS’2010*, Honolulu, US, Jul. 2010, pp. 4118-4121.

T. K. Sjögren, V. T. Vu, and M. I. Pettersson, “Moving target refocusing algorithm for synthetic aperture radar images,” in *Proc. IEEE IGARSS’2010*, Honolulu, US, Jul. 2010, pp. 4110-4113.

V. T. Vu, T. K. Sjögren, M. I. Pettersson, and L. Håkansson, “An approach to suppress RF interference in Ultrawideband low frequency synthetic aperture radar,” in *Proc. IEEE Radar’2010*, Washington, US, May 2010, pp. 1381-1385.

V. T. Vu, T. K. Sjögren, and M. I. Pettersson, “Fast detection of moving targets by focusing in multi-channel Ultra-wideband SAR,” in *EuRAD 2009*, Rome, Italy, Sep. 2009, pp. 218–241.

V. T. Vu, T. K. Sjögren, and M. I. Pettersson, “Moving target detection by focusing for frequency domain algorithms in UWB low frequency SAR,” in *Proc. IEEE IGARSS’2008*, Boston, US, Jul. 2008, pp. I-161–I-164.

T. K. Sjögren, V. T. Vu, and M. I. Pettersson, “Moving target relative speed estimation in the presence of strong stationary surrounding using a single an-

tenna UWB SAR system," in *Proc. IEEE IGARSS'2008*, Boston, US, Jul. 2008, pp. I-157–I-160.

M. I. Pettersson, V. T. Vu, T. K. Sjögren and A. Gustavsson, "Multi-dimensional hypotheses test of movement detection in wide band radar systems associated with long integration time," in *Proc. Svenska Nationalkommittén för RadioVetenskap*, Väjxö, Sweden, June 2008, pp. (4p).

T. K. Sjögren, V. T. Vu, and M. I. Pettersson, "A comparative study of the polar version with the subimage version of fast factorized backprojection in UWB SAR," in *Proc. IEEE IRS'08*, Wroclaw, Poland, May 2008, pp. 156–159.

V. T. Vu, T. K. Sjögren, M. I. Pettersson, H.-J. Zepernick, and A. Gustavsson, "Experimental results on moving targets detection by focusing in UWB low frequency SAR," in *Proc. IET RADAR'2007*, Edinburgh, UK, Oct. 2007, pp. 562–566.

T. K. Sjögren, V. T. Vu, M. I. Pettersson, H.-J. Zepernick, and A. Gustavsson, "Speed estimation experiments for ground moving targets in UWB SAR," in *Proc. IET RADAR'2007*, Edinburgh, UK, Oct. 2007, pp. 519–523.

Contents

Abstract	v
Preface	vii
Acknowledgments	ix
Publications list	xi
Introduction	1
Part I - Tools for UWB SAR System Design and Evaluation	
A An Impulse Response Function for Evaluation of UWB SAR Imaging	43
B On Synthetic Aperture Radar Azimuth and Range Resolution Equations	65
C Definition on SAR Image Quality Measurements for UWB SAR	83
Part II - UWB SAR Data Pre-processing, Processing and Post-processing	
A RFI Suppression in Ultrawideband SAR Using Adaptive Line Enhancer	103
B A Comparison between Fast Factorized Backprojection and Frequency-Domain Algorithms in UWB Low Frequency SAR	121
C On Apodization Techniques for Ultrawideband SAR Imaging	135
Part III - Applications of UWB SAR	
A Detection of Moving Targets by Focusing in UWB SAR – Theory and Experimental Results	151
B Fast Detection of Moving Targets by Focusing in UWB Low Frequency SAR	197
C Integrating Space-Time Processing into Time-Domain Backprojection Process to Detect and Image Moving Objects	215

Introduction

1 Motivation

Synthetic Aperture Radar (SAR) provides a wide range of applications in geoscience and remote sensing. The ability to operate in severe conditions such as rain, clouds, and darkness is seen to be a major advantage of SAR systems in comparison to other sensor systems. Ultrawideband-Ultrawidebeam (UWB) SAR refers to SAR systems which utilize a large fractional bandwidth signal and a wide antenna beamwidth. The fractional bandwidth is here defined by the ratio of the radar center frequency to the signal bandwidth. The illuminated scene size of a SAR system depends strongly on the swath in elevation while the radar signal bandwidth and the antenna beamwidth associated with the integration angle influence directly the resolution of that SAR system. A large scene size, high resolutions in azimuth (along track) and range (cross track) can therefore be achieved simultaneously with UWB SAR systems. For this reason, important applications of UWB SAR can be found in ground imaging, change detection and large scale observation. There are also other crucial applications of UWB SAR such as Ground Moving Target Indication (GMTI) and motion parameter estimation [1] which are of interest to both military and civilian end-users.

Processing radar echoes collected by a UWB SAR system for different applications is challenging and requires much effort. UWB SAR associated with long integration time usually results in a huge amount of data and very large range migration. For example, the dimensions of the CARABAS-II data matrix can be up to 35840×8192 [2]. Processing such amount of data cannot rely on the commonly used frequency-domain algorithms. Also, real time processing relied on the frequency-domain algorithms is almost impossible. Several practical issues on UWB SAR signal processing were stated for the first time in the 1990's [3], at the same time as the experimental systems CARABAS-II and P-3 were built. The issues mentioned in [3] have been clarified from the

experience with P-3 data processing. They refer to choice of algorithm, coherent integration angle, apodization or sidelobe control, motion compensation, Radio Frequency Interference (RFI), and auto-focus. There are also new issues such as Impulse Response Function in SAR Imaging (IRF-SAR), spatial resolution equations and image quality assessments which have been recently discovered during the measurements on the CARABAS-II data in practice. These issues have been presented in some publications and they are summarized in [4]. However, there might be other issues which are unknown and that may only appear in certain cases. According to the author's knowledge, practical issues on UWB SAR signal processing and approaches for them still remain an active area of research.

In this dissertation, newly introduced approaches for the challenges in UWB SAR signal processing are presented. Among the new approaches, IRF-SAR, spatial resolution equations and image quality measurements are arranged to the group of the tools for UWB SAR system design and evaluation. Meanwhile, the RFI suppression, apodization or sidelobe control approaches and SAR imaging algorithm are categorized into the pre-processing, processing and post-processing for UWB SAR data group. The selected applications of UWB SAR in GMTI and ground moving target imaging are also addressed. First of all, several basic concepts of radar and SAR, operation, classifications and UWB SAR are briefly reviewed.

2 Radar and Synthetic Aperture Radar

In this section, the fundamentals of radar and SAR are presented. The section also aims at the principle operations of radar and SAR, and the formulas which are mainly used for calculations in radar and SAR techniques.

2.1 Radar

Radar is an abbreviation of Radio Detection and Ranging. It is a radio system using electromagnetic waves, specifically radio waves, to detect objects and determine the ranges between this radio system and those objects. Although the beginning experiments of Heinrich Hertz showing that radio waves could be reflected from solid objects were carried out in 1886, the milestone for the development of radar did not occur until World War II. Radar has a wide range of applications including those for civil and military purposes. Detecting and ranging air, ground and sea targets are crucial applications of

radar for military purposes. Meanwhile, civilian applications of radar can be found in aviation, marine, monitoring and so forth. A basic radar system includes one transmitter emitting radio waves called radar signals and one or more receiver(s) capturing reflections from objects such as aircrafts, ships, vehicles and terrain. If a radar system utilizes one transmitting antenna and one receiving antenna which are collocated, that radar system is called a monostatic system. A radar system will be called a bistatic system if its transmitting antenna and receiving antenna are separated. For the monostatic case, the radar range R is calculated from the round trip propagation time as

$$R = \frac{c\tau}{2} \quad (1)$$

where c is the propagation speed and equal to the speed of light $c = 3 \times 10^8$ m/s, and τ is the propagation time of the radio waves back and forth. The relationship between the transmitted power P_t and received power P_r of a monostatic radar system is represented by the radar equation

$$\frac{P_r}{P_t} = \frac{GA_e\sigma F^4}{(4\pi)^2 R^4} \quad (2)$$

where G is the gain of the antenna, A_e is the effective area of the antenna, σ is the Radar Cross Section (RCS) of the object, and F indicates the antenna pattern. If a radar system operates in vacuum and without interference, the term F in the numerator of (2) is set to one ($F = 1$). Radar bands and common operating frequencies and wavelengths are summarized in Table 1.

2.2 SAR

SAR is the abbreviation for Synthetic Aperture Radar. It is a form of radar whose aperture is synthesized on account of the movement of the platform. This aperture is much larger than the physical length of the radar antenna. Hence, instead of being located on a ground station as usual, a radar system is mounted on an aircraft or a satellite. A radar system can also be placed on a ground track, which is known as ground-based SAR. Ground-based SAR is seen as a powerful technique for surface deformation monitoring. Let us consider an airborne SAR system as illustrated in Fig. 1.

At an aperture position, the radar broadcasts a radio wave towards an illuminated ground area of interest. This radio wave impinges and interacts with objects in the area of interest. Echoes backscattered from these objects

Table 1: Radar bands and common operating frequencies and wavelengths.

Band	Frequency range	Radar frequency	Radar wavelength
VHF	30–300 MHz	220 MHz	1.36 m
UHF	300–1000 MHz	425 MHz	0.71 m
L	1–2 GHz	1.3 GHz	23 cm
S	2–4 GHz	3.3 GHz	9.1 cm
C	4–8 GHz	5.5 GHz	5.5 cm
X	8–12 GHz	9.5 GHz	3.2 cm
K _u	12–15 GHz	1.3 GHz	2.0 cm
K	18–27 GHz	24 GHz	1.3 cm
K _a	27–40 GHz	35 GHz	0.86 cm

will be collected by the radar. Since the ranges between the radar and the objects on the ground are different, the time delays of these echoes are also different. Chirp signals or also called linear FM signals are particularly used in SAR systems. The mathematical expression of a chirp signal as a function of the range time τ is given by

$$s(\tau) = A \operatorname{rect}\left(\frac{\tau - \tau_0}{T}\right) \exp\left\{i2\pi f_c(\tau - \tau_0) + i\pi\kappa(\tau - \tau_0)^2\right\} \quad (3)$$

where A is the signal amplitude, τ_0 indicates the time delay of the signal, T is the pulse duration, f_c is the center frequency of the radar signal, and κ is the chirp rate computed by the ratio of the signal bandwidth B to the pulse duration T .

Due to the fact that the propagation speed of the radio waves is much faster than the speed of the platform, the radar approximately stops at each aperture position. This procedure is repeated for whole aperture positions associated with the motion of the platform. From a signal processing point of view, a set of echoes recorded at all aperture position is equivalent to echoes collected by a very large antenna at the time.

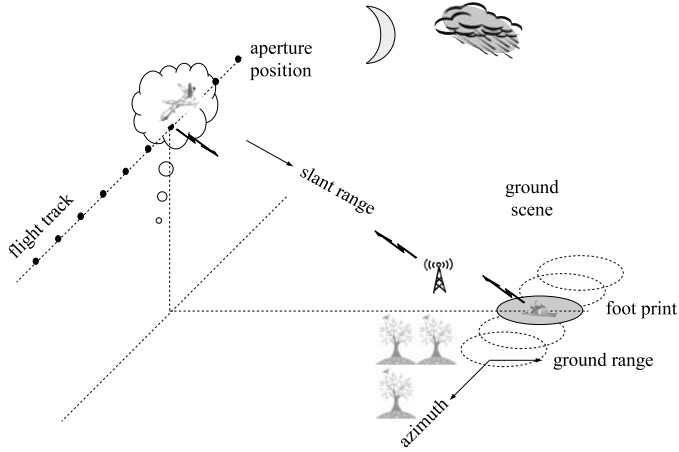


Figure 1: An illustration of the operation of an airborne SAR system.

3 SAR Categorization and UWB SAR

In this section, the bases for SAR categorization are summarized. The categorization can rely on parameters such as fractional bandwidth and antenna beam width associated with the integration angle. A classification of UWB SAR is given in comparison to Narrowband-Narrowbeam (NB) SAR.

3.1 Bases for SAR Categorization

Categorization for SAR can be based on several criteria. As mentioned, a radar system can be attached to an aircraft, a satellite or even a ground track. To distinguish between the SAR systems, different names are assigned to them. If a radar system is carried by an aircraft, that arrangement will be called an airborne SAR system. CARABAS-II [2], LORA [5] developed by the Swedish Defense Research Agency (FOI), P-3 [6] by the Environmental Research Institute of Michigan (ERIM) and SETHI by the French Aerospace Laboratory (ONERA) [7] are examples of airborne SAR systems. A system is called a spaceborne SAR system if the radar is mounted on a satellite. Several well-known spaceborne SAR systems are TerraSAR-X [8] built by the German Aerospace Center (DLR), COSMO-SkyMed [9] by the Italian



Figure 2: The ground-based SAR system built at BTH, Sweden.

Space Agency (ASI) and recently Komsat-5 [10] by the Korea Aerospace Research Institute (KARI), Radarsat by the Canadian Space Agency (CSA), and Envisat by the European Space Agency (ESA). The SAR system built at the Blekinge Institute of Technology (BTH) in Sweden is a ground-based SAR system since this SAR system is placed on a straight ground track [11]. The aperture is synthesized during the movement of the radar along the ground track as shown in Fig. 2.

For a SAR system, the most crucial parameters are the operating frequency and the synthetic aperture length. The terms such as VHF low frequency SAR, UHF SAR, and X-band SAR are usually assigned to SAR systems to state the operating frequencies of those SAR systems. Airborne SAR systems can operate at different frequency bands from VHF-band to X-band whereas L-band, C-band, S-band or X-band are mainly employed by spaceborne SAR systems. The operating frequency of a SAR system strongly influences the SAR spatial resolution. For example, the spatial resolution of X-band SAR systems can be up to 1 m while such resolution is hard to be achieved with a VHF low frequency SAR system. To improve the spatial resolution, SAR systems operating in VHF/UHF bands usually employ large radar signal fractional bandwidths and wide antenna beamwidths which are valid for long synthetic apertures or wide integration angles. For any SAR system, the frac-

tional bandwidth is only in the range $(0, 2]$. For a linear flight track of a platform, the integration angle cannot be beyond the range $[0^\circ, 180^\circ]$.

Static configuration is usually used for SAR categorization. In the simplest case, the transmitter and receiver of a radar system are mounted on the same platform and share a unique antenna for both transmitting and receiving. Such a SAR system is known as a monostatic SAR system. Conversely, the transmitter and receiver can also be separated, for example they are carried by different platforms or the receiver is deployed on a ground station. In this case, the SAR system is called a bistatic SAR. An example of a bistatic system can be found in the SAR system built from two monostatic SAR systems LORA and SETHI. The number of receivers of a SAR system can also be larger than one to create a multistatic SAR system. For applications of interest like GMTI, the transmitter and receiver of a radar system can be carried by the same platform but employ different antennas for transmitting and receiving. In this case, that SAR system can naturally be seen as a bistatic system. Since this arrangement can more or less be seen as a monostatic system, the configuration is usually defined as quasi-monostatic. Azimuth-invariant is another term used in SAR technique concerning static configuration. This indicates a bistatic system whose platforms fly with the same speed and the flight track are parallel.

In addition, the categorization can also be based on the looking direction to distinguish between forward-looking and side-looking SAR or be based on the number of channels generated by SAR systems to divide them into single-channel or multi-channel SAR.

3.2 UWB SAR in comparison to NB SAR

Let us consider again the categorization based on parameters. However, fractional bandwidth and antenna beamwidth are taken into account. SAR systems using small signal fractional bandwidths and narrow antenna beamwidths are considered as NB SAR systems. A typical two-dimensional Fourier transform (2-D FT) of a NB SAR image of a point-like scatterer is sketched in Fig. 3 and its approximation is marked by the light gray color. In this figure, k denotes the wave numbers and ϕ_0 is the integration angle. The subscripts x , y , \max , \min and c correspond to azimuth, range, maximum, minimum and center, respectively. Although spaceborne SAR systems utilize large apertures, most of them are NB SAR systems due to their high operating center frequency, the altitude of the satellites carrying the radars, and the small synthesized apertures in angle.

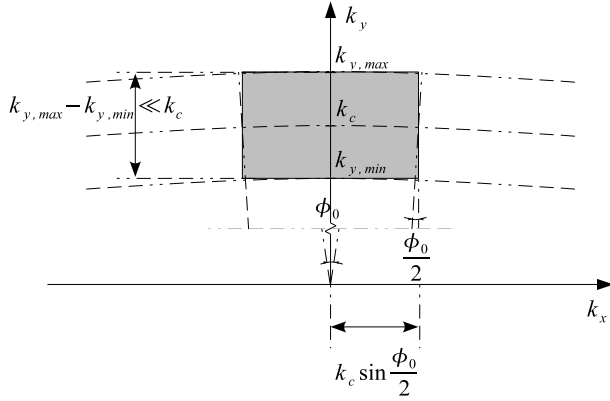


Figure 3: An example of 2-D FT of a NB SAR image of a point-like scatterer and its approximation is marked by the light gray color.

The concept of UWB used in SAR has been used recently in several publications. As seen, this concept does not only relate to the bandwidth of the radar signal, i.e. ultrawideband, but also the beamwidth of the antenna, i.e. ultrawidebeam, utilized by a SAR system. According to the definition of the ultrawideband signal issued by the Federal Communications Commission (FCC) in 2002 [11], signals with the relative bandwidth larger than 0.2 or signals with the absolute bandwidth larger than 500MHz are both considered as UWB signals. However, there has not been any clear definition of ultrawidebeam yet. SAR systems utilizing large signal fractional bandwidths and wide antenna beamwidths which allow synthesizing long apertures are considered as UWB SAR systems. Fig. 4 sketches a 2-D FT of a UWB SAR image of a point-like scatterer which is marked by the dark gray color while the light gray area associates with the NB approximation.

A comparison between the 2-D FT of a UWB SAR image and the NB approximation might be a basis for UWB SAR classification. Their mismatch can be represented by the ratio of the bright gray area to the dark gray area. This ratio is associated with the area resolutions and represented by a function of fractional bandwidth B_r and integration angle ϕ_0 as

$$\chi(B_r, \phi_0) = 1 - \frac{B'_r}{B_r} \cdot \left(1 - \frac{B_r}{2}\right) \cdot \left(\tan \frac{\phi_0}{2}\right) \cdot \left(\frac{2}{\phi_0}\right) \quad (4)$$

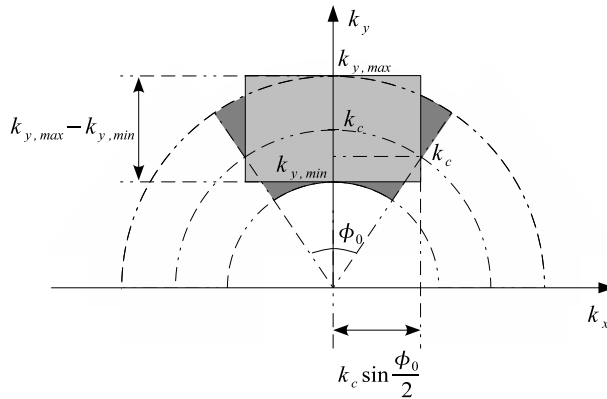


Figure 4: An example of 2-D FT of a UWB SAR image of a point-like scatterer marked by the dark gray color. The light gray area associates with the NB approximation.

where

$$B_r' (B_r, \phi_0) = \sqrt{\left(1 + \frac{B_r}{2}\right)^2 - \left(1 - \frac{B_r}{2}\right)^2 \tan^2 \frac{\phi_0}{2}} - \left(1 - \frac{B_r}{2}\right) \quad (5)$$

Fig. 5 plots $\chi(B_r, \phi_0)$ as functions of fractional bandwidth B_r and integration angle ϕ_0 . A bound of $\chi(B_r, \phi_0) \leq 0.1$, i.e. the mismatch is smaller than 10%, is proposed to be the limit between NB SAR and UWB SAR. At small integration angles, the limit of the fractional bandwidth is $B_r \approx 0.2$. This complies with the UWB concept defined by FCC in 2002. According to the categorization previously given, the SAR systems such as CARABAS-II, LORA, P-3 and PAMIR [13] fall into the UWB SAR group.

The research works presented in this dissertation deals with single- and multi-channel monostatic airborne side-looking UWB SAR systems. However, the results can be applied directly to spaceborne, quasi-monostatic, and NB cases. Extensions to bistatic or multistatic and forward-looking cases are possible but require further modifications.

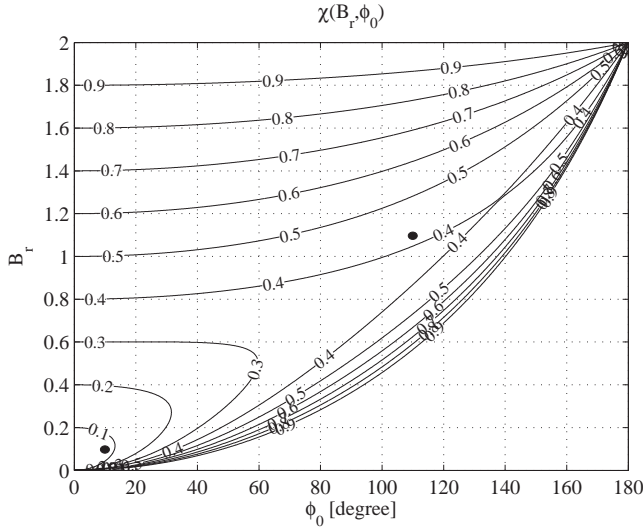


Figure 5: Plots of $\chi(B_r, \phi_0)$ as a function of the fractional bandwidth and the integration angle. The black solid circles mark the fractional bandwidths and integration angles of examples of a NB SAR and a UWB SAR system.

4 SAR Systems

The research works in this dissertation use data collected in different field campaigns performed by CARABAS-II and LORA. The information and the parameters of these SAR systems are given in this section.

4.1 CARABAS-II

CARABAS-II is an airborne imaging sensor developed by FOI [2]. Fig. 6 shows the Sabreliner platform which is used by CARABAS-II. The system operates in the frequency range 20-90 MHz (VHF) with horizontal polarization and utilizes wide beamwidth dipole antennas of more than 90° . The antennas are arranged in the tubes attached to the front lower part of the platform. Different field campaigns have been performed by the system since 1996. The system parameters which have been used in the data collection campaign in Visingö, Sweden are summarized in Table 2. The system fractional bandwidth,



Figure 6: CARABAS-II developed by FOI.

i.e. the ratio of the absolute bandwidth to the center frequency, estimated from the parameters is about $B_r \approx 1.15$ and the associated integration angle with respect to the aim point is up to $\phi_0 \approx 110^\circ$.

CARABAS-II is designed for some particular applications such as change detection [14], stationary ground target detection in open areas or areas obscured by trees. The system offers opportunities to investigate backscattering mechanisms from forests when using low frequency radar signals for their imaging. Some information about forest stem volume [15] and even of individual tree [16] which is of interest to forest monitoring and management, can be retrieved using CARABAS-II. Interferometric processing of VHF SAR data collected from two or several parallel and well separated flight tracks in forested areas is used to generate elevation maps [17]. Recently, CARABAS-II has been used as a reference system for many research works in the field of UWB SAR data processing. Some of them are included in this dissertation. GMTI application is also experimented with CARABAS-II using the moving target detection by focusing technique [1]. In [18], another crucial application, the motion parameter estimation for targets, is developed on CARABAS-II.

Due to the array configuration of CARABAS-II, the application of space-time processing technique to its data is quite constrained. This issue will be brought up again later in this dissertation.

Table 2: The CARABAS-II parameters for the field campaign in Visingö.

Parameter	Value
The highest frequency processed f_{max}	82 MHz
The lowest frequency processed f_{min}	22 MHz
Platform speed v_{pl}	128 m/s
Aperture step ΔL	0.9375 m
Aperture length L	33600 m
Flight altitude	4940 m
Minimum range to the aim point r_0	11250 m
Pulse Repetition Frequency (PRF)	137 Hz

4.2 LORA

Besides CARABAS-II, FOI also develops another airborne imaging sensor named LORA [5]. This system also employs the same Sabreliner platform shown in Fig. 6. LORA is originally designed to operate in the UHF-band 200-800 MHz with horizontal polarization. The system utilizes two different element types developed for the low and high part of the operating frequency range. Five identical LORA elements can be arranged in each tube. This arrangement supports the GMTI application in which moving objects can be located accurately [19]. The low frequencies used in LORA can be employed to detect moving objects even when hidden by trees in the forested areas. The application of LORA can also be found in suppression of jamming signals.

The first measurement campaign was carried out in late 2002. In 2006 and 2007, bistatic SAR imaging in the low VHF-band was experimented with CARABAS-II (transmitter) and LORA (receiver), however, located on ground. A bistatic SAR system operating in VHF/UHF-band was built using LORA and SETHI at the end of 2009.

In the GMTI campaign in 2004, this system is configured to work as a multistatic SAR system with three antennas (one transmits and two receive simultaneously). The displacement of the phase center of the forward and backward antenna is approximately five aperture steps. Since both the transmitter and the receivers are mounted on the same platform, this system can

Table 3: The LORA Parameters for the GMTI application.

Parameter	Value
The highest frequency processed f_{max}	307 MHz
The lowest frequency processed f_{min}	333 MHz
Platform speed v_{pl}	130 m/s
Aperture step ΔL	0.1 m
Aperture length L	600 m
Flight altitude	3000 m
Minimum range to the aim point r_0	7000 m
PRF	1300 Hz

approximately be seen as a monostatic system and therefore called a quasi-monostatic system. Table 2 provides the LORA parameters configured for the GMTI application. The system fractional bandwidth is calculated from the maximum and minimum frequencies as $B_r \approx 0.08$ and the associated integration angle with respect to the aim point is up to $\phi_0 \approx 5^\circ$. With these values, LORA for GMTI can be seen as a NB SAR system.

5 Tools for UWB SAR system design and evaluation

A point-like scatterer, e.g. a corner reflector deployed in a SAR scene for system calibration in a data collection campaign, appears differently in a reconstructed SAR scene. This difference depends strongly on the SAR system which illuminates the SAR scene. Two critical parameters which affect the shape of a point-like scatterer in a SAR image are the fractional signal bandwidth and the antenna beamwidth associated with the integration angle. A function which represents the SAR image of a point-like scatterer is called IRF-SAR. Based on IRF-SAR, spatial resolution equations in azimuth and range can be derived easily. IRF-NSAR is also used as a basis in building image quality assessments for SAR systems. From a SAR system designer's point

of view, IRF-SAR, resolution equations and SAR image quality assessments are seen as tools for SAR system design and evaluation.

5.1 Impulse response function in UWB SAR imaging

IRF-SAR allows us to determine the shape of a point-like scatterer in a reconstructed SAR scene illuminated by a SAR system. For NB SAR, IRF-SAR is represented by a 2-D *sinc* function. In the context of this dissertation, this function is named by the Impulse Response Function in NB SAR Imaging (IRF-NSAR). IRF-NSAR is nothing else than the 2-D Inverse Fourier transform (IFT) of a 2-D *rect* function which is an approximation for the 2-D FT of the SAR image of a point-like scatterer.

For UWB SAR, the presentation of a point-like scatterer in a reconstructed SAR scene by IRF-NSAR is not further valid. The reason is the invalidity of the 2-D *rect* approximation in UWB SAR. The true representation for the 2-D FT of the SAR image of a point-like scatterer is a set of concentric circular arcs which subtend an angle of ϕ_0 and their radii are in the interval $[k_{y,min}, k_{y,max}]$. In [20], an Impulse Response Function in UWB SAR Imaging (IRF-USAR) in polar coordinates is introduced. IRF-USAR implies IRF-NSAR, i.e. IRF-USAR and IRF-NSAR are identical with small values of the fractional signal bandwidth and the integration angle. IRF-USAR is also extended for the particular SAR configurations, e.g. circular apertures. IRF-USAR opens opportunities to derive UWB SAR resolution equations and to define UWB SAR image quality assessments.

5.2 UWB SAR resolution equations

Spatial resolutions (azimuth and range) are considered to be one of the most important parameters among SAR image quality assessments. They describe the distance between two objects on the ground at which the objects appear distinct and separate in a SAR image. Spatial resolution equations are always necessary to estimate the azimuth and range resolutions which can be achieved with a SAR system. The azimuth and range resolutions given by spatial resolution equations can be a basis to evaluate the performance of that SAR system. The azimuth and range resolutions are usually based on the -3 dB width or Half Power Beamwidth (HPBW) of the mainlobe. The spatial resolution equations for NB SAR can be derived easily by assigning *sinc* functions in IRF-NSAR to -3 dB and then solving them. The azimuth resolution equation given in [21] and the range resolution equation in [22] can

be derived from this principle as shown in [23]. Although these resolution equations are widely used, they may result in large errors in estimations for UWB SAR cases.

For UWB SAR systems with large fractional signal bandwidth and wide integration angle, the coupling between azimuth and range frequencies must be taken into account. Considering this coupling, the so-called area resolution equation for UWB SAR is suggested in [24]. However, this area resolution equation only provides the lower bound of area resolution but not the separate azimuth and range resolutions. In theory, the azimuth and range resolution equations can be achieved by setting IRF-USAR to -3 dB and solving it. In practice, it is not easy to solve IRF-USAR analytically. A possible approach for such a problem is to find the roots of IRF-USAR in a numerical way.

The research work presented in [22] shows that IRF-NSAR and -USAR are very similar in the intensity interval from -6 dB to 0 dB. For this reason, the mainlobe of IRF-USAR down to -6 may still be approximated as a *sinc* curve. The work also finds that the frequency coupling can be represented by HPBW narrowing/broadening factors. Based on these findings, the UWB SAR resolution equations are proposed in [22].

5.3 UWB SAR quality measurements

Evaluating the performance and/or efficiency of an arbitrary system is usually based on the measurements for the end-product produced by that system. For a SAR system, a SAR scene reconstructed from the data collected by that SAR system can be considered to be the end-product. The evaluation can therefore rely on SAR image quality measurements. The measurements are usually performed on known point-like scatterers. In general, corner reflectors used for system calibration in field campaigns can be seen as point-like scatterers. Basic SAR image quality measurements are spatial resolution (azimuth and range), Integrated Sidelobe Ratio (ISLR), and Peak Sidelobe Ratio (PSLR). Again, the spatial resolution is the most significant parameter among SAR image quality assessments. The spreading energy of mainlobe over sidelobes is indicated by ISLR. PSLR measures the ability to image a weak reflective target affected by a strong reflective target nearby. Before any measurement, delimitations of mainlobe and sidelobe are required. Two parameters of the delimitations are geometric form and dimension.

For NB SAR, the delimitations are quite simple and can rely on IRF-NSAR. The locus of the first nulls of the 2-D *sinc* function can be shown to be rectangular. Naturally, rectangles are used to delimit mainlobe and

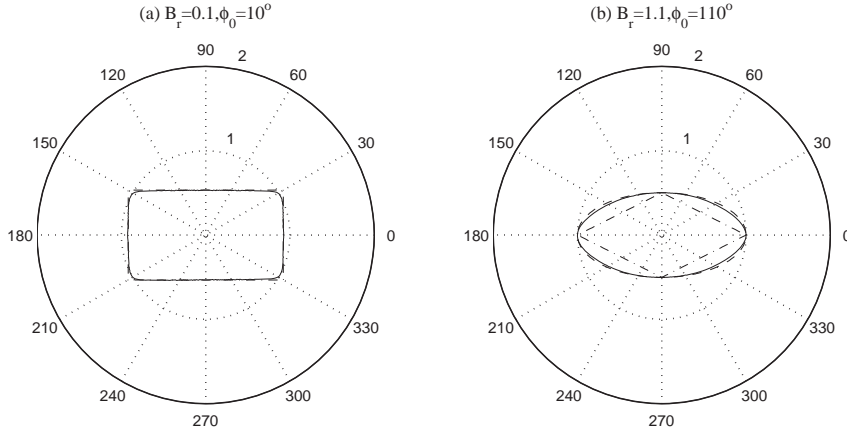


Figure 7: The locus of the first nulls of IRF-USAR with different values of B_r and ϕ_0 and three possible approximations, rectangle, ellipse, and lozenge. (a) $B_r = 0.1, \phi_0 = 10^\circ$, (b) $B_r = 1.1, \phi_0 = 110^\circ$.

sidelobe. The dimensions of mainlobe and sidelobe areas are both determined by a number of times of the HBPW, i.e. resolution. For an arbitrary *sinc* function, the ratio of First Null Beamwidth (FNBW) to HBPW is a constant and approximated to 2. The *sinc* function also attenuates to below -20 dB from 10 times of the HBPW. For these reasons, the factors of 2 and 10 are usually used to limit the areas of mainlobe and sidelobe, respectively, for NB SAR cases. The currently used definitions on SAR image quality measurement [25]-[27] are matched to these analyses.

Some findings in UWB SAR image quality measurements are presented in [28]. Based on a series of investigations, some suggestions for the mainlobe and sidelobe delimitations aiming at CARABAS-II have been given. For example, elliptical areas are recommended for the geometric form delimiting mainlobe and sidelobe areas. The dimension of mainlobe is limited by a factor of 3 for UWB SAR cases instead of 2 for NB SAR cases. The research also suggests that the image quality measurements should be performed at different integration angles since different azimuth focusing obtained at different integration angles results in different spatial resolution in azimuth and therefore different ISLR and PSLR. In addition, a new measurement, so-called

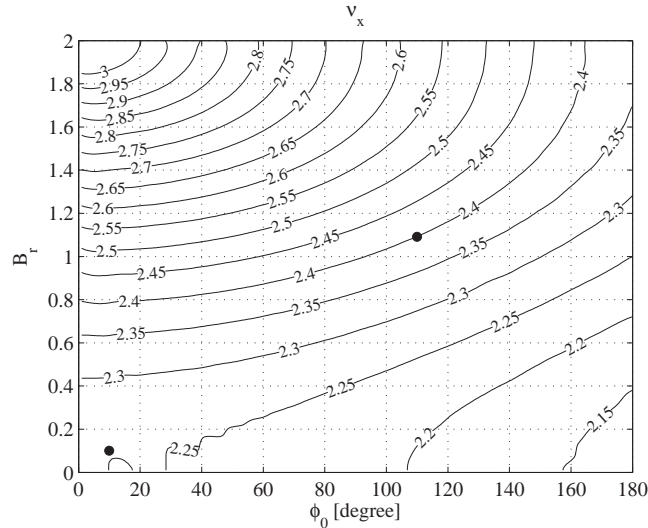


Figure 8: Numerical results of the ratio of FNBW to HPBW in azimuth ν_x . The black solid circles mark the fractional bandwidths and integrations angles of examples of a NB SAR and a UWB SAR system.

differential resolution, is introduced. Such measurement makes the comparisons in term of image quality much more convenient. However, the suggested procedure to delimit mainlobe and sidelobe areas requires much of effort. At the time the research was published, IRF-USAR had not yet been derived. The lack of IRF-USAR prevents having more investigations and clearly limits the generality of these findings.

Hence, IRF-USAR derived in [20] can be a basis for the mainlobe and sidelobe delimitations which are essential in UWB SAR image quality measurements. In [29], IRF-USAR has been used in the investigations of geometric form and dimension. The elliptical area is proved to be more suitable than the rectangular area for geometric form while the factor of 2.5 is shown to be enough for presenting the spread of mainlobe areas. However, those investigations are limited only for one specific UWB SAR system.

Fig. 7 plots the loci of the first nulls IRF-USAR with different values of fractional bandwidth $B_r \in [0.1, 1.1]$ and integration angle $\phi_0 \in [10^\circ, 110^\circ]$. Three possible approximations, i.e. rectangle, ellipse and lozenge, for these

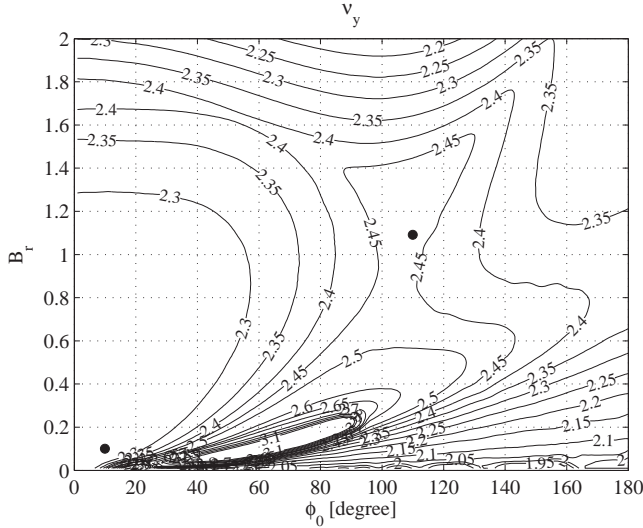


Figure 9: Numerical results of the ratio of FNBW to HPBW in range ν_y . The black solid circles mark the fractional bandwidths and integrations angles of examples of a NB SAR and a UWB SAR system.

loci are also plotted for visual evaluations. The locus of the first nulls with $B_r = 0.1, \phi_0 = 10^\circ$, i.e. NB SAR, is approximately given by a rectangle while that with $B_r = 1.1, \phi_0 = 110^\circ$, i.e. UWB SAR, is perfectly matched with an ellipse. We can also predict that mainlobe areas in UWB SAR imaging may vary to lozenge areas when B_r and ϕ_0 increase. Sidelobe areas can be naturally delimited by the same geometric forms.

Investigations into the dimensions of mainlobe areas in azimuth and range are given in Fig. 8 and 9, respectively. The figures show the numerical results of the broadening factors of the mainlobe, i.e. the ratios of FNBW to HPBW, in azimuth ν_x and in range ν_y . In this investigation, the interval of fractional bandwidth is also $(0, 2]$ and the associated integration angle $[0^\circ, 180^\circ]$. As can be seen from these figures, the factors ν_x and ν_y depend strongly on the signal fractional bandwidth and the integration angle and are in the interval between 2 and 3. For UWB SAR system utilizing, for example $B_r = 1.1$ and $\phi_0 = 110^\circ$, the broadening factor of the mainlobe is closer to 2.5 than 2. Even at small fractional bandwidths and narrow integration angles, the factors of

2 to determine the dimensions of mainlobe areas are not very accurate. For UWB SAR, the factors of 2 are not sufficient to present the spread of mainlobe areas. Using factors of 2.5 in this case is reasonable.

6 UWB SAR Data Pre-processing, Processing and Post-processing

Pre-processing for UWB SAR refers to procedures to process radar echo received by a SAR system before any further processing. Processing refers to SAR algorithms to reconstruct scenes illuminated by SAR systems. Procedures to process end-products produced by a SAR system like a reconstructed SAR scene illuminated by that SAR system are seen as post-processing.

Low energy radar signals are usually affected by other RFI resources such as radio and television broadcasting stations, base transceiver stations used in mobile communications and so on. For a SAR system, the possibility to get effects from RFI resources depends on the radar signal bandwidth, the operating frequency range, and the antenna beamwidth utilized by that system. This possibility for UWB SAR systems operating in wide frequency range and utilizing wide beamwidth antenna is quite high. In addition, since RFI energy is generally much higher than radar signal energy, the effects of RFI are significant. The radar echo may be worthless without RFI cancellation or suppression. Pre-processing radar echo before any further processing like RFI cancellation is essential.

UWB SAR data processing requires SAR algorithms. Due to the characteristics of UWB SAR, not all algorithms are valid for processing. The algorithms for UWB SAR should meet the following demands: not require extremely powerful computers with huge memory, support real time processing, handle large range migration, and manage motion error compensation. An algorithm containing NB approximations works neither with UWB SAR data nor does it result in large reconstructed and well focused scenes simultaneously. The choice of algorithms for UWB SAR is therefore very critical.

A reconstructed SAR scene illuminated by a SAR system is considered as an end-product produced by that SAR system. This end-product is evaluated by image quality assessments such as spatial resolutions, ISLR, and PLSR. In UWB SAR imaging, the energy of mainlobe areas is spilled not only over orthogonal sidelobes but also over non-orthogonal sidelobes. Due to the existence of both orthogonal and non-orthogonal sidelobes, ISLR and

PSLR measurement results for UWB SAR cases are usually worse than the ones for NB SAR cases. As such, the ability to image a weak reflective target is quite limited. A post-processing step like apodization should be included in UWB SAR data processing.

6.1 RFI Suppression in UWB SAR

RFI suppression is listed as one of the challenges in UWB SAR processing. This pre-processing step is supposed to be performed before any further processing. However, there have been few publications on this topic. This can be explained by the strong dependence of RFI on the operating frequency of the SAR system as well as the illuminated ground scene. SAR systems working at low frequencies and/or utilizing large bandwidths are much more sensitive to RFI than SAR systems working at high frequencies and utilizing small bandwidths.

Let us consider the airborne UWB low frequency CARABAS-II system [2]. As mentioned in the previous chapters, this system operates in the lower VHF-band and employs wide beamwidth dipole antennas. The field campaigns with CARABAS-II have been performed mainly in Sweden. The radar signal can therefore be affected by various shortwave bands (5.9-26.1 MHz), citizens' bands (26.965 - 27.405 MHz), television channels 2-6 (54-88 MHz) and FM broadcast bands (88-108 MHz). The measured power spectrum on the CARABAS-II recording data indicates that the influence is seen to be significant since the RFI energy is much higher than the radar backscattered energy (≈ 40 dB) [30]. To possibly use the CARABAS-II radar signal, approaches to eliminate or at least suppress RFI are required. From the point of view of signal processing, approaches for RFI suppression can be classified into two classes: non-adaptive and adaptive.

An example of the non-adaptive approach is Linear RFI Filtering (LRF) which is mentioned in [31] and currently used in CARABAS-II data processing. The approach is based on a linear filter which is defined by the inversion of the averaged range frequency response or the so-called smooth function. Thus, the procedure of the approach is as follows. The radar signal is first transformed to frequency-domain, then filtered with the averaged range frequency response, and finally transformed back to time-domain. LRF has been proven to be robust in stationary environments. However, since LRF is non-supportive for real-time processing and unable to handle short-time RFI, it may be inefficient to apply LRF in non-stationary environments, where RFI sources can appear anywhere and anytime in an illuminated SAR scene.

Adaptive RFI suppression approaches in UWB SAR are usually based on an Adaptive Line Enhancer (ALE) [32]. The filter coefficients in ALE is updated continuously using the adaptive algorithms such as Least Mean Square (LMS), Normalized Least Mean Square (NLMS), Leak Least Mean Square (LLMS) and Recursive Least Square (RLS). The idea to use ALE to eliminate narrowband RFI in wideband radar echo has been proposed for the first time in [33]. The roles of signal and noise in the original mechanism are exchanged. In this research work, ALE controlled by LMS is proposed to suppress RFI in Wideband SAR (WB). The approach is experimented on the baseband SAR signals (40 MHz) and resulted in a good RFI suppression. A similar proposal but in frequency-domain with amplitude normalization is introduced in [34]. Thus, ALE works with the DFT of radar echo instead of the radar echo. The main limitation of these approaches can mainly be found in LMS, which may be sensitive to non-stationary SAR scenes. To avoid this sensitivity, another approach is suggested in [30],[35]. The approach aims at UWB low frequency SAR systems. The basis of the approach is also ALE. The NLMS algorithm, which can work well in the non-stationary environments, is recommended in this approach. In [35], the interaction between the integration angle and the effects of RFI on a reconstructed SAR scene is also explored. The possibility to integrate this RFI suppression approach into SAR imaging algorithms is investigated in [30]. This integration helps to reduce the computational cost required by the approach. In [36], an experiment on the SAR data affected by mobile phone signals is presented. In this research work, RLS is used to control ALE as the capability of fast tracking time-varying signals and noise statistics in RLS is supposed to be better than other adaptive algorithms such as LMS and NLMS.

6.2 UWB SAR Imaging Algorithms

The first SAR imaging algorithm based on computer processing, known as Range Doppler (RD) [37], was introduced in the 1970's. Later on, other SAR imaging algorithms aiming at high image quality and/or minimizing processing time have been introduced. In general, the SAR algorithms can be divided into two main groups: time-domain and frequency-domain algorithms. Time or frequency-domain here refers to the domain where the SAR data is mainly processed.

According to the division, RD belongs to the frequency-domain algorithm group. The radar echoes are first transformed to the Range-Doppler domain by one-dimensional (1-D) Fast Fourier Transform (FFT) in azimuth. Range

cell migration correction and azimuth compression are then handled before transforming back by 1-D Inverse Fast Fourier Transform (IFFT) to obtain the SAR image of the illuminated SAR scene. Range Migration (RM) [38] and Chirp Scaling (CS) [39] are two other typical frequency-domain imaging algorithms. The former offers high SAR image quality but it requires computationally expensive interpolation, i.e. Stolt interpolation [40]. The latter does not require any interpolation and is efficiently performed by complex multiplications and FFT. The processing time required by CS is therefore reduced significantly in comparison to other frequency-domain imaging algorithms. The main disadvantage of CS is the approximations caused by eliminating high order terms in the Taylor expansion of the phase of the radar signal which prevents the algorithm from working with high PRF data. The approximation also causes large phase errors which do not allow CS to handle large range migrations. However, due to the superiority in processing time, CS has become a topic of interest in the field of SAR imaging algorithm for many years. This can be proved by a significant number of CS versions such as Nonlinear Chirp Scaling (NCS) [41], Extended Chirp Scaling (ECS) [42] and recently Ultrawideband Chirp Scaling (UCS) [43] aiming at different goals.

Time-domain algorithms refer to the backprojection algorithms whose backprojection is interpreted as a superposition of backprojected radar echoes to reconstruct a SAR scene. The first time-domain algorithm is Global Backprojection (GBP) [44] which was developed in the 1980's. GBP is shown to be a linear and direct transformation process from radar echo into SAR image. The calculation of the ranges between each aperture position and each SAR image pixel in GBP leads to an extremely high computational cost. However, this is exchanged by high quality SAR images, i.e. without phase error. The range calculation based on each aperture position in GBP also means that the motion errors are compensated automatically and the real time processing is possible. The scene size illuminated by a SAR system can be seen to be unlimited and depends strongly on the antenna beamwidth, integration time, flight attitude, radiated power, and PRF of the SAR system. The scene imaged by GBP can be selected from small areas to the whole illuminated scene. Fast Backprojection (FBP) [45], [46] and Fast Factorized Backprojection [47] are developed on GBP so that they retain the characteristic of GBP. Although both FBP and FFBP manage to overcome the main drawback in processing time of GBP, there is always a trade-off between the phase errors and processing time. The principle of FBP is to process the SAR data on a subaperture and/or subimage basis. Instead of backprojecting radar echoes directly to a SAR image, FBP handles SAR data in two stages: beam-forming and local

backprojection. If the size of the reconstructed SAR scene size is $N \times N$ and the number of the aperture position is also N , the number of operations required by FBP can be reduced to a factor of \sqrt{N} in comparison to GBP. The difference between FBP and FFBP is only the number of beam-forming stages. FFBP requires more than one beam-forming stage prior to the local backprojection stage. Such factorized processing allows reducing the number of operations by a factor of $\log(N)$. Due to the time-domain characteristics, i.e. unlimited scene size, manageable motion compensation, local and real time processing, the time-domain SAR algorithms GBP, FBP and FFBP are very suitable and highly recommended for UWB SAR data processing [48]. In [49] and [50], the GBP and FBP algorithms are examined with the UWB SAR data and the results show the good performance of these algorithms. The capabilities of different FFBP versions working with UWB SAR data are tested and compared in [51]. The different phase errors generated by two FFBP versions, which cause defocusing in the image, are also discussed in this publication. The frequency-domain algorithms are also candidates for UWB SAR data processing. A comparative study of time- and frequency-domain algorithms given in [48] has shown that if there was no motion error, RM would be an excellent candidate for UWB SAR data processing. However, in reality, the motion errors caused by platforms need to be compensated to focus SAR data. An investigation into the motion compensation for the nonlinear sensor trajectories presented in [52] shows difficulties to focus SAR data by using the frequency-domain SAR algorithms. Ignoring the large phase error caused by the elimination of the high order phase terms, UCS [43] offers opportunities to process different kinds of UWB SAR data which is not valid for other CS versions.

6.3 Apodization

Apodization is an important post-processing step since it connects directly to the quality of the final product of a SAR system. Conventional apodization methods are classified into two groups: linear and nonlinear. Linear apodization refers to the apodization methods using 2-D weighting functions to filter the 2-D DFT of a SAR image in wave-domain in order to suppress sidelobes. Such methods allow orthogonal sidelobe suppression, preserving phase information of SAR images, however, this is always accompanied by loss in SAR spatial resolutions. The relationship between the sidelobe suppression and the loss in resolutions is decided by the 2-D weighting function in use. The mostly used weighting functions are *Rect*, *Hanning*, *Hamming* and *Blackman*.

Nonlinear apodization can be interpreted as linear apodizations in combination with a set of nonlinear operators. Nonlinear apodization methods have shown capability to control sidelobe levels and retain the resolutions, simultaneously. However, the nonlinear apodization methods can damage the phase information of SAR images and the additional information being contained in the complex values of image pixels. In the nonlinear apodization process, a number of linear apodized images are utilized as the input of the nonlinear operators. The nonlinear operators work in the image-domain and on a pixel-by-pixel basis. The outputs of these nonlinear operators are nonlinear apodized images. The performance of nonlinear apodization methods depends on the number of linear apodized images taken into account by the nonlinear operators and the type of data (complex or complex modulus) that these nonlinear operators work with. Well-known nonlinear apodization methods are Dual Apodization (DA), Multiple Apodization (MA) - a logical extended version of DA, Complex Dual Apodization (CDA) and Spatially Variant Apodization (SVA) [53].

However, both linear and nonlinear apodization methods are introduced for images reconstructed from NB SAR data in which orthogonal sidelobes, i.e. the sidelobes in azimuth or range, are dominant. In images reconstructed from UWB SAR data, both orthogonal and non-orthogonal sidelobes exist, i.e. the sidelobes not in azimuth or range, which need to be eliminated in order to avoid the degradation of image quality. Applying the linear apodization methods to UWB SAR is sparsely mentioned in [54] as this research work does not give any suggestion to define the 2-D weighting functions just as it does not account for the effects to SAR images caused by the linear apodization. In [55], the same topic is discussed again in detail. For UWB SAR, the loss in resolution caused by linear apodization is much higher than NB SAR. The loss in azimuth resolution is more sensitive than in range resolution as the independence of the loss in azimuth resolution on the integration angle. The loss in range resolution can be avoided, even for a large fractional bandwidth and a wide integration angle, by a reasonable selection of fractional bandwidth and integration angle for SAR systems [55]. Also in [55], a 2-D *Cosine-on-pedestal* weighting function is recommended for linear apodization to optimize between the efficiency in sidelobe suppression and the loss in spatial resolution. The optimization is analyzed in detail in [56].

Nonlinear apodization is proved to be applicable to UWB SAR [55]. Hence, the results given in [55] indicate that MA can suppress both orthogonal and non-orthogonal sidelobes in images reconstructed from UWB SAR data and retain spatial resolutions. However, the phase information is most likely to

disappear in the final images as MA works only with complex moduli of image pixels. To preserve the phase information, MA is suggested to work with the in-phase and quadrature parts of image pixels separately. However, there is no way to help MA to retain the additional information being contained in the complex values of image pixels. CDA is introduced as a solution for this challenge using the so-called intermediate weighting function. However, the performance of CDA is usually poor. This can be explained by the criticalness in the selection of weighting functions as there is not a single weighting function which is optimum for all images. The criticalness can only be lightened by using different weighting functions in the linear apodization, i.e. MA, without phase reservation. Another solution for keeping the resolution unchanged, preserving the phase information as well as additional information in apodization can be to use a dynamic weighting function. In the SVA method, the dynamic window is nothing else but a 2-D *Cosine-on-pedestal* function with dynamic weighting factors. However, to use this solution for UWB SAR cases, further investigations are required.

7 Applications of UWB SAR

The application of SAR in imaging can be seen as a basis for other applications in geoscience and remote sensing. UWB SAR systems can offer large scene size and high resolution imaging and therefore allows us to detect changes, distinguish SAR scene features, recognize and identify targets of interest in large scale areas. Systems operating at low radar frequencies even facilitate detecting changes in dense forested areas or under camouflage. In this dissertation, the concentration is on the UWB SAR application in GMTI.

A common GMTI solution is based on antenna array solutions without SAR capabilities. However, there are also other GMTI solutions for single-channel SAR based on, e.g. Doppler shift [57], shadowing phenomenon [58] and magnitude of phase errors [59]. For multi-channel SAR, GMTI solutions can be constructed on space-time processing techniques [60] such as Displaced Phase Center Antenna (DPCA) [22] and Space-Time Adaptive Processing (STAP) [61]. Moving target detection by focusing [62], developed recently, is another GMTI solution aimed at UWB SAR systems. This solution has been tested with CARABAS-II to detect the Ebba Brahe ferry in the lake Vättern, Sweden [1]. This solution is also available for the civil traffic monitoring tasks [63].

7.1 Moving targets detection by focusing in UWB SAR

Moving targets in an illuminated ground scene are displaced and defocused to elliptic or hyperbolic curves in a reconstructed SAR image [64]. For NB SAR, the displacement is mainly caused by movements in the range direction while movements in the azimuth direction result in the defocusing. For UWB SAR associated with long integration time, movements in range direction produce both displacement and defocusing in a reconstructed SAR image. Due to the dispersion of the energy reflected from moving targets, these targets can be hidden by clutter and noise and may therefore not appear in a reconstructed SAR image, especially when the targets are fully obscured by surrounding clutter.

The moving target detection by focusing technique is built on the fact that a moving target can be considered to be stationary in a SAR image formation process if the SAR platform is assumed to move with the difference velocity of the original platform velocity and the target velocity. Hence, the moving target can be focused in the reconstructed SAR scene simply by scaling the speed of the platform with the Normalized Relative Speed (NRS) [65]. This procedure smears clutter surrounding the moving target at the same time.

For detection, different blind hypotheses, so-called NRS under test, must be tested until the optimum moving target focusing for detection is reached. The energy reflected from moving targets and clutter at each hypothesis is therefore either more concentrated or more dispersed. If a moving target exists and it is focused with true NRS, the energy reflected from that target will be highly concentrated whereas the energy reflected from clutter will be strongly dispersed. The optimum step size between NRS under test for detection is suggested in [66].

In [62], the GBP algorithm is selected to be the basis of the focusing approach by NRS. Hence, the SAR data is processed by GBP with different NRS under test. The processed data is then examined to detect moving targets based on intensity. The procedure to perform the moving target detection by focusing technique is given in [1] as follows:

- Processing data with different hypotheses on NRS (NRS under test) in SAR image formation.
- Examining image pixels after the data processing.
- Detecting the presence of moving targets based on intensity.

As soon as the moving target is detected, an appropriate method can be used to estimate such parameters as speed, moving direction, and dimension of the target object. The investigation in [26] demonstrates that the technique not only facilitates detecting moving targets but also estimates motion parameters such as NRS. An estimation of NRS can be achieved by testing other different hypotheses with smaller steps surrounding to the NRS retrieved in the detection.

7.2 Fast detection of moving targets by focusing in UWB SAR

The main shortcoming of the moving target detection technique is the processing time required by this detection technique. The large number of tested blind hypotheses contributes significantly to the processing time of this technique. Although reducing the range of tested blind hypotheses and increasing the step size between hypotheses shorten the processing time of the technique, this also results in the poor performance of the technique due to detection failures and high false alarm rate. The other contribution to the processing time comes from the GBP algorithm which is used as the basis of the focusing approach. This algorithm requires a high computational cost. An approach for such a problem is to employ faster algorithms for the focusing approach.

In [67], the suitability of the RM algorithm [38] for the focusing approach in the detection technique is examined. A comparison between the performance of the original detection technique and the one using RM for its focusing approach indicates that without motion error, the detection results are the same. This algorithm is also investigated to refocus moving targets in reconstructed SAR images [68]-[70]. The introduction of the UCS algorithm [43] gives another opportunity to further shorten the processing time of the detection technique. The possibility of using UCS in the detection technique is investigated in [1]. However, due to the lack of time-domain characteristics, frequency-domain algorithms in general and UCS in particular can be used in certain cases, e.g. short integration time.

Using the polar grid version of the FBP algorithm [46] and the FFBP algorithm [47] for the focusing approach is shown to reduce the processing time of the detection technique significantly [1],[71]. Basically, the replacements of GBP by FBP and FFBP can shorten the processing time to factors of \sqrt{N} and $\log(N)$, respectively. However, the processing time can be further reduced depending on the ways to use these algorithms for the focusing approach in the detection technique. The analytical number of operations required by

the detection technique and the optimum selection of subaperture are also presented in [71]. Similarly, an investigation of the possibility to use the local processing version of the FBP algorithm [45] for the detection technique is given in [72]. Also in this study, it is the first time a combination of the detection technique with the space-time processing is mentioned.

7.3 A combination of the detection technique with the space-time processing

Besides the limitation in processing time, the moving target detection by focusing technique also shows the restriction in detection ability in certain cases [72], e.g. the true NRS of a moving target is approximate or equal to one. This example corresponds to either a very slow moving target or target moving under the so-called invisible direction [72]. To overcome this obstacle, a combination of the detection technique with the space-time processing is recommended. In [72], DPCA is selected to demonstrate this combination. According to this proposal, dual-channel SAR data is first handled by DPCA to suppress ground clutter. The data with clutter suppression is then processed again by the moving target detection by focusing technique. However, the requirements of DPCA to work properly such as identical channels and PRF perfect matching to the platform velocity are very strict and may not be satisfied in practice. A combination of the detection technique with STAP is one solution for this problem. However, the computational cost required by STAP prevents the efficiency of this combination

The integration of space-time processing into the time-domain algorithms is presented in [73]. The integration is expected to lighten the strict requirements of DPCA and improve the computational practicality of STAP. Hence, DPCA and STAP are proposed to perform after the beam-forming stage. According to this proposal, the range compressed SAR data collected by each antenna is first processed separately in the beginning of the beam-forming stage. The beams formed by all channels are then handled by DPCA or STAP to generate a single beam with clutter suppression. Moving target detection is performed on the beam with clutter suppression. This beam is then tested with different hypotheses of NRS in the backprojection stage. Moving target detection is also performed on the reconstructed image. Hence, this integration can provide a reliable detection. Since the array configuration of CARABAS-II does not support DPCA, LORA configured for the GMTI application is used as the reference system for this study.

8 Dissertation Overview

8.1 Part I–A - An impulse response function for evaluation of ultrawideband SAR imaging

The analyses in this study show that the commonly used IRF-SAR - 2-D *sinc* function or so-called IRF-NSAR - is inappropriate for UWB SAR. As a consequence, the applications built on this function such as image quality measurement and resolution estimation are limited to NB SAR cases. A more general IRF-SAR, which aims at UWB SAR systems, is derived with an assumption of the flat 2-D FT of a SAR image and called IRF-USAR.

8.2 Part I–B - On synthetic aperture radar azimuth and range resolution equations

A discussion on spatial resolutions for UWB SAR in comparison to NB SAR is given in this study. The similarity between the behavior of IRF-NSAR and IRF-USAR in azimuth and range is found in the intensity interval from -6 dB to 0 dB. This similarity is employed in a derivation of new spatial resolution equations for UWB SAR based on -3 dB width or HPBW. The effects of the signal fractional bandwidth and the associated integration angle to HPBW are described by the HPBW narrowing/broadening factors which are included in the new derived resolution equations.

8.3 Part I–C - Definition on SAR image quality measurements for UWB SAR

This study points out that measurements under currently used definitions of SAR image quality measurement may be unsuitable for UWB SAR. The main objective of the study is therefore to propose a new definition which is more suitable for UWB SAR. To propose as well as validate the assessments in the definition, it is necessary to use both real and simulated UWB SAR data.

8.4 Part II–A - RFI suppression in ultrawideband SAR using adaptive line enhancer

An approach to suppress RFI in UWB low frequency SAR is introduced in this study. According to the proposal, RFI suppression is performed by ALE whose filter coefficients are adaptively updated by an NLMS algorithm. The

proposed approach is examined with real UWB low frequency SAR data. A possibility to integrate this approach into SAR imaging algorithms is also suggested.

8.5 Part II–B - A comparison between fast factorized backprojection and frequency-domain algorithms in UWB low frequency SAR

Two frequency-domain algorithms, CS with the superiority in processing time and RM with possibly minimized phase errors are candidates for a comparative study to the time-domain algorithm FFBP. The performance of these algorithms with UWB low frequency SAR data is focused in this study. The comparison is based on the standard image quality assessments such as spatial resolutions, ISLR and PSLR, and processing time affected by the computational complexity.

8.6 Part II–C - On apodization techniques for ultrawideband SAR imaging

This study presents a discussion about apodization or sidelobe control for UWB SAR which is one of the practical issues in UWB SAR data processing. The applicability of different NB SAR apodization techniques, e.g. linear and nonlinear apodization, to UWB SAR are first examined. The study is followed by evaluations for the performance of these apodization techniques in the UWB SAR environment.

8.7 Part III–A - Detection of moving targets by focusing in UWB SAR – Theory and experimental results

The theory on moving target detection by focusing and the experimental results on single-channel SAR data are presented in this study. The detection technique is based on the fact that a moving target can be considered to be stationary in a SAR formation process if the SAR platform is processed with the difference velocity of the original platform velocity and the target velocity. For detection, different hypotheses (so-called NRS under test) have to be tested until the detection is reached. The experimental results show that the ability to detect moving targets increases significantly when applying the proposed detection technique. The improvement in SCNR which is a basic

requisite for evaluating the performance reaches approximately 20 dB using only single-channel SAR data. This gain will be preserved for the case of multi-channel SAR data.

8.8 Part III–B - Fast detection of moving targets by focusing in UWB low frequency SAR

The moving target detection technique shows some limits in processing. One of the factors contributing to the processing time of the detection technique is the GBP algorithm which is employed as a basis for the focusing approach. This algorithm requires a high computational cost. The fast detection of moving target by focusing method is introduced in this study. The method is based on the moving target detection technique incorporating fast time-domain algorithms in the process. Two fast time-domain algorithms considered in this study are FBP and FFBP.

8.9 Part III–C - Integrating space-time processing into time-domain backprojection process to detect and image moving objects

This paper presents a method to integrate space-time processing techniques into the time-domain backprojection process. The integration allows detecting moving objects and reconstructing the SAR images of those moving objects. Two space-time processing techniques considered for this integration are DPCA and STAP. The integration partially meets the strict requirements of DPCA and improves the computational practicality of STAP.

References

- [1] V. T. Vu, T. K. Sjögren, M. I. Pettersson, L. M. H. Ulander, and A. Gustavsson, "Moving targets detection by focusing in UWB SAR - Theory and experimental results," *IEEE Trans. Geosci. Remote Sensing*, vol. 48, no. 10, pp. 3799–3815, 2010.
- [2] A. Gustavsson, L. M. H. Ulander, B. H. Flood, P.-O. Frölind, H. Hellsten, T. Jonsson, B. Larsson, and G. Stenstrom, "Development and operation of an airborne VHF SAR system-lessons learned," in *Proc. IEEE IGARSS'98*, vol. 1, Seattle, US, Jul. 1998, pp. 458–462.

- [3] R. Goodman, S. Tummala, and W. Carrara, "Issues in ultra-wideband, widebeam SAR image formation," in *Proc. IEEE International Radar Conference*, Alexandria, US, May 1995, pp. 479–485.
- [4] V. T. Vu, *Practical considerations in ultrawideband synthetic aperture radar*, Licentiate dissertation, Blekinge Institute of Technology, Karlskrona, Sweden, Nov. 2009, ISBN 978-91-7295-171-6.
- [5] L. M. H. Ulander and H. Hellsten, "Low-frequency ultrawideband array-antenna SAR for stationary and moving target imaging," in *Proc. SPIE Radar Sensor Technology IV*, vol. 3704, Orlando, US, Apr. 1999, pp. 149–158.
- [6] D. R. Sheen, N. L. VandenBerg, S. J. Shackman, D. L. Wiseman, L. P. Elenbogen and R. F. Rawson, "P-3 ultra-wideband SAR: description and examples," *IEEE Aerosp. Electron. Syst. Magazine*, vol. 11, no. 11, pp. 25–30, 1996.
- [7] R. Baque, G. Bonin and O. Ruault du Plessis, "The airborne SAR-system: SETHI airborne microwave remote sensing imaging system," in *Proc. International Radar Conference*, Bordeaux, France, Oct. 2009, pp. 1–5.
- [8] S. Buckreuss, W. Balzer, P. Muhlbauer, R. Werninghaus and W. Pitz, "The terraSAR-X satellite project," in *Proc. IEEE IGARSS'03*, Toulouse, France, July 2003, pp. 3096–3098.
- [9] L. Candela, F. Caltagirone, "COSMO-SkyMed: Mission definition and main application and products," in *Proc. POLinSAR 2003 Workshop*, Frascati, Italy, Jan. 2003, pp. 35.1–35.26.
- [10] Sang-Ryool Lee, "Overview of KOMPSAT-5 program, mission, and system," in *Proc. IEEE IGARSS'10*, Honolulu, US, July 2010, pp. 797–800.
- [11] M. Faisal, *Building a GB-SAR system and perform basic and advance measurements for a fixed target*, Master Thesis, Blekinge Institute of Technology, Karlskrona, Sweden, Oct. 2011.
- [12] Federal Communications Commission (FCC), "Revision of part 15 of the commission's rules regarding ultra-wideband systems: First report and order," FCC 02-48, April 2002, pp. 36.

- [13] J. H. G. Ender and A. R. Brenner, "PAMIR - a wideband phased array SAR/MTI system," *IEE Proc.-Radar Sonar and Navigation*, vol. 150, no. 3, pp. 165–172, 2003.
- [14] L. M. H. Ulander, M. Lundberg, W. Pierson, and A. Gustavsson, "Change detection for low-frequency SAR ground surveillance," *IEE Proc.-Radar Sonar and Navigation*, vol. 152, no. 6, pp. 423–420, 2005.
- [15] J. E. S. Fransson, G. Smith, F. Walter, A. Gustavsson, and L. M. H. Ulander, "Estimation of forest stem volume in sloping terrain using CARABAS-II VHF SAR data," *Canadian Journal Remote Sensing*, vol. 30, no. 4, pp. 651–660, 2004.
- [16] B. Hallberg, G. Smith-Jonforsen, and L. M. H. Ulander, "Measurements on individual trees using multiple VHF SAR images," *IEEE Trans. Geosci. Remote Sensing*, vol. 43, no. 10, pp. 2261–2269, 2005.
- [17] P.-O. Fröling and L. M. H. Ulander, "Digital elevation map generation using VHF-band SAR data in forested areas," *IEEE Trans. Geosci. Remote Sensing*, vol. 40, no. 8, pp. 1769–1776, 2002.
- [18] T. K. Sjögren, V. T. Vu, M. I. Pettersson, H.-J. Zepernick, and A. Gustavsson, "Speed estimation experiments for ground moving targets in UWB SAR," in *Proc. IET RADAR'2007*, Edinburgh, UK, Oct. 2007, pp. 519–523.
- [19] M. I. Pettersson, "Extraction of Moving Ground Targets by a Bistatic Ultra-Wideband SAR," *IEE Proc.-Radar Sonar and Navigation*, vol. 148, no. 1, pp. 35–40, 2001.
- [20] V. T. Vu, T. K. Sjögren, M. I. Pettersson, and H. Hellsten, "An impulse response function for evaluation of UWB SAR imaging," *IEEE Trans. Signal Processing*, vol. 58, no. 7, pp. 3927–3932, 2010.
- [21] W. M. Brown, "Synthetic aperture radar," *IEEE Trans. Aerosp. Electron. Syst.*, vol. AES-3, pp. 217–229, 1967.
- [22] M. I. Skolnik, *Radar handbook*, 3rd ed, McGraw-Hill, 1990.
- [23] V. T. Vu, T. K. Sjögren, and M. I. Pettersson, "On synthetic aperture radar azimuth and range resolution equations," *IEEE Trans. Aerosp. Electron. Syst.*, accepted for publication.

- [24] L. M. H. Ulander and H. Hellsten, “A new formula for SAR spatial resolution,” *AEÜ International Journal of Electronics and Communications*, vol. 50, no. 2, pp. 117–121, 1996.
- [25] A. Martinez and J. L. Marchand, “SAR image quality assessment,” *Asoc. Española de Teledetección Revista de Teledetección*, no. 2, pp. 12–18, 1993.
- [26] JPL SIR-C Team, DLRNE-HF X-SAR Team, and I-PAF X-SAR Team, “Data products and image quality specifications for the SIR-C/X-SAR mission,” JPL Document D-7193, Mar. 1990.
- [27] Envisat ASAR Cal/Val Team, “Quality measurements definition for ASAR level 1 products,” ESA, Tech. Rep. Issue 1, Mar. 2002.
- [28] V. T. Vu, T. K. Sjögren, M. I. Pettersson, and A. Gustavsson, “Definition on SAR image quality measurements for UWB SAR,” in *Proc. SPIE Image and Signal Processing for Remote Sensing XIV*, vol. 7109, Cardiff, UK, Sep. 2008, pp. 71091A1–71091A9.
- [29] S. K. Das, *Synthetic aperture radar image quality measurements*, Master Thesis, Blekinge Institute of Technology, Karlskrona, Sweden, July 2011.
- [30] V. T. Vu, T. K. Sjögren, M. I. Pettersson, L. Håkansson, A. Gustavsson, and L. M. H. Ulander, “RFI suppression in ultrawideband SAR using adaptive line enhancer,” *IEEE Geosci. Rem. Sens. Lett.*, vol. 7, no. 4, pp. 694–698, 2010.
- [31] L. M. H. Ulander, and P.-O. Frölind “Precision processing of CARABAS HF/VHF-band SAR data,” in *Proc. IEEE IGARSS’99*, vol. 1, Hamburg, Germany, Jun. 1999, pp. 47–49.
- [32] Monson H. Hayes, in *Statistical Digital Signal Processing and Modeling*, Willey, 1996, pp. 514–521.
- [33] C. T. Le, S. Hensley and E. Chapin, “Adaptive filtering of RFI in wideband SAR signals,” in *7th Annual JPL AirSAR Workshop*, Jan. 1997.
- [34] X. Luo, L.M.H. Ulander, J. Askne, G. Smith, and P.-O. Frolind, “RFI suppression in ultra-wideband SAR systems using LMS filters infrequency domain,” *IET Electronics Letters*, vol. 37, no. 4, pp. 241–243, 2001.

- [35] V. T. Vu, T. K. Sjögren, M. I. Pettersson, and L. Håkansson, “An approach to suppress RFI in ultrawideband low frequency SAR,” in *Proc. IEEE Radar 2010*, Washington, US, May 2010, pp. 1381–1385.
- [36] K. F. Ullah, *RFI suppression in low frequency UWB SAR using the RLS algorithm*, Master Thesis, Blekinge Institute of Technology, Karlskrona, Sweden, Dec. 2010.
- [37] J. R. Bennett and I. G. Cumming, “Digital processor for the production of Seasat synthetic aperture radar imagery,” in *Proc. Proc. Internationall Conference On Seasat-SAR Processor*, Frascati, Italy, Dec. 1979, ESA-SP-154.
- [38] C. Cafforio, C. Prati, and F. Rocca, “SAR data focusing using seismic migration techniques,” *IEEE Trans. Aerosp. Electron. Syst.*, vol. 27, pp. 194–207, Mar. 1991.
- [39] R. K. Raney, H. Runge, R. Bamler, I. G. Cumming, and F. H. Wong, “Precision SAR processing using chirp scaling,” *IEEE Trans. Geosci. Remote Sensing*, vol. 32, no. 4, pp. 786–799, 1994.
- [40] R. Stolt, “Migration by Fourier transform,” *Geophysics*, vol. 43, no. 1, pp. 23–48, 1978.
- [41] G. W. Davidson, I. G. Cumming, and M. R. Ito, “A chirp scaling approach for processing squint mode SAR data,” *IEEE Trans. Aerosp. Electron. Syst.*, vol. 32, no. 1, pp. 121–133, 1996.
- [42] A. Moreira, J. Mittermayer, R. Scheiber, “Extended chirp scaling algorithm for air- and spaceborne SAR data processing in stripmap and scanSAR imaging modes,” *IEEE Trans. Geosci. Remote Sensing*, vol. 34, no. 5, pp. 1123–1136, 1996.
- [43] V. T. Vu, T. K. Sjögren, and M. I. Pettersson, “Ultrawideband chirp scaling algorithm,” *IEEE Geosci. Rem. Sens. Lett.*, vol. 7, no. 2, pp. 281–285, 2010.
- [44] L. E. Andersson, “On the determination of a function from spherical averages,” *SIAM Journal on Mathematical Analysis*, vol. 19, no. 1, pp. 214–232, 1988.

- [45] O. Seger, M. Herberthson, and H. Hellsten, "Real time SAR processing of low frequency ultra wide band radar data," in *Proc. EUSAR'98*, Friedrichshafen, Germany, May 1998, pp. 489–492.
- [46] A. F. Yegulalp, "Fast backprojection algorithm for synthetic aperture radar," in *Proc. IEEE RadarCon'99*, Waltham, US, Apr. 1999, pp. 60–65.
- [47] L. M. H. Ulander, H. Hellsten, and G. Stenstrom, "Synthetic-aperture radar processing using fast factorized back-projection," *IEEE Trans. Aerosp. Electron. Syst.*, vol. 39, no. 3, pp. 760–776, 2003.
- [48] V. T. Vu, T. K. Sjögren, and M. I. Pettersson, "A comparison between fast factorized backprojection and frequency-domain algorithms in UWB low frequency SAR," in *Proc. IEEE IGARSS'2008*, Boston, US, Jul. 2008, pp. IV-1284–IV-1287.
- [49] H. Yves, *A study of fast backprojection algorithm for UWB SAR and a comparison between fast- and global backprojection*, Master Thesis, Blekinge Institute of Technology, Ronneby, Sweden, Nov. 2008.
- [50] I. Ahmed, *Study of the local backprojection algorithm for image formation in ultrawideband synthetic aperture radar*, Master Thesis, Blekinge Institute of Technology, Ronneby, Sweden, Dec. 2008.
- [51] T. K. Sjögren, V. T. Vu, and M. I. Pettersson, "A comparative study of the polar version with the subimage version of fast factorized backprojection in UWB SAR," in *Proc. IEEE IRS'08*, Wroclaw, Poland, May 2008, pp. 156–159.
- [52] O. Frey, C. Magnard, M. Rüegg, and E. Meier, "Focusing of airborne synthetic aperture radar data from highly non-linear flight tracks," *IEEE Trans. Geosci. Remote Sensing*, vol. 47, no. 6, pp. 1844–1858, 2009.
- [53] H. C. Stankwitz, R. J. Dallaire, and J. R. Fienup, "Nonlinear apodization for sidelobe control in SAR imagery," *IEEE Trans. Aerosp. Electron. Syst.*, vol. 31, no. 1, pp. 267–279, 1995.
- [54] X. Xu and R. M. Narayanan, "Enhanced resolution in SAR/ISAR imaging using iterative sidelobe apodization," *IEEE Trans. Image Processing*, vol. 14, no. 4, pp. 537–547, 2005.

- [55] V. T. Vu, T. K. Sjögren, and M. I. Pettersson, "On apodization techniques for ultra-wideband SAR imaging," in *Proc. EURAD'2009*, Roma, Italy, Sep. 2009, pp. 529–532.
- [56] T. K. Sjögren, V. T. Vu, and M. I. Pettersson, "Optimum linear apodization for UWB SAR imaging," *IEEE Trans. Signal Processing*, submitted for publication.
- [57] M. Kirsch, "Detection and imaging of arbitrarily moving targets with single-channel SAR," *IEE Proc.-Radar Sonar and Navigation*, vol. 150, no. 1, pp. 7–11, 2003.
- [58] M. Jahangir and C. P. Moate, "Utilising signal absence in SAR imagery for moving target detection," in *The IET Forum on Waveform Diversity and Design in Communications, Radar and Sonar*, London, UK, Nov. 2006, pp. 41–46.
- [59] J. R. Fienup, "Detecting moving targets in SAR imagery by focusing," *IEEE Trans. Aerosp. Electron. Syst.*, vol. 37, no. 3, pp. 749–809, 2001.
- [60] J. H. G. Ender, "Space-time processing for multichannel synthetic aperture radar," *IEE Electronics & Communication Engineering Journal*, vol. 11, no. 1, pp. 29–38, 1999.
- [61] L. E. Brennan, J. D. Mallett, and I. S. Reed, "Adaptive arrays in airborne MTI radar," *IEEE Trans. Antennas Propagat.*, vol. 24, no. 5, pp. 607–615, 1976.
- [62] V. T. Vu, T. K. Sjögren, M. I. Pettersson, H.-J. Zepernick, and A. Gustavsson, "Experimental results on moving targets detection by focusing in UWB low frequency SAR," in *Proc. IET RADAR'2007*, Edinburgh, UK, Oct. 2007, pp. 562–566.
- [63] V. T. Vu, T. K. Sjögren, M. I. Pettersson, and P. A. C. Marques, "Application of moving target detection by focusing technique in civil traffic monitoring," in *Proc. IEEE IGARSS'2010*, Honolulu, US, Jul. 2010, pp. 4118–4121.
- [64] J. K. Jao, "Theory of synthetic aperture radar imaging of a moving target," *IEEE Trans. Geosci. Remote Sensing*, vol. 39, no. 9, pp. 1984–1992, 2001.

- [65] M. I. Pettersson, "Detection of moving targets in wideband SAR," *IEEE Trans. Aerosp. Electron. Syst.*, vol. 40, no. 3, pp. 780–796, 2004.
- [66] M. I. Pettersson, "Optimum relative speed discretisation for detection of moving objects in wide band SAR," *IET Radar, Sonar & Navigation*, vol. 1, no. 3, pp. 213–220, 2007.
- [67] V. T. Vu, T. K. Sjögren, and M. I. Pettersson, "Moving target detection by focusing for frequency domain algorithms in UWB low frequency SAR," in *Proc. IEEE IGARSS'2008*, Boston, US, Jul. 2008, pp. I-161–I-164.
- [68] S. Rahman, *Focusing moving targets using range migration algorithm in ultrawideband low frequency synthetic aperture radar*, Master Thesis, Blekinge Institute of Technology, Karlskrona, Sweden, June 2010.
- [69] T. K. Sjögren, V. T. Vu, and M. I. Pettersson, "Moving target refocusing algorithm for synthetic aperture radar images," in *Proc. IEEE IGARSS'2010*, Honolulu, US, Jul. 2010, pp. 4110–4113.
- [70] T. K. Sjögren, V. T. Vu, M. I. Pettersson, A. Gustavsson, and L. M. H. Ulander, "Moving target relative speed estimation and refocusing in synthetic aperture radar images," *IEEE Trans. Aerosp. Electron. Syst.*, accepted for publication.
- [71] V. T. Vu, T. K. Sjögren, and M. I. Pettersson, "Fast detection of moving targets by focusing in UWB low frequency SAR," in *Proc. IEEE Radar-Con'2009*, Pasadena, US, May 2009, pp. 1–5.
- [72] V. T. Vu, T. K. Sjögren, and M. I. Pettersson, "Fast detection of moving targets by focusing in multi-channel Ultra-wideband SAR," in *EuRAD 2009*, Rome, Italy, Sep. 2009, pp. 218–241.
- [73] V. T. Vu, T. K. Sjögren, and M. I. Pettersson, "Integrating space-time processing into time-domain backprojection process to detect and image moving objects," in *Proc. IEEE IGARSS'2010*, Honolulu, US, Jul. 2010, pp. 4106–4109.

Part I—A

Part I-A

An Impulse Response Function for
Evaluation of UWB SAR Imaging

Part I–A is published as:

V. T. Vu, T. K. Sjögren, M. I. Pettersson, and H. Hellsten “An impulse response function for evaluation of ultrawideband SAR imaging,” *IEEE Trans. Signal Processing*, vol. 58, no. 7, pp. 3927–3932, 2010.

An Impulse Response Function for Evaluation of UWB SAR Imaging

V. T. Vu, T. K. Sjögren, M. I. Pettersson and H. Hellsten

Abstract

Based on analysis of a point target imaged by different Synthetic Aperture Radar (SAR) systems, the commonly used Impulse Response Function in SAR Imaging (IRF-SAR) - a two-dimensional (2-D) *sinc* function - is shown to be inappropriate for ultrawideband-ultrawidebeam (UWB) SAR systems utilizing a large fractional signal bandwidth and a wide antenna beamwidth. As a consequence, the applications of the 2-D *sinc* function such as image quality measurements and spatial resolution estimations are limited to narrowband-narrowbeam (NB) SAR systems exploiting a small fractional signal bandwidth and a narrow antenna beamwidth. In this paper, a more general IRF-SAR, which aims at UWB SAR systems, is derived with an assumption of flat two-dimensional (2-D) Fourier Transform (FT) of a SAR image and called IRF-USAR. However, the derived IRF-USAR is also valid for NB SAR systems.

1 Introduction

Synthetic Aperture Radar (SAR) is widely used as ground-imaging radars. SAR has its own surface illuminating capability that allows it to work in hazy weather (fog, rain etc.) and even in the night. During such unfavorable weather condition, most other remote sensing systems are inefficient. Ultrawideband-ultrawidebeam (UWB) SAR systems utilizing a large fractional signal bandwidth and a wide antenna beamwidth associated with very long integration time or wide integration angle enable large scene and/or high resolution imaging. The fractional bandwidth is defined by the ratio of the bandwidth to the center frequency while the integration angle by the angle between two vectors from the point target to the first and the last aperture

positions. One example of experimental UWB SAR systems is CARABAS-II [1] operating in the lower VHF-band from 20 to 90 MHz and using wide beamwidth dipole antennas (larger than 90°). Other systems such as LORA operating in the VHF/UHF-bands from 200 to 800 MHz [2], P-3 with a bandwidth of 515 MHz in the VHF/UHF-bands 215-900 MHz [3], ground-based BoomSAR with a spectral response extending from 50 MHz to 1200 MHz [4] and PAMIR with a very high bandwidth of 1820 MHz in X-band [5] are also known as UWB SAR systems. Inherent challenges in UWB SAR data processing in general and UWB SAR imaging in particular have been clearly pointed out in [6] where the choice of processing algorithm, sidelobe control or apodization, motion error compensation and Radio Frequency Interference (RFI) suppression are listed. Some developed approaches for such problems can be found in [7]-[10]. However, another issue, which is significantly important but has not been either mentioned or investigated in earlier publications, is the Impulse Response Function in SAR imaging (IRF-SAR) for UWB SAR.

The commonly used IRF-SAR is known as a two-dimensional (2-D) *sinc* function. This function in image-domain is obtained from the 2-D Inverse Fourier Transform (IFT) of a 2-D *rect* function in wave-domain which is an approximation for the 2-D Fourier Transform (FT) of a SAR image of a point target. For narrowband-narrowbeam (NB) SAR systems utilizing a small fractional bandwidth and a narrow antenna beamwidth, this IRF-SAR is shown to be a good approximation. Important applications of the 2-D *sinc* function are found in SAR image quality measurements [11]-[13] as well as SAR spatial resolution estimations [14]-[16]. However, such the applications are limited to the NB SAR systems. For a UWB SAR system utilizing a large fractional signal bandwidth and a wide integration angle, the 2-D Fourier Transform (FT) of a SAR image of a point target is very different from the 2-D *rect* function. The complicated behavior of the Impulse Response in SAR imaging (IR-SAR), which refers to a SAR image of a point target, cannot therefore be represented by the 2-D *sinc* function in image-domain. Applying a 2-D *rect* function to the 2-D Fourier Transform (FT) of a SAR image can result in a 2-D *rect* function in wave-domain and therefore a 2-D *sinc* function in image-domain. However, this also lead to extremely high loss in SAR spatial resolutions [10]. Such situation will therefore not be considered here. To the knowledge of the authors, there has been neither mathematical representation of IRF-SAR other than the 2-D *sinc* function nor investigation into the validity of the 2-D *sinc* function for SAR systems using large fractional signal bandwidths and wide integration angles.

Table 1: The parameters of the simulated SAR systems.

	System 1	System 2	System 3
Fractional bandwidth B_r	0.1	0.35	1.1
Integration angle ϕ_0	10°	35°	110°

The main objective of this paper is to derive a new IRF-SAR, which can be used for evaluation of UWB SAR imaging. In the context of this paper, the derived IRF-SAR is denoted by IRF-USAR which stands for Impulse Response Function in UWB SAR imaging. Similarly, IRF-NSAR, which stands for Impulse Response Function in NB SAR imaging, is used for the 2-D *sinc* function. The IRF-USAR is derived with the assumption that the flat 2-D FT of a SAR image of a point target is flat and the derivation is limited to the monostatic case. In spite of aiming at UWB SAR systems, the derived IRF-SAR is valid for NB SAR systems.

The paper is organized as follows. Section 2 shows an analysis based on a point target imaged by SAR systems with various fractional bandwidths and integration angles. Motivated by the analysis in Section 2, the IRF-USAR is derived in Section 3. Section 4 presents some basic investigations based on the derived IRF-USAR. Section 5 summarizes the contributions of the paper.

2 Analysis on Point Target

In this section, we present an analysis based on a point target, which is illuminated by some SAR systems utilizing different fractional signal bandwidths and different integration angles. The main parameters of these SAR systems are summarized in Table 1. The reason for this analysis is explained by the fact that the SAR system parameters decide how the point target appears in a SAR image, which directly connects to IRF-SAR. The analysis is based on simulated data to avoid undesired effects such as impacts of antenna pattern, clutter backscattering, noise and local reflection which may be caused by incompletely calibrated SAR systems. Also, no apodization technique is applied. Image quality has a high priority in this study and it is known that both Global Backprojection (GBP) [17] and Range Migration (RM) [18] are good candidates for UWB SAR imaging in terms of quality. However, we use

GBP in this study due to its advanced characteristics such as local processing and manageable motion error compensation.

In this analysis, we call sidelobes in the azimuth and range directions orthogonal sidelobes. Sidelobes in other directions, i.e. neither in the azimuth nor range directions, are called non-orthogonal sidelobes. The azimuth and range directions correspond with vertical and horizontal axes of Cartesian coordinates, respectively. In polar coordinates, they correspond with the angles of 90° and 0°, respectively.

In Fig. 1, the simulation results of a point target, which is imaged by the SAR systems in Table 1, are provided. Fig. 1.a and 1.b show an example of a point target imaged by a NB SAR system $h_1(x, y)$ and its 2-D FT $H_1(k_x, k_y)$, respectively. The azimuth and range are denoted by x and r while k_x and k_y indicate azimuth and range wavenumbers and are connected together by the relation

$$\omega = \frac{c}{2} \sqrt{k_x^2 + k_y^2}, \quad (1)$$

where ω is the signal frequency and c is the speed of light. The relation between a SAR image of a point target $h(x, y)$ in image-domain and its 2-D FT $H(k_x, k_y)$ in wave-domain are generally represented by

$$H(k_x, k_y) = \int_{-\infty}^{+\infty} \int_{-\infty}^{+\infty} h(x, y) \cdot e^{-j(k_x x + k_y y)} dx dy. \quad (2)$$

Conversely, a SAR image of a point target $h(x, y)$ is represented by the 2-D IFT of $H(k_x, k_y)$ as

$$h(x, y) = \frac{1}{(2\pi)^2} \int_{-\infty}^{+\infty} \int_{-\infty}^{+\infty} H(k_x, k_y) \cdot e^{j(k_x x + k_y y)} dk_x dk_y. \quad (3)$$

In this simulation, the NB SAR system possesses a fractional bandwidth $B_r = 0.1$ and an integration angle $\phi_0 = 10^\circ$. The 2-D FT of the SAR image $h_1(x, y)$ can be approximated by a 2-D *rect* function. With the assumption of the flat 2-D FT of the SAR image, $H_1(k_x, k_y)$ of the point target imaged by the NB SAR system is given by

$$H_1(k_x, k_y) \approx \begin{cases} 1 & k_{x,min} \leq k_x \leq k_{x,max} \\ & k_{y,min} \leq k_y \leq k_{y,max} \\ 0 & \text{elsewhere} \end{cases}. \quad (4)$$

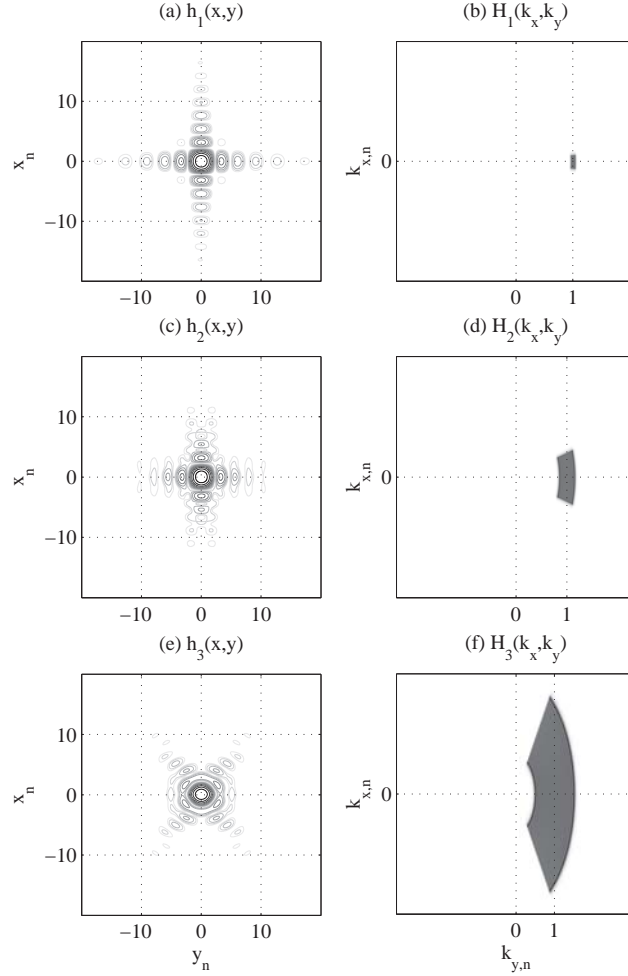


Figure 1: Images of the point target illuminated by the different simulated SAR systems in Table 1 and their 2-D FT. The figures on the left hand side plot contours from -30 dB to -3 dB with a 3 dB step and on the right hand side the associated 2-D FT. The SAR image coordinates x_n and y_n denote normalized azimuth and range with respect to -3 dB widths. $k_{x,n}$ and $k_{y,n}$ denote normalized wavenumbers with respect to the center wave number k_c . (a) and (b) NB SAR with $B_r = 0.1$ and $\phi_0 = 10^\circ$. (c) and (d) UWB SAR with $B_r = 0.35$ and $\phi_0 = 35^\circ$. (e) and (f) UWB SAR with $B_r = 1.1$ and $\phi_0 = 110^\circ$.

With this approximation, Equation (3) results in a normalized SAR image in the coordinates x and y which can be mathematically represented by

$$h_1(x, y) \approx \text{sinc}\left(k_c x \sin \frac{\phi_0}{2}\right) \cdot \text{sinc}\left(\frac{k_{y,\max} - k_{y,\min}}{2} y\right), \quad (5)$$

where $k_{y,c}$ is the center wavenumber and ϕ_0 is the integration angle. Equation (5) is known as the IRF-NSAR. The similarity between IRF-NSAR and the SAR image given in Fig. 1.a can be observed. The orthogonal sidelobes in the SAR image are predominated and there is no non-orthogonal sidelobe.

The investigations into the the 2-D FT of the SAR image NB SAR image can also be based on models which have been proposed in [19] for the monostatic case and in [20, 21] for the bistatic case.

The point target is then illuminated by another SAR system and this time it utilizes a large fractional bandwidth $B_r = 0.35$ and an wide integration angle $\phi_0 = 35^\circ$. As shown in Fig. 1.d, the 2-D FT of the SAR image $H_2(k_x, k_y)$ is different from a 2-D *rect* function. As consequence, using (5) for IRF-SAR in this case needs to be examined. The effects of fractional bandwidth and integration angle to IR-SAR can be initially observed in Fig. 1.c. The orthogonal sidelobes in the range direction start to get broader compared to Fig. 1.a. In the azimuth direction, the orthogonal sidelobes begin to attenuate and are separated into symmetric non-orthoganal sidelobes.

In the last example, we simulate the existing UWB SAR system with an extremely large fractional bandwidth $B_r = 1.1$ and an extremely wide integration angle $\phi_0 = 110^\circ$. The 2-D FT of the SAR image $H_3(k_x, k_y)$ shown in Fig. 1.f is clearly seen not to be a 2-D *rect* function. However, it can be seen as a set of one-dimensional (1-D) *rect* functions with the same window lengths and organized in angle of the polar coordinates. Thus, (5) cannot be used to represent the IRF-SAR for such SAR system. The point target illuminated by this UWB SAR system is plotted in Fig. 1.e where the broadening of the range sidelobes and the strong attenuation associated with the separation of the azimuth sidelobes are observed. As a consequence of this attenuation, the orthogonal sidelobes in the azimuth direction disappear.

3 IRF-USAR

The analysis given in Section 2 shows that the 2-D FT of the SAR images $H(k_x, k_y)$ resulted by the SAR systems 2 and 3 in Table 1 should be represented by a more accurate form, which complies with the relation (1), instead

of the approximate form given by (4). A flat image spectrum in wave-domain is a natural choice due to the similarities to the derivation of IRF-NSAR as well as the minimization of the -3 dB beamwidth in image-domain. Hence, a more accurate form for these SAR image spectra in the polar coordinates (κ, ϕ) can basically be given by

$$H(\kappa, \phi) = \begin{cases} 1 & -\phi_0/2 \leq \phi \leq \phi_0/2 \\ \kappa_{min} \leq \kappa \leq \kappa_{max} & \\ 0 & \text{elsewhere} \end{cases}, \quad (6)$$

where

$$\begin{aligned} \kappa_{min} &= k_{y,min} & \text{when } k_x = 0 \\ \kappa_{max} &= k_{y,max} & \text{when } k_x = 0. \end{aligned} \quad (7)$$

Without losing generality, we can normalize κ with respect to the center wave-number k_c . Hence, (6) can be rewritten as

$$H(\varrho, \phi) = \begin{cases} 1 & -\phi_0/2 \leq \phi \leq \phi_0/2 \\ 1 - B_r/2 \leq \varrho \leq 1 + B_r/2 & \\ 0 & \text{elsewhere} \end{cases}, \quad (8)$$

where B_r denotes the fractional bandwidth. With the approximate 2-D FT of the SAR image given in (8), the integral (3) is calculated in the polar coordinates (ϱ, ϕ) and the IRF-USAR is shown to be (see Appendix A)

$$\begin{aligned} h(\rho, \varphi, B_r, \phi_0) = & \\ \frac{e^{-i\varphi}}{\rho} \left[\phi_0 \sum_{n=-\infty}^{+\infty} \frac{i^n h_{j,n-1}(\rho, B_r)}{e^{i(n-1)\varphi}} \text{sinc}\left(n \frac{\phi_0}{2}\right) \right] \\ + \frac{e^{-i\varphi}}{\rho} h_s(\rho, \varphi, B_r, \phi_0), \end{aligned} \quad (9)$$

where

$$\begin{aligned} h_{j,n-1}(\rho, B_r) = & - \left(1 + \frac{B_r}{2}\right) J_{n-1} \left[\rho \left(1 + \frac{B_r}{2}\right)\right] \\ & + \left(1 - \frac{B_r}{2}\right) J_{n-1} \left[\rho \left(1 - \frac{B_r}{2}\right)\right] \end{aligned} \quad (10)$$

and

$$\begin{aligned} h_s(\rho, \varphi, B_r, \phi_0) = & \\ & -B_r \text{sinc} \left[\frac{B_r}{2} \rho \cos \left(\frac{\phi_0}{2} + \varphi \right) \right] e^{i\rho \cos(\frac{\phi_0}{2} + \varphi) - i\frac{\phi_0}{2}} \\ & + B_r \text{sinc} \left[\frac{B_r}{2} \rho \cos \left(\frac{\phi_0}{2} - \varphi \right) \right] e^{i\rho \cos(\frac{\phi_0}{2} - \varphi) + i\frac{\phi_0}{2}}. \end{aligned} \quad (11)$$

In (9), the azimuth direction corresponds to $\varphi = 0^\circ$ and for the range direction $\varphi = 90^\circ$. For approximate calculation of (9), the accuracy depends strongly on the attenuation of $\text{sinc}(n\phi_0/2)$. At large integration angles, this *sinc* function attenuates faster than at small integration angles. For example, if $\phi_0 = 110^\circ$, it is not necessary to consider the values of n beyond the range $-30 \leq n \leq 30$ while this range must be extended, e.g. $-300 \leq n \leq 300$ for $\phi_0 = 10^\circ$.

The derived IRF-USAR (9) can be simplified for particular SAR configurations. In the following example, we consider a circular aperture, i.e. $\phi_0 = 360^\circ$. Since

$$\text{sinc} \left(n \frac{\phi_0}{2} \right) = \begin{cases} 1 & n = 0 \\ 0 & \text{elsewhere} \end{cases} \quad (12)$$

and

$$h_2(\rho, \varphi, B_r, \phi_0 = 360^\circ) = 0,$$

the derived IRF-SAR (9) is no longer a function of φ and can be rewritten as

$$\begin{aligned} h(\rho, B_r, \phi_0 = 360^\circ) = & \\ & -\frac{\phi_0}{\rho} \left(1 + \frac{B_r}{2} \right) J_{-1} \left[\rho \left(1 + \frac{B_r}{2} \right) \right] \\ & + \frac{\phi_0}{\rho} \left(1 - \frac{B_r}{2} \right) J_{-1} \left[\rho \left(1 - \frac{B_r}{2} \right) \right]. \end{aligned} \quad (13)$$

The IRF-USAR in this particular SAR configuration results in a circularly symmetric pattern which is known as a typical pattern for circular apertures [22].

4 Evaluations of the Derived IRF-USAR

The derived IRF-USAR in Section 3 is first used to examine the validity of the IRF-NSAR in representing the complicated behavior of IR-SAR in both

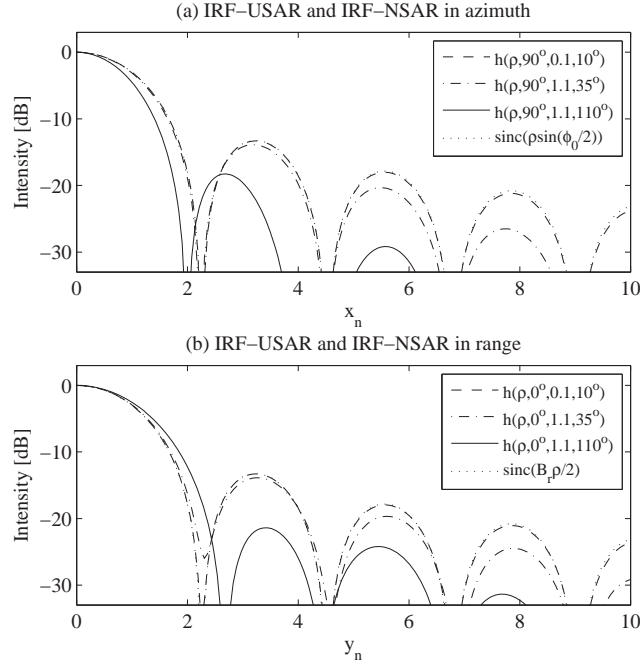


Figure 2: Plots of $h(\rho, \varphi, B_r, \phi_0)$ with different values of the fractional bandwidths B_r and the integration angle ϕ_0 given in Table 1. The intensities of IRF-USAR are normalized with respect to their peak intensity and in the dB scale. The horizontal axes in the plots are rescaled with respect to the -3 dB beamwidths of the sinc functions given in (5). The rescaled azimuth and range are denoted by x_n and y_n , respectively. The IRF-NSAR are also plotted for evaluation purposes. (a) in azimuth. (b) in range.

azimuth and range directions with respect to large fractional signal bandwidth and wide integration angle. In reality, IR-SAR in azimuth and range directions are normally extracted at the peak intensity belonging to the mainlobe of a single point target in a SAR image. For NB SAR systems, these IR-SAR are approximately given by the former and later *sinc* functions in 5. Relied on the derived IRF-USAR in Section 3, the IR-SAR in azimuth and range directions are approximately found from the functions $h(\rho, 90^\circ, B_r, \phi_0)$ and $h(\rho, 0^\circ, B_r, \phi_0)$, respectively.

Fig. 2 plots the derived IRF-USAR associated with the SAR systems in Table 1. In the plots, normalized terms are used for evaluation purposes. The intensities of IRF-USAR are normalized with respect to their peak intensity and represented in the dB scale. The horizontal axes in the plots are rescaled with respect to the -3 dB beamwidths of the *sinc* functions given in (5). This means, the azimuth and range are normalized with respect to the $\sin(\phi_0/2)$ and $B_r/2$, respectively. However, in these *sinc* functions, $k_{c,r} = 1$ and $k_{r,max} - k_{r,min} = B_r$ due to the normalization in the derivation of IRF-USAR. These *sinc* functions are also plotted in the same figures to inspect the validity of IRF-NSAR for IR-SAR resulted by different SAR systems. The *sinc* functions and the functions $h(\rho, \varphi, 0.1, 10^\circ)$ are almost identical. This again confirms IRF-NSAR is a good approximation for IR-SAR resulted by NB SAR systems. This approximation may still be used for $h(\rho, \varphi, 0.35, 35^\circ)$. However, it does not hold for UWB SAR systems such as the SAR system 3 in Table 1. In this extreme case, $h(\rho, \varphi, 1.1, 110^\circ)$ are considered to be significantly different from the *sinc* functions. These observed results are similar to the analysis results given in Section 2 based on SAR simulated data.

A comparison between the IR-SAR extracted at the peak intensity of the single point target in a SAR image formed by simulated data and the IR-SAR approximately generated by the derived IRF-USAR in Section 3 is here given to evaluate the accuracy of the IRF-USAR. Only the extreme case where $B_r = 1.1$ and $\phi_0 = 110^\circ$ is considered. Hence, the extracted IR-SAR in azimuth and range directions are given by $h_3(x, 0)$ and $h_3(0, y)$, respectively while the approximate IR-SAR are given by $h(\rho, 0^\circ, 1.1, 110^\circ)$ and $h(\rho, 90^\circ, 1.1, 110^\circ)$. They are plotted in Fig. 3. In the plots, we also use the normalized terms. As shown, the functions $h(\rho, \varphi, 1.1, 110^\circ)$ and $h_3(x, y)$ are well matched, especially the function $h(\rho, 0^\circ, 1.1, 110^\circ)$ and $h_3(0, y)$. The observed differences in azimuth are caused by the assumption given in (8) used in the derivation.

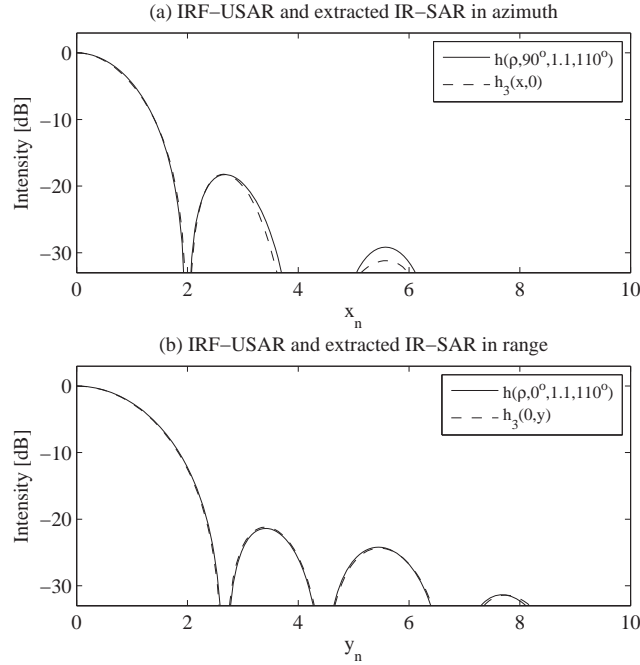


Figure 3: Plots of IR-SAR approximately generated by $h(\rho, \varphi, 1.1, 110^\circ)$ and extracted at the peak intensity of the single point target in the SAR image given in Fig. 1.e. The intensities of IR-SAR are normalized with respect to their peak intensity and in the dB scale. The horizontal axes in the plots are also rescaled with respect to the -3 dB beamwidths of the *sinc* functions given in (5) and also denoted by x_n and y_n , respectively. (a) in azimuth. (b) in range.

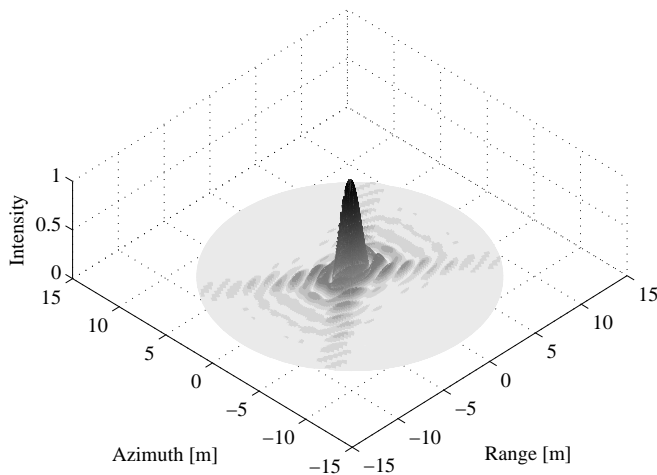


Figure 4: The three-dimensional (3-D) approximate SAR image of the point target is reconstructed from a set of the functions $h(\rho, \varphi, 1.1, 110^\circ)$. The intensity of the reconstructed point target is normalized with respect to its peak intensity and represented in the dimensionless scale.

In reality, we can compensate this by an azimuth weighting function. This extreme example confirms the accuracy of the derived IRF-USAR.

We can also use the derived IRF-USAR to reconstruct the SAR image of the point target. Fig. 4 shows a three-dimensional (3-D) image of a point target reconstructed using the derived IRF-SAR where the parameters of the SAR system 3 are used and the step between values of φ is 1° . The features of the reconstructed point target are similar to the point target imaged in Fig. 1.e. The contour plots from -30 dB to -3 dB with a 3 dB step of this point target are also given in Fig. 5 to provide a more illustrative comparison to the contours plotted in Fig. 1.e.

Similar to the applications of the IRF-NSAR in SAR image quality measurements and spatial resolution estimations for NB SAR systems, the derived IRF-USAR also facilitates such applications for UWB SAR systems. Based on the derived function in this paper, new SAR spatial resolution equations can be developed. The methods to determine mainlobe and sidelobe areas are also

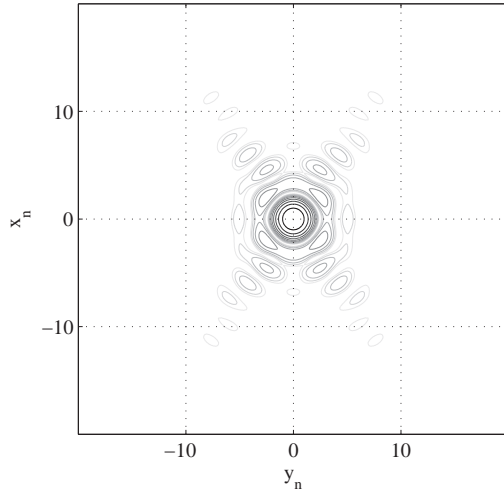


Figure 5: Contour plots from -30 dB to -3 dB with a 3 dB step of the the point target is reconstructed from a set of the functions $h(\rho, \varphi, 1.1, 110^\circ)$. The SAR image coordinates x_n and y_n denote normalized azimuth and range with respect to -3 dB widths.

supported by the new IRF-USAR. In general, UWB SAR image quality measurement procedures are simplified significantly compared to the ones given in [23]. In addition, the new IRF-USAR can be used to investigate orthogonal and non-orthogonal sidelobes resulted by UWB SAR systems and determine the limits of fractional bandwidth and integration angle to use IRF-NSAR.

5 Conclusion

The analysis on the point target in this paper shows that the currently used IRF-NSAR - the 2-D *sinc* function is mainly valid for NB SAR systems exploiting a small fractional signal bandwidth and a narrow antenna beamwidth. In reality, IRF-SAR depends strongly on these SAR system parameters. As a consequence, the applications of IRF-SAR such as image quality measurements and spatial resolution estimations are limited to NB SAR systems.

This analysis is used as a basis to derive a new IRF-USAR aiming at UWB SAR systems utilizing a large fractional signal bandwidth and a wide antenna beamwidth. However, the derived IRF-USAR is also valid for NB SAR systems. The derivation is based on the assumption that the 2-D FT of a SAR image is flat. The differences between the derived IRF-USAR and IRF-NSAR are addressed in the evaluations. The accuracy of the derived function is verified by a comparison between the IR-SAR extracted at the peak intensity of the single point target in a SAR image and the approximate IR-SAR generated by the derived IRF-USAR. The derived IRF-USAR can also be used to reconstruct a SAR image of a point target. The applications of the derived IRF-USAR such as SAR image quality measurements, spatial resolution estimations, orthogonal and non-orthogonal sidelobe investigation, and examining the validity of IRF-SAR are also suggested.

Appendix A

Impulse Response Function Derivation

With a natural choice of a flat 2-D FT of a SAR image of a point target (8), the integral (3) can be normalized and transformed to polar coordinates and represented by

$$h(\rho, \varphi) = \int \int \varrho e^{i\varrho\rho\cos(\phi-\varphi)} d\varrho d\phi \quad (\text{A-1})$$

by simply setting

$$\begin{aligned} k_x &= \varrho \cdot \sin\phi \\ k_y &= \varrho \cdot \cos\phi \end{aligned} \quad (\text{A-2})$$

and

$$\begin{aligned} x &= \rho \cdot \sin\varphi \\ r &= \rho \cdot \cos\varphi. \end{aligned} \quad (\text{A-3})$$

The complex exponential function in the integral (A-1) can be represented in terms of *bessel* functions as [24]

$$e^{i\varrho\rho\cos(\phi-\varphi)} = \sum_{n=-\infty}^{+\infty} i^n J_n(\varrho\rho) e^{in(\phi-\varphi)}. \quad (\text{A-4})$$

Hence, the integral (A-1) is rewritten as

$$h(\rho, \varphi) = \sum_{n=-\infty}^{+\infty} i^n \int \varrho J_n(\varrho\rho) d\varrho \int e^{in(\phi-\varphi)} d\phi. \quad (\text{A-5})$$

The solutions for the first and second integrals inside the summation (A-5) are given by

$$\int \varrho J_n(\varrho\rho) d\varrho = \frac{1}{\rho} \left\{ -\varrho J_{n-1}(\varrho\rho) + n \int J_{n-1}(\varrho\rho) d\varrho \right\} \quad (\text{A-6})$$

and

$$\int e^{in(\phi-\varphi)} d\phi = \frac{e^{in(\frac{\phi_0}{2}-\varphi)}}{in}, \quad (\text{A-7})$$

respectively. With the limits of ϕ defined in (8), the integral (A-7) results in

$$\int_{-\frac{\phi_0}{2}}^{+\frac{\phi_0}{2}} e^{in(\phi-\varphi)} d\phi = \frac{e^{in(\frac{\phi_0}{2}-\varphi)} - e^{-in(\frac{\phi_0}{2}+\varphi)}}{in}. \quad (\text{A-8})$$

The second term in (A-6) and (A-7) can be combined together and simplified to

$$\begin{aligned} & \frac{1}{\rho} \int \sum_{n=-\infty}^{+\infty} i^{n-1} J_{n-1}(\varrho\rho) e^{in(\frac{\phi_0}{2}-\varphi)} d\varrho \\ & - \frac{1}{\rho} \int \sum_{n=-\infty}^{+\infty} i^{n-1} J_{n-1}(\varrho\rho) e^{-in(\frac{\phi_0}{2}+\varphi)} d\varrho \\ & = \frac{e^{i(\frac{\phi_0}{2}-\varphi)}}{\rho} \int e^{i\varrho\rho\cos(\frac{\phi_0}{2}-\varphi)} d\varrho \\ & - \frac{e^{-i(\frac{\phi_0}{2}+\varphi)}}{\rho} \int e^{i\varrho\rho\cos(\frac{\phi_0}{2}+\varphi)} d\varrho \\ & = \frac{e^{i(\frac{\phi_0}{2}-\varphi)} e^{i\varrho\rho\cos(\frac{\phi_0}{2}-\varphi)}}{i\rho^2\cos(\frac{\phi_0}{2}-\varphi)} - \frac{e^{-i(\frac{\phi_0}{2}+\varphi)} e^{i\varrho\rho\cos(\frac{\phi_0}{2}+\varphi)}}{i\rho^2\cos(\frac{\phi_0}{2}+\varphi)}. \end{aligned} \quad (\text{A-9})$$

Substituting (A-6) and (A-7) to (A-5) and taking (A-10) into account, we

get

$$h(\rho, \varphi) = -\phi_0 \sum_{n=-\infty}^{+\infty} \frac{i^n \varrho J_{n-1}(\varrho\rho)}{\rho e^{in\varphi}} \text{sinc}\left(n \frac{\phi_0}{2}\right) \quad (\text{A-10})$$

$$+ \frac{e^{i\varrho\rho\cos(\frac{\phi_0}{2}-\varphi)+i(\frac{\phi_0}{2}-\varphi)}}{i\rho^2\cos(\frac{\phi_0}{2}-\varphi)} - \frac{e^{i\varrho\rho\cos(\frac{\phi_0}{2}+\varphi)-i(\frac{\phi_0}{2}+\varphi)}}{i\rho^2\cos(\frac{\phi_0}{2}+\varphi)}.$$

The final IRF-USAR can be obtained by inserting the integral limits of ϱ given in (8).

References

- [1] H. Hellsten, L. M. H. Ulander, A. Gustavsson, and B. Larsson, “Development of VHF CARABAS II SAR,” in *Proc. SPIE Radar Sensor Technology*, vol. 2747, Orlando, FL, Apr. 1996, pp. 48–60.
- [2] L. M. H. Ulander and H. Hellsten, “Airborne array aperture UWB UHF radar motivation and system considerations,” *IEEE Aerosp. Electron. Syst. Mag.*, vol. 15, pp. 35–45, May 2000.
- [3] D. R. Sheen, N. L. VandenBerg, S. J. Shackman, D. L. Wiseman, L. P. Elenbogen, and R. F. Rawson, “P-3 ultra-wideband SAR: description and examples,” *IEEE Aerosp. Electron. Syst. Mag.*, vol. 11, no. 11, pp. 25–30, 1996.
- [4] L. Carin, N. Geng, M. McClure, J. Sichina, and L. Nguyen, “Ultra-wideband synthetic-aperture radar for mine-field detection,” *IEE Antennas and Propagation Magazine*, vol. 41, no. 1, pp. 18–33, 1999.
- [5] A. R. Brenner and J. H. G. Ender, “Demonstration of advanced reconnaissance techniques with the airborne SAR/GMTI sensor PAMIR,” *IEE Proc.-Radar Sonar and Navigation*, vol. 153, no. 2, pp. 152–162, 2006.
- [6] R. Goodman, S. Tummala, and W. Carrara, “Issues in ultra-wideband, widebeam SAR image formation,” in *Proc. IEEE International Radar Conference*, Alexandria, VA, May 1995, pp. 479–485.
- [7] V. T. Vu, T. K. Sjögren, and M. I. Pettersson, “A comparison between fast factorized backprojection and frequency-domain algorithms in UWB

- low frequency SAR,” in *Proc. IEEE IGARSS’2008*, Boston, MA, Jul. 2008, pp. 1293–1296.
- [8] V. T. Vu, T. K. Sjögren, and M. I. Pettersson, “Ultrawideband chirp scaling algorithm,” *IEEE Geosci. Rem. Sens. Lett.*, vol. 7, no. 1, pp. 1–5, 2010.
- [9] V. T. Vu, T. K. Sjögren, M. I. Pettersson, L. Håkansson, A. Gustavsson, and L. M. H. Ulander, “RFI suppression in ultra-wideband SAR using adaptive line enhancer,” *IEEE Geosci. Rem. Sens. Lett.*, accepted for publication.
- [10] V. T. Vu, T. K. Sjögren, and M. I. Pettersson, “On apodization techniques for ultra-wideband SAR imaging,” in *Proc. EURAD 2009*, Rome, Italy, Sep. 2009, pp. 529–532.
- [11] M. A. and J. Marchand, “SAR image quality assessment,” *Asoc. Española de Teledetección Revista de Teledetección*, no. 2, pp. 12–18, 1993.
- [12] JPL SIR-C Team, DLRNE-HF X-SAR Team, and I-PAF X-SAR Team, “Data products and image quality specifications for the SIR-C/X-SAR mission,” JPL Document D-7193, Mar. 1990.
- [13] Envisat ASAR Cal/Val Team, “Quality measurements definition for ASAR level 1 products,” ESA, Tech. Rep. Issue 1, Mar. 2002.
- [14] W. M. Brown, “Synthetic aperture radar,” *IEEE Trans. Aerosp. Electron. Syst.*, vol. AES-3, pp. 217–229, 1967.
- [15] M. I. Skolnik, *Radar handbook*, 4th ed, New York: McGraw-Hill, 1990.
- [16] L. M. H. Ulander and H. Hellsten, “A new formula for SAR spatial resolution,” *AEÜ International Journal of Electronics and Communications*, vol. 50, no. 2, pp. 117–121, 1996.
- [17] L. E. Andersson, “On the determination of a function from spherical averages,” *SIAM Journal on Mathematical Analysis*, vol. 19, no. 1, pp. 214–232, 1988.
- [18] C. Cafforio, C. Prati, and F. Rocca, “SAR data focusing using seismic migration techniques,” *IEEE Trans. Aerosp. Electron. Syst.*, vol. 27, pp. 194–207, Mar. 1991.

- [19] R. K. Raney, “A new and fundamental Fourier transform pair,” in *Proc. IEEE IGARSS’1992*, Houston, TX, May 1992, pp. 106–107.
- [20] Y. L. Neo, F. H. Wong, and I. G.. Cumming, “A two-dimensional spectrum for bistatic SAR processing using series reversion,” *IEEE Geosci. Rem. Sens. Lett.*, vol. 4, no. 1, pp. 93–96, 2007.
- [21] X. Geng, H. Yan, and Y. Wang, “A two-dimensional spectrum model for general bistatic SAR,” *IEEE Trans. Geosci. Remote Sensing*, vol. 46, no. 8, pp. 2216–2223, 2008.
- [22] C. V. J. Jakowatz, D. E. Wahl, P. H. Eichel, D. C. Ghiglia, P. A. Thompson, *Spotlight-mode synthetic aperture radar: a signal processing approach*, Norwell, MA: Kluwer Academic Publishers, 1996, ch. 3, pp. 105–167.
- [23] V. T. Vu, T. K. Sjögren, M. I. Pettersson, and A. Gustavsson, “Definition on SAR image quality measurements for UWB SAR,” in *Proc. SPIE Image and Signal Processing for Remote Sensing XIV*, vol. 7109, Cardiff, UK, Sep. 2008, pp. 71091A (1–9).
- [24] L. Råde and B. Westergren, *Mathematics handbook for science and engineering*, 4th ed Lund, Sweden: Studentlitteratur, 1998, ch. 12, pp. 266–283.

Part I—B

Part I–A

On Synthetic Aperture Radar
Azimuth and Range Resolution Equations

Part I–B is published as:

V. T. Vu, T. K. Sjögren, and M. I. Pettersson, “On synthetic aperture radar azimuth and range resolution equations,” *IEEE Trans. Aerosp. Electron. Syst.*, accepted for publication.

On Synthetic Aperture Radar Azimuth and Range Resolution Equations

V. T. Vu, T. K. Sjögren, M. I. Pettersson and H. Hellsten

Abstract

This paper discusses spatial resolutions for ultrawideband-ultrawidebeam (UWB) synthetic aperture radar (SAR) in comparison to narrowband-narrowbeam (NB) SAR. The study shows that in the intensity interval from -6 dB to 0 dB, the behavior of the impulse response function in NB SAR imaging (IRF-NSAR) - *sinc* function - and the impulse response function in UWB SAR imaging (IRF-USAR) in azimuth and range are similar. This similarity is utilized in a derivation of new spatial resolution equations for UWB SAR based on -3 dB width or half power beamwidth (HPBW). Signal fractional bandwidth and associated integration angle are shown to affect the behavior of IRF-USAR. The effects to HPBW are described by the so-called HPBW narrowing/broadening factors.

Spatial resolutions are considered as the most significant parameter for image quality measurements since it describes the distance between two objects on the ground at which the objects appear distinct and separate in a synthetic aperture radar (SAR) image. Spatial resolution equations are used to estimate the azimuth and range resolutions which can be achieved by a specific SAR system. Such information is important from a SAR system designer's point of view. The azimuth resolution equation given in [1] and range resolution equation in [2] are supposed to aim at narrowband-narrowbeam (NB) side-looking SAR without a squint angle. These resolution equations do not consider the coupling between azimuth and range frequencies. They may therefore be invalid for ultrawideband-ultrawidebeam (UWB) SAR. Taking system frequency dependence into account, a new spatial resolution equation is introduced in [3]. However, this equation only provides the information of the area resolution, not azimuth and range resolutions which may be of interest.

The assessment of spatial azimuth and range resolutions is based on the -3 dB width of the impulse response function in SAR imaging (IRF-SAR) or the half power beamwidth (HBPW), i.e. the distances between the points with intensities of 3 dB below the peak intensity. For the availability of the impulse response function in NB SAR imaging (IRF-NSAR) - the *sinc* function, the derivation of the azimuth and range resolution equations for NB SAR seems to be simple. However, the complicated mathematical representation of the impulse response function in UWB SAR imaging (IRF-USAR) [4] creates difficulties for the derivation of the azimuth and range resolution equations for UWB SAR.

The objective of this paper is to discuss spatial resolution equations for UWB SAR in relation to the ones for NB SAR. This study is built on IRF-USAR which is previously published in [4]. On account of the similar behavior of the IRF-NSAR and IRF-USAR in the intensity interval from -6 dB to 0 dB, the spatial resolution equations for UWB SAR are built on the ones for NB SAR with the consideration of the coupling between azimuth and range frequencies through the so-called HPBW narrowing/broadening factors. The numerical results of these factors are also provided and summarized in graph.

The paper is organized as follows. In Section 2, the spatial resolution equations for NB SAR are derived based on IRF-NSAR. The relations to the commonly known SAR resolution equations are also examined. Section 3 investigates the similarity and difference between IRF-NSAR and IRF-USAR. New spatial resolution equations for UWB SAR are then introduced. Section 4 provides the conclusion.

1 Spatial Resolution Equations for NB SAR

As illustrated in Fig. 1, for NB SAR where both the integration angle and the fractional bandwidth are very small, the following approximations are valid for the two-dimensional (2-D) Fourier Transform (FT) of a NB SAR image of a point-like scatterer $H(k_x, k_y)$ marked by the light gray color

$$k_{y,min}\sin\frac{\phi_0}{2} \approx k_c\sin\frac{\phi_0}{2} \approx k_{y,max}\sin\frac{\phi_0}{2} \quad (1)$$

$$k_{y,max} - k_{y,min} \approx (k_{y,max} - k_{y,min})\cos\frac{\phi_0}{2} \quad (2)$$

where k_x and k_y are the azimuth and the range wavenumber. The subscripts c , max and min denote the terms of center, maximum and minimum, respec-

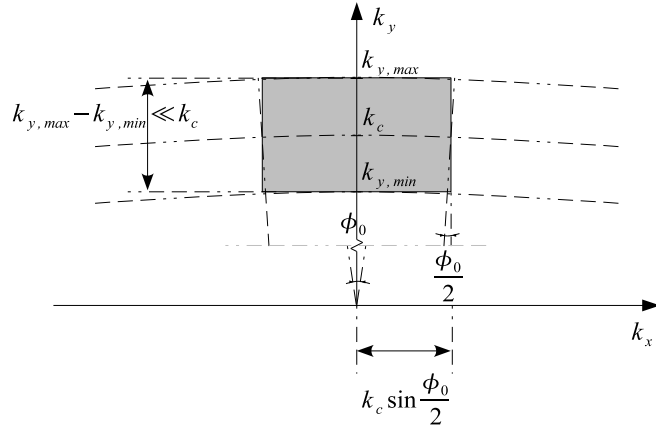


Figure 1: An example of 2-D FT of a NB SAR image of a point-like scatterer marked by the light gray color.

tively. The SAR image coordinates x and y indicate azimuth and range while ϕ_0 refers to the integration angle. The approximations in (1) and (2) are also interpreted as follows: a rectangular and flat approximation can be applied to the two-dimensional (2-D) Fourier Transform (FT) of a NB SAR image of a point-like scatterer. As shown in [4], IRF-NSAR $h(x, y)$ can be achieved from a 2-D Inverse Fourier Transform (IFT) of this approximation as

$$h(x, y) \approx \text{sinc} \left[k_c \sin \left(\frac{\phi_0}{2} \right) x \right] \text{sinc} \left(\frac{k_{y,\max} - k_{y,\min}}{2} y \right) \quad (3)$$

According to definitions of SAR image quality assessments proposed in [5]-[8], the spatial resolution, integrated sidelobe ratio (ISLR), and peak sidelobe ratio (PSLR) are based on a point-like scatterer approximation in a SAR image which can be a corner reflector deployed in measurement campaigns. The assessment of spatial azimuth and range resolutions is based on the -3 dB width or the half power beamwidth (HBPW) of the mainlobe, i.e. the distances between the points with intensities of 3 dB below the peak intensity. From the function (3), the spatial resolutions for NB SAR can be estimated

by solving the set of equations

$$\text{sinc}\left(k_c \frac{\Delta_x}{2} \sin \frac{\phi_0}{2}\right) = -3 \text{ dB} \quad (4)$$

$$\text{sinc}\left(\frac{k_{y,max} - k_{y,min}}{2} \frac{\Delta_y}{2}\right) = -3 \text{ dB} \quad (5)$$

The azimuth and range resolutions are then given by

$$\Delta_{N,x} = \frac{0.2211\lambda_c}{\sin\left(\frac{\phi_0}{2}\right)} \approx \frac{\lambda_c}{4\sin\left(\frac{\phi_0}{2}\right)} \quad (6)$$

$$\Delta_{N,y} = \frac{0.4422\lambda_c}{B_r} \approx \frac{c}{2B} \quad (7)$$

where λ_c is the center wavelength and B_r is the fractional bandwidth, defined by the ratio of the radar signal bandwidth B to the center frequency f_c . The approximated version of the azimuth resolution equation (6) is similar to the one given in [1] which is derived from the diffraction limit of the synthetic aperture. Similarly, the range resolution equation given in [2] has exactly the same expression as the approximated version of the range resolution equation (7). It should be mentioned here that the range resolution equation proposed in [2] is a general equation and used widely in the radar field. This equation is based on the minimum delay between two adjacent radar echoes so that they can be distinguished after pulse compression. For the cases where the integration angle is very small, i.e. $\sin(\phi_0/2) \approx \phi_0/2$, equation (6) can be further simplified as

$$\Delta_{N,x} \approx \frac{\lambda_c}{2\phi_0} \quad (8)$$

2 Spatial Resolution Equations for UWB SAR

Let us look at the 2-D FT of a UWB SAR image of a point-like scatterer $H(k_x, k_y)$, which is marked by the dark gray area given in Fig. 2. As illustrated, using NB approximation for $H(k_x, k_y)$ in this case is unreasonable. As a consequence, the approximations (1) and (2) should not be applied to UWB SAR systems. Equation (3) is not a good approximation for IRF-USAR. Also, the spatial resolution equations (6) and (7) or (8), which are derived from (3),

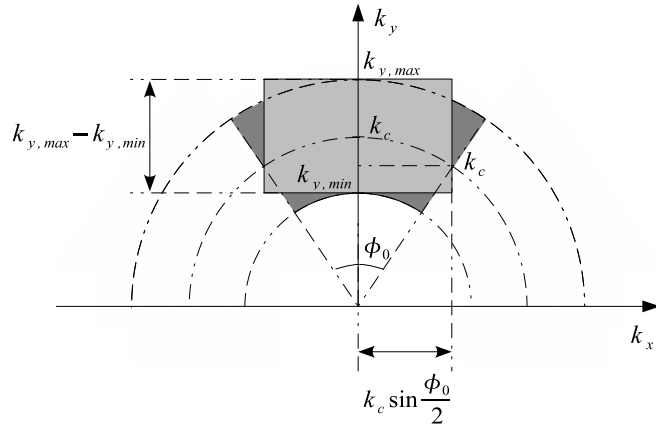


Figure 2: An example of 2-D FT of a UWB SAR image of a point-like scatterer $H(k_x, k_y)$ marked by the dark gray color. The light gray area associates with the NB approximation. Using NB approximation marked by the light gray color for $H(k_x, k_y)$ marked by dark gray color is unreasonable.

may result in large errors when used for UWB SAR. However, from a geometric point of view, (7) may be still valid for the cases of large fractional bandwidths and not very wide integration angles.

For UWB SAR systems with large fractional bandwidth and wide integration angle, the coupling between azimuth and range frequencies must be taken into account. This coupling can be represented by the relationship

$$\omega = \frac{c}{2} \sqrt{k_x^2 + k_y^2} = \frac{c}{2} \kappa \quad (9)$$

where ω is the radar signal frequency and κ represents a transformation of the wavenumbers k_x and k_y from a Cartesian coordinate system to a polar coordinate system. Considering the coupling between azimuth and range frequencies, the lower bound of the area resolution for UWB SAR is suggested in [3] but not the separate azimuth and range resolutions.

Table 1: SAR system parameters.

	System 1	System 2	System 3
Fractional bandwidth B_r	0.1	0.35	1.1
Associated integration angle ϕ_0	10°	35°	110°

2.1 IRF-USAR

As shown in the previous section, the spatial resolution equations for NB SAR were derived successfully from the IRF-NSAR. Similarly, the derivation of spatial resolution equations for UWB SAR can be based on an IRF-USAR. In other words, the possibility to develop spatial resolution equations for UWB SAR depends somewhat on the availability of an IRF-USAR. Using an assumption of a flat 2-D FT of a SAR image of a point-like scatterer and without the NB approximation, i.e. considering the coupling between azimuth and range frequencies, an IRF-USAR in polar coordinates (ρ, φ) is introduced in [4] as

$$\begin{aligned} h(\rho, \varphi, B_r, \phi_0) = & \\ & \frac{e^{-i\varphi}}{\rho} \left[\phi_0 \sum_{n=-\infty}^{+\infty} \frac{i^n h_{1,n-1}(\rho, B_r)}{e^{i(n-1)\varphi}} \text{sinc}\left(n \frac{\phi_0}{2}\right) \right] \\ & + \frac{e^{-i\varphi}}{\rho} h_2(\rho, \varphi, B_r, \phi_0) \end{aligned} \quad (10)$$

Equation (10), which is a function of fractional bandwidth B_r and integration angle ϕ_0 , has been proved in [4] to be valid for both NB and UWB SAR. This means that IRF-USAR with small fractional bandwidth and narrow integration angle is almost identical to IRF-NSAR with the corresponding values. This function is here used as a basis for derivation of spatial resolution equations for UWB SAR.

2.2 A comparison between IRF-NSAR and -USAR

In the derivation of (10), κ in (9) has been normalized with respect to the center wavenumber k_c . To compare between IRF-NSAR and -USAR, a similar

normalization can be applied to IRF-NSAR. The normalized form of (3) can be shown to be

$$h_n(x, y) \approx \text{sinc} \left[\sin \left(\frac{\phi_0}{2} \right) x \right] \text{sinc} \left(\frac{B_r}{2} y \right) \quad (11)$$

The comparison will focus only on the mainlobe area since the resolution information is extracted from the mainlobe of IRF-SAR. Since the azimuth and range resolutions are of interest, the 2-D plots of IRF-USAR are informative enough to be used in the comparison. For IRF-NSAR, the IRF-SAR in azimuth and range are given by $\text{sinc}[\sin(\phi_0/2)x]$ and $\text{sinc}[(B_r/2)y]$ while $h(\rho, 90^\circ, B_r, \phi_0)$ and $h(\rho, 0^\circ, B_r, \phi_0)$ result in the IRF-USAR in azimuth and range, respectively. By rescaling the azimuth and range axes with the inverse of $\sin(\phi_0/2)$ and $B_r/2$, the IRF-NSAR and -USAR can be plotted in the same figure. The rescaling also facilitates a comparison between IRF-NSAR and -USAR associated with different SAR systems. The fractional bandwidths and the integration angles associated with the antenna beamwidth (B_r, ϕ_0) used in the comparison are summarized in Table 1. Due to the rescaling of the azimuth and range axes, the plots of IRF-NSAR with these parameters would be identical. For this reason, only one of the pairs (B_r, ϕ_0) needs to be used to generate IRF-NSAR in this comparison.

Fig. 3 plots the mainlobes of IRF-USAR given by (10) and IRF-NSAR given by (11). In this plot, the intensity of an IRF-SAR is normalized with respect to its peak and then converted to the dB scale. As observed from Fig. 3, IRF-NSAR and -USAR are almost identical at small fractional bandwidth and narrow integration angle, e.g. $(B_r, \phi_0) = (0.1, 10^\circ)$. At large fractional bandwidths and wide integration angles, the behavior of IRF-USAR is much more complicated than the behavior of a *sinc* function. This can be explained by the azimuth-range frequency coupling which has been taken into account in IRF-USAR.

For comparison purposes, we can normalize the azimuth and range axes with respect to the HPBW of the IRF-SAR and then plot them in the same figure. The 2-D plots of the IRF-NSAR and -USAR with this normalization are given in Fig. 4 where the normalized azimuth and range are denoted by x_n and y_n . As shown, the behavior of IRF-NSAR and -USAR are very similar down to -6 dB. In other words, the mainlobe in the intensity interval from -6 dB to 0 dB may still be approximated as a *sinc* curve with the corresponding intensity interval. Hence, the function (3) may therefore be used to estimate the spatial resolutions in UWB SAR. However, the difference between IRF-NSAR and -USAR at the -3 dB beamwidth must be taken into account in the

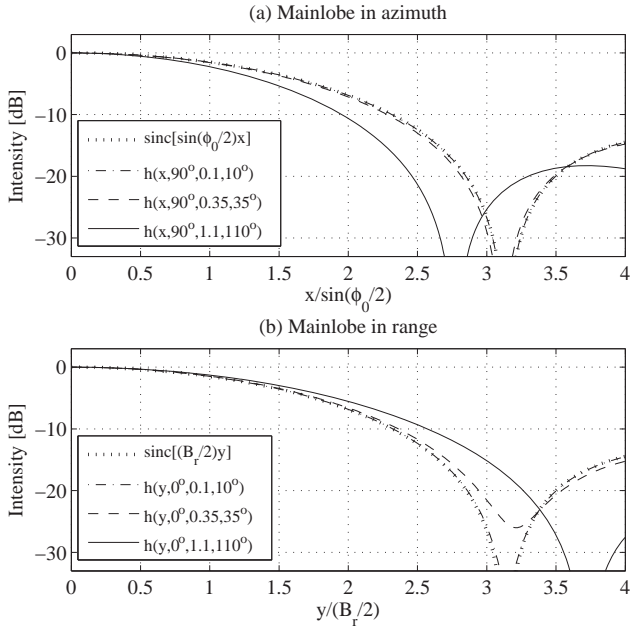


Figure 3: The plots of IRF-NSAR and -USAR with the different values of (B_r, ϕ_0) . The azimuth and range axes are rescaled with the inverse of $\sin(\phi_0/2)$ and $B_r/2$, respectively. (a) $\text{sinc}[\sin(\phi_0/2)x]$ and $h(x, 90^\circ, B_r, \phi_0)$, (b) $\text{sinc}[(B_r/2)y]$ and $h(y, 0^\circ, B_r, \phi_0)$.

estimations. This difference is described by a HPBW narrowing/broadening factor which will be introduced in the next section.

2.3 HPBW Narrowing/Broadening Factors

Let us consider a SAR system utilizing a fractional bandwidth B_r and an integration angle ϕ_0 . If the estimations of HPBW using IRF-NSAR are given by $\Delta_{N,x}(B_r, \phi_0)$ and $\Delta_{N,y}(B_r, \phi_0)$, and if $\Delta_{U,x}(B_r, \phi_0)$ and $\Delta_{U,y}(B_r, \phi_0)$ indicate the same estimations, however using IRF-USAR, then the HPBW narrowing/broadening factors in azimuth ϵ_x and in range ϵ_y will be defined

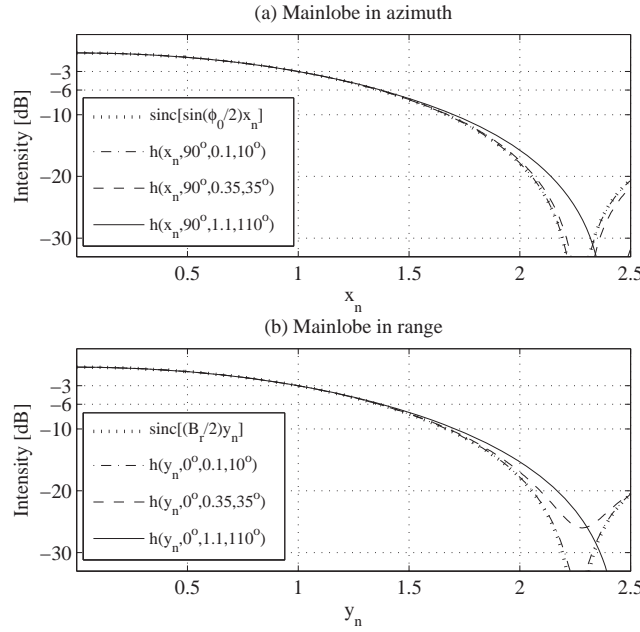


Figure 4: The mainlobes in azimuth and range with the different values of (B_r, ϕ_0) . The azimuth and range are normalized with respect to the -3 dB beamwidths of IRF-SAR. (a) $\text{sinc}[\sin(\phi_0/2)x_n]$ and $h(x_n, 90^\circ, B_r, \phi_0)$, (b) $\text{sinc}[(B_r/2)y_n]$ and $h(y_n, 0^\circ, B_r, \phi_0)$.

by

$$\epsilon_x = \frac{\Delta_{U,x}(B_r, \phi_0)}{\Delta_{N,x}(B_r, \phi_0)} \quad (12)$$

$$\epsilon_y = \frac{\Delta_{U,y}(B_r, \phi_0)}{\Delta_{N,y}(B_r, \phi_0)}, \quad (13)$$

respectively. To investigate HPBW narrowing/broadening factors associated with different SAR systems, IRF-NSAR (3) and -USAR (10) in the intensity interval $[-3, 0]$ dB are again plotted in Fig. 5 in which the same axial scaling used in Fig. 3, i.e. scaling the axes with the inverse of $\sin(\phi_0/2)$ and $B_r/2$, is used. IRF-NSAR is therefore independent of fractional bandwidth B_r and

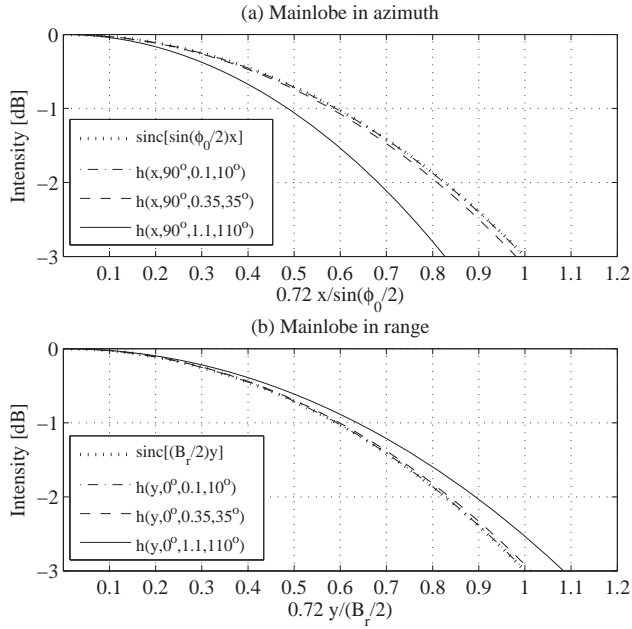


Figure 5: An investigation into the HPBW narrowing/broadening factors with the different values of (B_r, ϕ_0) . The azimuth and range are rescaled so that $\Delta_{N,x}/2 = 1$ and $\Delta_{N,y}/2 = 1$. (a) $\text{sinc}[\sin(\phi_0/2)x]$ and $h(x, 90^\circ, B_r, \phi_0)$, (b) $\text{sinc}[(B_r/2)y]$ and $h(y, 0^\circ, B_r, \phi_0)$.

integration angle ϕ_0 . In other words, $\Delta_{N,x}(B_r, \phi_0)$ and $\Delta_{N,y}(B_r, \phi_0)$ are a constant. The azimuth and range axes are then rescaled with a factor of 0.72 so that $\Delta_{N,x}/2 = 1$ and $\Delta_{N,y}/2 = 1$. In this case, the horizontal axes at intensity of -3 dB give, directly, the values of ϵ_x and ϵ_y with the different (B_r, ϕ_0) .

Some comments on the HPBW narrowing/broadening factors may be given as follows. The HPBW narrowing/broadening factors depend on the fractional bandwidth and integration angle of SAR systems. However, the deviation of these factors from one can be observed clearly when fractional bandwidth and integration angle are very large, e.g. $(B_r, \phi_0) = (1.1, 110^\circ)$. For SAR systems utilizing a small fractional bandwidth and a narrow integration angle, e.g.

$(B_r, \phi_0) = (0.1, 10^\circ)$, these HPBW narrowing/broadening factors are very close to one. Even at a larger fractional bandwidth and a wider integration angle, e.g. $(B_r, \phi_0) = (0.35, 35^\circ)$, we may still approximate ϵ_x and ϵ_y to one.

2.4 Azimuth and Range Resolution Equations

The azimuth and range resolution equations can be achieved by solving the set of equations

$$h\left(\frac{\Delta_x}{2}, 90^\circ, B_r, \phi_0\right) = -3 \text{ dB} \quad (14)$$

$$h\left(\frac{\Delta_y}{2}, 0^\circ, B_r, \phi_0\right) = -3 \text{ dB} \quad (15)$$

where $h(\rho, \varphi, B_r, \phi_0)$ is given by (10). This set of equations is not easy to solve analytically. The possibility to find the roots in a numerical way is also constrained due to the existence of two variables B_r and ϕ_0 in the equation. Thus, we propose to build the spatial resolution equations for UWB SAR upon (6) and (7). IRF-USAR is therefore approximated to IRF-NSAR in the intensity interval from -6 dB to 0 dB by the consideration of the HPBW narrowing/broadening factors. The azimuth and range resolution equations for UWB SAR are proposed as follows

$$\Delta_{U,x} = \epsilon_x \Delta_{N,x} = \epsilon_x \frac{0.2211 \lambda_c}{\sin\left(\frac{\phi_0}{2}\right)} \quad (16)$$

$$\Delta_{U,r} = \epsilon_y \Delta_{N,y} = \epsilon_y \frac{0.4422 c}{B} \quad (17)$$

The HPBW narrowing/broadening factors ϵ_x and ϵ_y in (16) and (17) represent the effects of fractional bandwidth and the integration angle to the azimuth and range resolutions or, in other words, the coupling between azimuth and range frequencies. For any SAR system, its fractional bandwidth, which is the ratio of the signal bandwidth to the center frequency, can only be in the interval $(0, 2]$. If the flight track of a SAR system is a straight line, the associated integration angle of this SAR system cannot be beyond the interval $[0^\circ, 180^\circ]$. These intervals are considered in the numerical calculations of ϵ_x and ϵ_y in (16) and (17). The values of these factors associated with different SAR systems are summarized in Fig. 6 and 7. As shown, for small signal fractional bandwidth and narrow integration angle, the factors ϵ_x and ϵ_y can be

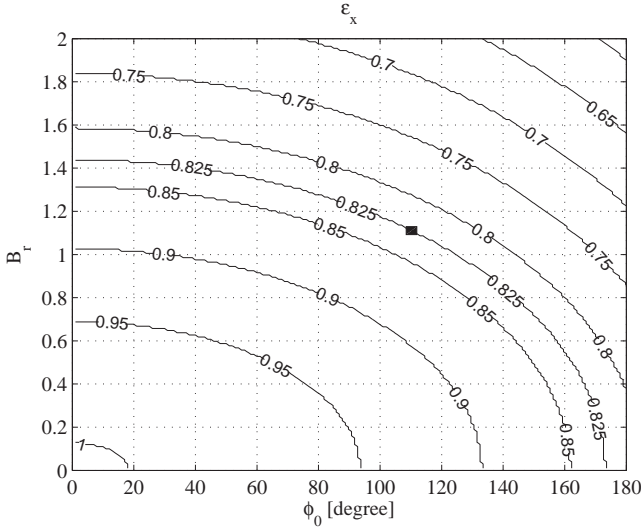


Figure 6: Numerical results of the HPBW narrowing/broadening factor in azimuth ϵ_x .

approximated to one. In this case, Equations (6) and (7) are identical to (16) and (17). The effect of the fractional bandwidth to the azimuth resolution is not as strong as the effect of the integration angle to the range resolution. A SAR system utilizing small fractional bandwidth can obtain very high range resolution by increasing the integration angle. For example, the range resolution of a SAR system with $B_r = 0.1$ can be enhanced two times when the system integration angle increases from $\phi_0 = 10^\circ$ to $\phi_0 = 70^\circ$.

The integration angle $\bar{\phi}_0$, where equal azimuth and range resolutions are reached, is estimated by equalizing (16) and (17) as

$$\bar{\phi}_0 = 2 \arcsin \left(\frac{\epsilon_x B_r}{\epsilon_r} \frac{1}{2} \right) \quad (18)$$

2.5 Validation

The validation of (16) and (17) is based on the parameters of the SAR system 3 given in Table 1. The SAR scene illuminated by this system is simulated only with one point-like scatterer. Using simulated data will avoid undesired effects

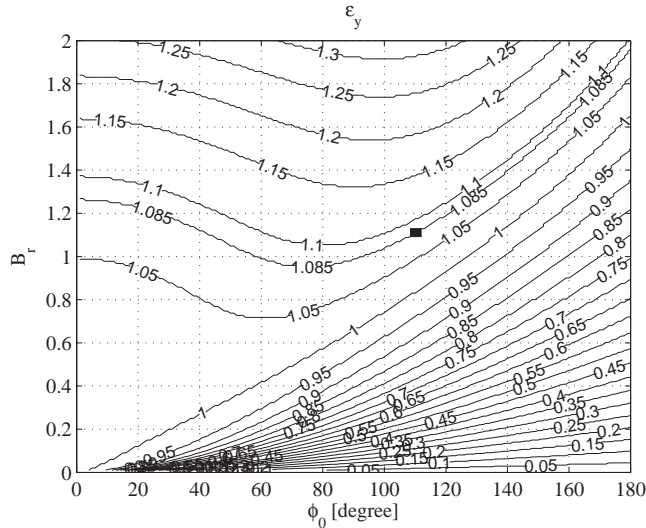


Figure 7: Numerical results of the HPBW narrowing/broadening factor in range ϵ_y .

such as impacts of antenna pattern, clutter backscattering, noise and local reflection which may affect the resolutions of the system. The azimuth and range resolutions achieved with this system in the simulation are $\Delta_{x,ref} \approx 1.36$ m and $\Delta_{y,ref} \approx 2.49$ m.

If the spatial resolutions are estimated by the approximated versions of (6) and (7), the results will be $\Delta_{N,x} \approx 1.75$ m and $\Delta_{N,y} \approx 2.61$ m. These values are quite different from $\Delta_{x,ref}$ and $\Delta_{y,ref}$. The Differential Resolution (DRES) introduced in [8] should be used to evaluate the accuracy of the resolution equations. In this case, DRES directly indicates the estimation errors. The errors are calculated as $\Delta_{dx} \approx 28.7\%$ and $\Delta_{dy} \approx 4.8\%$. The former can be seen to be significant.

Based on Fig. 6 and 7, we can determine the HPBW broadening/narrowing factors to be $\epsilon_{x,-3} \approx 0.825$ and $\epsilon_{y,-3} \approx 1.085$ (marked by black points on the figures). With these factors, the azimuth and range resolutions retrieved from (16) and (17) are $\Delta_{N,x} \approx 1.28$ m and $\Delta_{N,y} \approx 2.50$ m, respectively. The estimation errors are reduced to $\Delta_{dx} \approx 5.8\%$ and $\Delta_{dy} \approx 0.4\%$. These errors are quite small and originated from the flat spectrum assumption.

3 Conclusion

In this paper, we discuss the spatial resolution equations for NB and UWB SAR. The proposed spatial resolution equations can be seen as extended versions of the commonly known spatial resolution equations for NB SAR. The comparison between IRF-NSAR and -USAR and the HPBW narrowing/broadening factors, which must be considered in the equations for UWB SAR, can be seen to be the basis for this proposal. The HPBW narrowing/broadening factors are shown to be dependent on the fractional bandwidth and the integration angle of SAR systems. The numerical results of HPBW narrowing/broadening factors are also provided in this study.

References

- [1] W. M. Brown, “Synthetic aperture radar,” *IEEE Trans. Aerosp. Electron. Syst.*, vol. AES-3, pp. 217–229, 1967.
- [2] M. I. Skolnik, *Radar handbook*, 4th ed., New York: McGraw-Hill, 1990.
- [3] L. M. H. Ulander and H. Hellsten, “A new formula for SAR spatial resolution,” *AEÜ International Journal of Electronics and Communications*, vol. 50, no. 2, pp. 117–121, 1996.
- [4] V. T. Vu, T. K. Sjögren, M. I. Pettersson and H. Hellsten, “An impulse response function for evaluation of ultrawideband SAR imaging,” *IEEE Trans. Signal Processing*, vol. 58, issue. 7, pp. 3927–3932, 2010.
- [5] M. A. and J. Marchand, “SAR image quality assessment,” *Asoc. Española de Teledetección Revista de Teledetección*, no. 2, pp. 12–18, 1993.
- [6] JPL SIR-C Team, DLRNE-HF X-SAR Team, and I-PAF X-SAR Team, “Data products and image quality specifications for the SIR-C/X-SAR mission,” JPL Document D-7193, Mar. 1990.
- [7] Envisat ASAR Cal/Val Team, “Quality measurements definition for ASAR level 1 products,” ESA, Tech. Rep. Issue 1, Mar. 2002.
- [8] V. T. Vu, T. K. Sjögren, M. I. Pettersson, and A. Gustavsson, “Definition on SAR image quality measurements for UWB SAR,” in *Proc. SPIE Image and Signal Processing for Remote Sensing XIV*, vol. 7109, Cardiff, UK, Sep. 2008, pp. 71091A-1–71091A-9.

Part I—C

PART I-C

Definition on SAR Image Quality Measurements for UWB SAR

Part I–C is published as:

V. T. Vu, T. K. Sjögren, M. I. Pettersson, and A. Gustavsson, “Definition on SAR image quality measurements for UWB SAR,” in *Proc. SPIE Image and Signal Processing for Remote Sensing XIV*, vol. 7109, Cardiff, UK, Sep. 2008, pp. 71091A1–71091A9.

Definition on SAR Image Quality Measurements for UWB SAR

V. T. Vu, T. K. Sjögren, M. I. Pettersson, and A. Gustavsson

Abstract

Analyses in this study show that measurements under currently used definitions on SAR image quality measurement may be unsuitable for UWB SAR. The main objective of this paper is therefore to propose a definition based on the shape of a single point target in a SAR image which is more suitable for UWB SAR. We use both real and simulated data based on the airborne UWB low frequency SAR CARABAS-II in experiments. The time-domain algorithm Global Backprojection (GBP) is selected for the image formation in this study.

1 Introduction

Over the last decades, Synthetic Aperture Radar (SAR) has received a great interest as the number of applications in geosciences remote sensing, surveillance and recognizance increases. The ability to effectively collect data in severe conditions like rain, cloud and/or darkness is considered as the main advantages of SAR systems compared to other imaging sensors. Beside this, SAR systems enable high resolution images from long distances. A SAR image is a twodimensional mapping of the ground generated by coherent integration of many radar pulses backscattered by various targets in the illuminated scene. Ultra wideband (UWB) SAR which utilizes a large relative bandwidth (larger than 0.2 according to the FCC definition) signal and a wide beamwidth antenna (more than 90 degrees for CARABAS-II [1]) associated with very long integration times enables high resolution imaging and allows change detection in dense forested areas or under camouflage at low frequencies [2]. Such application is of interest to both military and civilian end-users.

SAR data obtained from measurement as well as the SAR processor performance are usually evaluated by SAR image quality measurements. The

measurements are usually based on known point targets. In general, corner reflectors which can be seen as point targets are used for system calibration in data collection campaigns. Basic terms of SAR image quality such as spatial resolution, Integrated Sidelobe Ratio (ISLR) and Peak Sidelobe Ratio (PSLR) are determined by the peak values and integrated energy of the mainlobe and sidelobes of the impulse response (IR) of a point target. Several SAR image quality definitions have been proposed. Some of them are briefly summarized in [3]. In general, spatial resolutions in azimuth Δ_x and range Δ_r are defined by -3 dB beamwidth of the mainlobe. We consider one example of quality measurement definition for SIR-C/X-SAR Mission [4]. According to [4], ISLR is defined by the ratio of energy of the sidelobe to energy of the mainlobe in which the energy is found within rectangle areas $20\Delta_x \times 20\Delta_r$ and $2\Delta_x \times 2\Delta_r$ respectively. Another example of quality measurement definition for Envisat ASAR products is given in [5] where the ratio of sidelobe energy to mainlobe energy also defines ISLR. However, the sidelobe area is here limited by a smaller rectangle $10\Delta_x \times 10\Delta_r$. PSLR or other measurement terms are based on parameters found within defined rectangular areas. Hence, the common idea in currently used SAR image quality definitions is to split the SAR image of a point target into mainlobe and sidelobe areas bounded by rectangles with different dimensions. Retrieved peak values and integrated energy within those areas are used to calculate SAR image quality parameters.

For UWB SAR, the delimitation of the mainlobe and sidelobe areas by rectangles may not be totally suitable. Moreover, the dimensions of these areas are even not equal to $2\Delta_x \times 2\Delta_r$, $10\Delta_x \times 10\Delta_r$ or $20\Delta_x \times 20\Delta_r$ in the case where the rectangles are assumed to be suitable for the delimitation. Measurements with currently used definitions on SAR image quality for UWB SAR may therefore be inexact, especially the measurements based on integrated energy. These measurements should also be performed at different integration angles since different azimuth focusing obtained at different integration angles results in different spatial resolution in azimuth and therefore different ISLR and PSLR.

In this paper, we propose a definition on image quality measurement for UWB SAR in which the shape and dimensions of the mainlobe and sidelobe areas are taken into account. In our evaluation we use both real and simulated data of CARABAS-II. A basic time-domain algorithm Global Backprojection (GBP) [6] which has been assigned to UWB SAR data processing is selected for this study.

The paper is organized as follows. Section 2 presents some main parameters of CARABAS-II system with impact on SAR image quality measure-

Table 1: CARABAS-II's main parameters of the data set analyzed.

Parameter	Value
The highest frequency channel processed	82 MHz
The lowest frequency channel processed	22 MHz
Platform speed v_{pl}	126 m/s
Full aperture length	33600 m
Number of aperture positions	35840
Flight altitude	4943 m
Minimum range to the aim point	11250 m

ments. We also briefly describe GBP algorithms in this section. Analyses on real shape of a point target in a SAR image and unsuitability of the currently used definitions on SAR image quality measurement for UWB SAR are given in section 3. In section 4, we propose a definition on image quality measurements for UWB SAR. Section 5 summarizes the contributions of the paper and provides the conclusions.

2 UWB SAR Systems and UWB SAR Data Processing

There have been UWB experimental systems developed such as CARABAS-II operating in the lower VHF-band from 20 to 90 MHz, LORA [7] in the VHF and UHF bands from 200 to 800 MHz, P-3 [8] with a bandwidth of 515 MHz in the 215-900 MHz VHF/UHF bands, BoomSAR [9] having a spectral response extending from 60 MHz to over 1 GHz and PAMIR SAR/MTI imaging radar with a very high simultaneous bandwidth of 1.82 GHz in X-band [10]. CARABAS-II is chosen to be the candidate for this study with a large number of publications available based on this sensor data. Early scientific publications concerning this system can be found in [11, 12]. CARABAS-II data is still used in many recent research works [13, 14]. In this section, we summarize main parameters of the CARABAS-II which is known as a UWB low frequency SAR system. Data which is used in this study is either collected

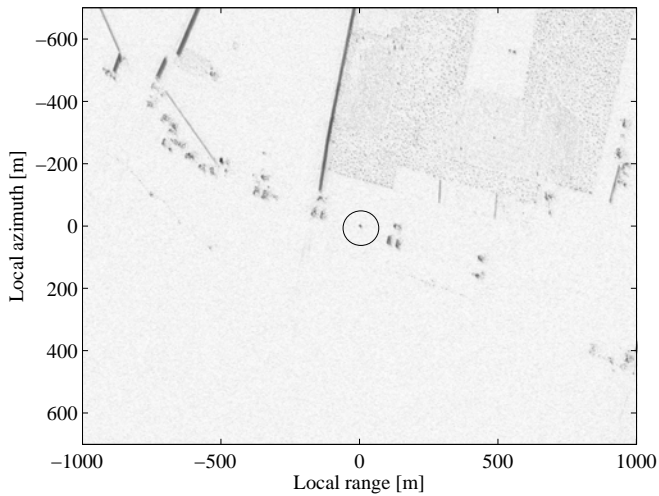


Figure 1: The SAR image is processed by GBP from the data collected in one of the CARABAS-II measurement campaigns. The corner reflector is located in the center of the image scene and marked by a black circle.

in one of the field campaigns with CARABAS-II or simulated according to its system parameters. Several time-domain algorithms have been proposed to process UWB SAR data. The main reasons to make them suitable for UWB SAR processing are manageable motion compensation, unlimited scene size, sufficient focus and local processing.

2.1 CARABAS-II

CARABAS-II has been developed by the Swedish Defence Research Agency (FOI). It is a VHF SAR system operating in the frequency range of 20-90 MHz. CARABAS-II is a wide beam system and therefore associated with very large integration angles due to the wide beamwidth dipole antennas of more than 90 degree. For these reasons, CARABAS-II can be seen as a UWB low frequency SAR system. The radar parameters used in one of the data collection campaigns are summarized in Table 1.

A part of the imaged scene used is shown in Figure 1. During this filed campaign, corner reflectors located at different areas with low scattering surrounding were deployed. One of them is located in the center of the local azimuth and range coordinates marked by a white circle. The reflector appears in the SAR image to be a single point target. We use this point target in analyses presented in the next section. With the given CARABAS-II parameters, the minimum integration angle evaluated is 5 degrees and at 65 degrees equal spatial resolutions in azimuth and range are obtained [15]. The maximum integration angle with respect to the aim point is about 110 degrees.

2.2 Global Backprojection (GBP)

The basic time-domain algorithm GBP allows imaging of scenes with high precision. In many contexts such as evaluation or comparison between time-domain algorithms, a SAR image processed by GBP can be considered to be a reference. However, the weakness of this algorithm is the high computational cost. A SAR image is considered as a linear transformation from the radar echo data. The backprojection process in GBP places a target at a position (x_0, r_0) in the SAR image and is simply interpreted by an integral

$$h(x_0, r_0) = \int_{-\frac{L}{2}}^{+\frac{L}{2}} g(x, R) dx \quad (1)$$

where x is the platform positions in the flight track, L is the aperture length and $g(x, R)$ is the range compressed data of a point target. In the case where the platform flies in a straight flight track along the x-axis, the range to the position (x_0, r_0) is represented by the hyperbolic function

$$R = \sqrt{(x - x_0)^2 - r_0^2} \quad (2)$$

3 Analysis on A Point Target

Analysis on a point target is the topic of this section. The analysis focuses on the delimitation of mainlobe and sidelobe areas and is based on both real and simulated CARABAS-II data. Using the real data, analysis may suffer from undesired effects such as impacts of antenna pattern, clutter backscattering,

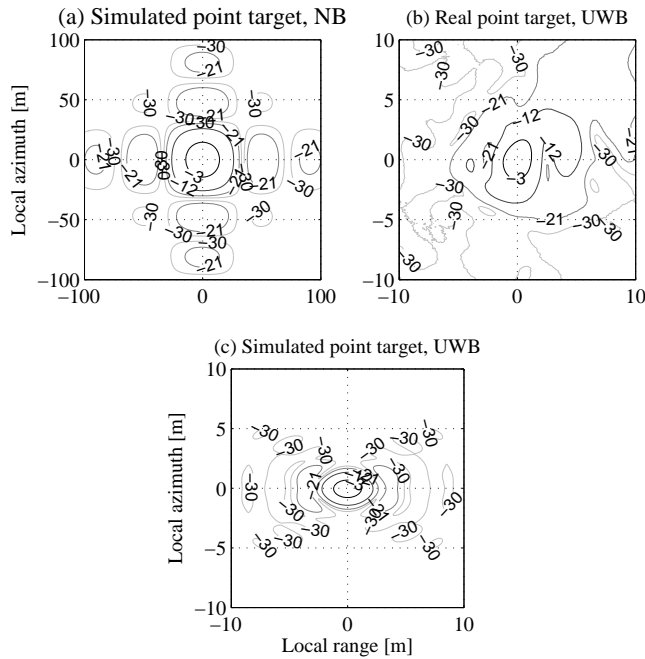


Figure 2: (a) Contour plots of a simulated point target in VHF narrowband SAR, (b) Contour plots of the corner reflector imaged by CARABAS-II and focused in Figure 1, (c) Contour plots of the simulated point target with the parameters given in Table 1. The UWB data is here processed with the full 110-degree integration angle.

noise and local reflection since the system may not be fully calibrated. Using the simulated data, we can avoid these undesired effects.

Delimitation of mainlobe and sidelobe areas are based on -3 dB beamwidth in azimuth and range according to currently used definitions on SAR image quality measurement.

For conventional SAR systems, rectangles can be approximately used for this delimitation as shown in Figure 2.a. With this assumption, azimuth and range vectors at the peak IR of a single point target can be approximated to be sinc functions. The ratios of First Null Beamwidth (FNBW) Θ_N to Half Power Beamwidth (HPBW) Θ_H in azimuth and range is used to estimate the dimensions of these rectangles as

$$\frac{\Theta_N}{\Theta_H} \approx \frac{\theta_N|_{\text{sinc}^2(\theta_N)=0}}{\theta_H|_{\text{sinc}^2(\theta_H)=0}} \approx 2 \quad (3)$$

Hence, the mainlobe area can be delimited by a $2\Delta_x \times 2\Delta_r$ rectangle. The area between the $2\Delta_x \times 2\Delta_r$ rectangle and either $10\Delta_x \times 10\Delta_r$ or $20\Delta_x \times 20\Delta_r$ rectangle is defined to represent the sidelobe area.

For UWB SAR systems, the narrowband approximations concerning the shape and/or the dimensions of the shape may not be suitable. Figure 2.b gives a closer look of the trihedral corner reflector in Figure 1 using contour plots at levels -3 dB, -12 dB, -21 dB and -30 dB. Due to the undesired effects, it may be difficult to delimit the mainlobe and sidelobe areas. However, neither the -3 dB contour nor lower levels of the point target can be considered as rectangles.

To get a better analysis, we propose to use simulated CARABAS-II data. No window or sidelobe control approach is used. Figure 2.c shows contour plots of a simulated point target. Using elliptic instead of rectangular areas to delimit the mainlobe and sidelobe areas seems more suitable for UWB SAR. If we use the approximation for the conventional SAR to estimate the dimensions of the elliptic areas, i.e. semimajor and semiminor axes, the mainlobe area can be delimited by an ellipse with semimajor and semiminor axes $(2\Delta_x, 2\Delta_r)$. The concentric elliptic area between a $(2\Delta_x, 2\Delta_r)$ ellipse and either a $(10\Delta_x, 10\Delta_r)$ or a $(20\Delta_x, 20\Delta_r)$ ellipse may be defined to represent sidelobe area. However, a further investigation of azimuth and range vectors at the peak IR of the single point target can result in more exact dimensions of these elliptic areas. This investigation is based on the simulated CARABAS-II data. Figure 3 shows azimuth vectors at the different integration angles 5, 65 and 110 degrees. If we call HPBW of azimuth vector spatial resolution

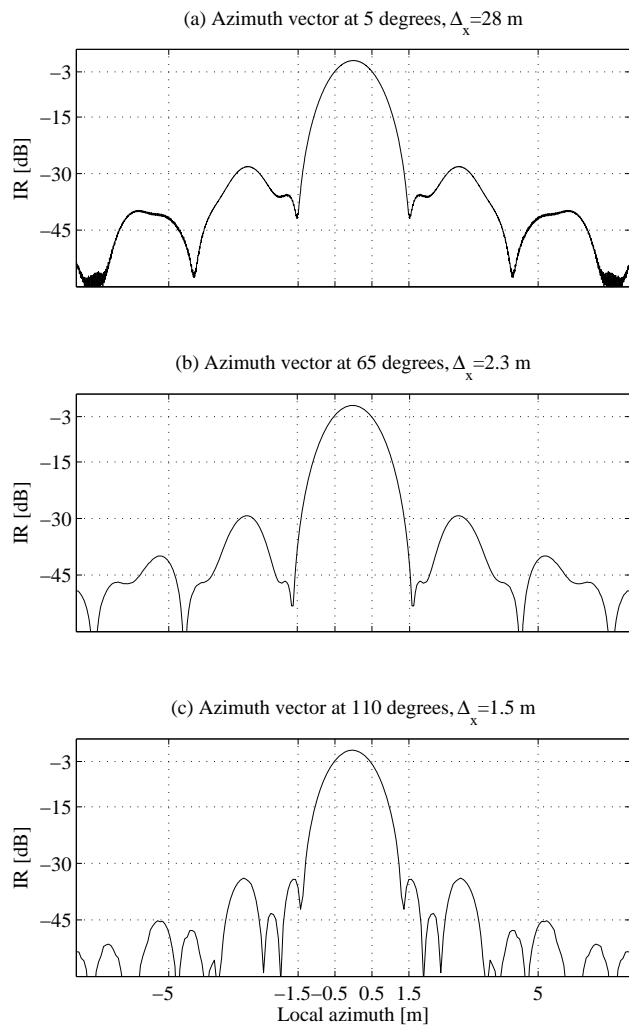


Figure 3: Azimuth vectors at different integration angles.

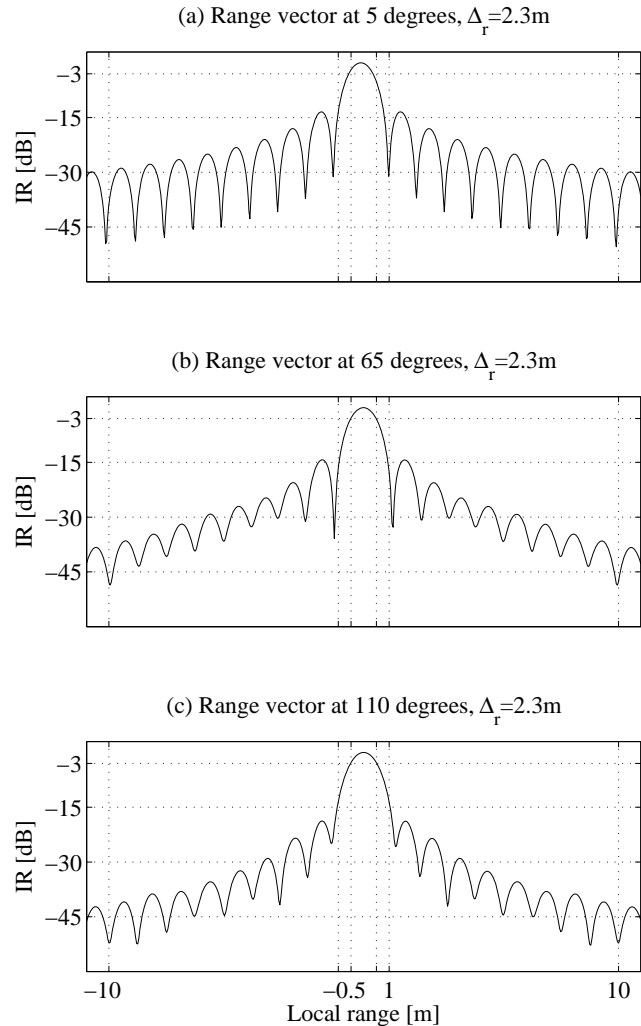


Figure 4: Range vectors at different integration angles.

in azimuth and -30 dB is the threshold for the SAR image considered to be null, investigations on these vectors show that the mainlobe broadening or FNBW is about three times this resolution at all integration angles. The peak intensity of the second sidelobes drops below the threshold -30 dB. Thus, the first sidelobes in azimuth are considered in the delimitation of the sidelobe area and lie in the interval from $\pm 3\Delta_x/2$ to $\pm 5\Delta_x$. The same investigation is carried out in range as shown in Figure 4. Although the mainlobe broadening is only about two times resolution in range, the sidelobes in the interval from $\pm \Delta_x$ to $\pm 10\Delta_x$ must be considered in the delimitation of the sidelobe areas. Hence, a factor of 2 is sufficient to represent the mainlobe broadening in the range direction but may not be large enough to represent the spread of the mainlobe in azimuth direction.

For UWB SAR, the mainlobe area and the sidelobe area may still be approximately delimited by a $(2\Delta_x, 2\Delta_r)$ ellipse and a $(2\Delta_x, 2\Delta_r) \& (10\Delta_x, 10\Delta_r)$ concentric elliptic area, respectively. For the UWB SAR system CARABAS-II, we propose, however a $(3\Delta_x, 2\Delta_r)$ ellipse and a $(3\Delta_x, 2\Delta_r) \& (5\Delta_x, 10\Delta_r)$ concentric elliptic area to define the mainlobe area marked in black area in Figure 5.b and the sidelobe area marked in gray area in Figure 5.b, respectively. If we make a reference to the SAR image of the simulated point target in Figure 5.a, we can see that such area delimitation is very realistic.

4 A Definition of SAR Image Quality Measurements

The analysis on a simulated point target in the previous section indicates that both mainlobe and sidelobe areas can be considered as elliptic and concentric elliptic areas, respectively. In general case, the dimensions of these areas can be approximated by $((2\Delta_x, 2\Delta_r)$ and $(10\Delta_x, 10\Delta_r)$. For CARABAS-II, $(3\Delta_x, 2\Delta_r)$ and $(5\Delta_x, 10\Delta_r)$ ellipses should be used to delimit the mainlobe and sidelobe areas. Based on these analyses, we propose a definition of SAR image quality measurements for UWB SAR in this section.

4.1 Resolution (RES) and Differential Resolution (DRES)

At the retrieved peak intensity of a single point target, we can extract two vectors in azimuth and range directions from a SAR image. The spatial resolution (RES) is the distance between two points at which the intensity is one

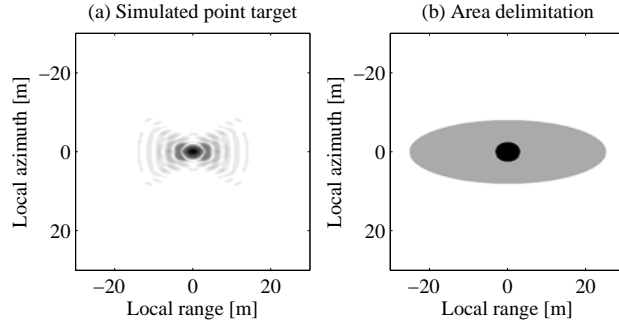


Figure 5: Mainlobe and sidelobe area delimitation (a) based on a simulated point target (b).

half of the peak intensity or in other words HPBW. Dependent on the considered vector, we can get spatial resolutions either in azimuth or in range. The spatial resolutions are recognized to be the most significant parameter for image quality measurements since it describes the distance between two objects on the ground at which the objects appear distinct and separate in a SAR image. Figure 6.a shows the measurement results on the spatial resolutions of the corner reflector and the simulated point target processed with GBP. As mentioned, UWB SAR systems are always associated with large integration angles to handle azimuth focusing. Hence, SAR image quality measurements should be performed different integration angles. A range of integration angles from 5 to 70 degrees has been used in this case.

In addition, we need to compare between the measured results in theory (simulated data) and in practice (real data). By looking at Figure 6.a, it is difficult to estimate the differences of measured results in both azimuth and range, especially at large integration angles. To simplify this work, we introduce the differential resolution (DRES) terms which are defined by

$$\begin{aligned}\Delta_{dx} &= \frac{\Delta_x - \Delta_{x,ref}}{\Delta_{x,ref}} \\ \Delta_{dr} &= \frac{\Delta_r - \Delta_{r,ref}}{\Delta_{r,ref}}\end{aligned}\quad (4)$$

where $\Delta_{x,ref}$ and $\Delta_{r,ref}$ are measured results in simulated data and can be considered as the reference. Figure 6.b shows the obtained results on differential resolution. Based on these results, we can easily evaluate the performance

of CARABAS-II in terms of SAR image quality. For example, the resolution in range is about 20% lower than theory predicts and it is more difficult to reach the theoretical resolution in azimuth at large integration angles.

4.2 Integrated Sidelobe Ratio (ISLR) and Peak Sidelobe Ratio (PSLR)

Based on the delimitation of the mainlobe and sidelobe areas given in Section 3, we can estimate energy within mainlobe and sidelobe areas. The ISLR which measures energy spilling over to sidelobes from the mainlobe is the ratio in the general case as a ratio expressed in logarithmic terms by

$$\text{ISLR} |_{\text{dB}} = 10 \log \left| \frac{\iint_{(10\Delta_x, 10\Delta_r)} |I| dA - \iint_{(2\Delta_x, 2\Delta_r)} |I| dA}{\iint_{(2\Delta_x, 2\Delta_r)} |I| dA} \right| - 10 \log \left| \iint_{(2\Delta_x, 2\Delta_r)} |I| dA \right| \quad (5)$$

and for UWB systems such as CARABAS-II

$$\text{ISLR} |_{\text{dB}} = 10 \log \left| \frac{\iint_{(5\Delta_x, 10\Delta_r)} |I| dA - \iint_{(3\Delta_x, 2\Delta_r)} |I| dA}{\iint_{(3\Delta_x, 2\Delta_r)} |I| dA} \right| - 10 \log \left| \iint_{(3\Delta_x, 2\Delta_r)} |I| dA \right| \quad (6)$$

PSLR which measures the ability to image a weak reflective target affected by a strong reflective target nearby is defined by the ratio of the extracted peak intensity within the sidelobe area to the peak intensity in the mainlobe area according to

$$\text{PSLR} |_{\text{dB}} = 10 \log |I_{SL}| - 10 \log |I_{ML}| \quad (7)$$

Figure 7 shows measurement results of ISLR and PSLR on the simulated CARABAS-II data using both the proposed and currently used definitions. The difference between ISLR measured by equation (5) for general case and equation (6) for CARABAS-II is more than 1dB. Although the difference is not large, investigations on the mainlobe broadening may be required before performing measurements for UWB SAR. The difference between ISLR measured by equation (6) and the currently used (rectangles $2\Delta_x \times 2\Delta_r$ and $10\Delta_x \times 10\Delta_r$) definitions is less 1dB. The difference may be much larger in reality when undesired effects are added. However, the ISLR measured by the

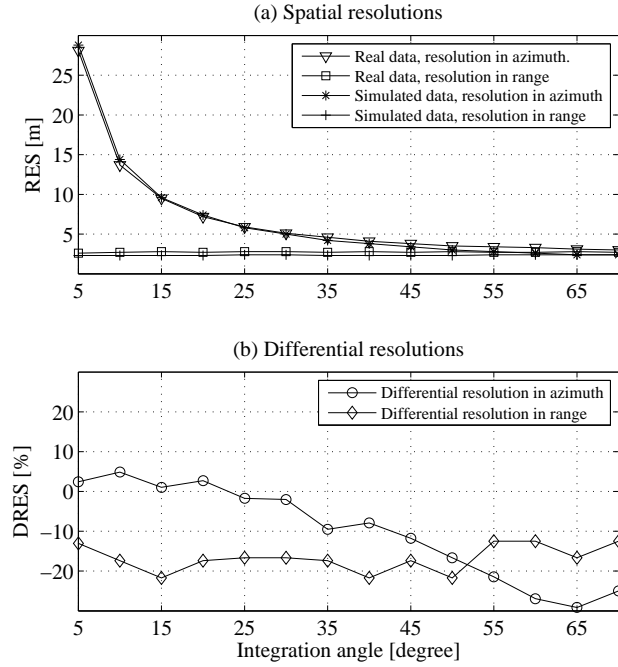


Figure 6: Resolution measurements.

different definitions has similar behavior and is proportional to the increase of integration angle. The measured results on PSLR show that PSLR reduces slightly proportional to the increase of the integration angle. Found PSLR values usually correspond to the first sidelobe in the extracted range vectors. Thus, there is not much difference between results measured by the proposed and currently used definitions.

5 Conclusion

In this paper, we point out that the currently used definition on SAR image quality measurements is unsuitable to measure UWB SAR performance. Based on analyses of a point target, we propose the elliptic instead of rectangular delimitation of the mainlobe and sidelobe areas, i.e. mainlobe and

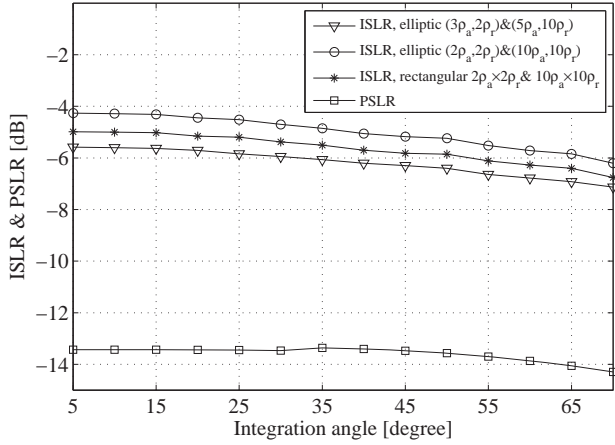


Figure 7: ISLR and PSLR measurements.

sidelobe areas are bounded by an ellipse and a concentric ellipse, respectively. Dimensions of these elliptic areas can be either approximately estimated by sinc functions as in the narrowband cases or based on investigations of the mainlobe broadening. The latter show that a factor of 2 is sufficient to represent the spread of the mainlobe in the range direction but may not be large enough to represent the spread of the mainlobe in the azimuth direction. A factor of 3 is considered for the UWB systems CARABAS-II to cover the mainlobe broadening in azimuth direction. With this delimitation, we give a definition on image quality measurements for UWB SAR in general and CARABAS-II in particular. The definition concerns basic terms such as resolution, ISLR and PSLR. Beside the resolution factor, we also introduce a differential resolution term which is very convenient for comparison purposes. SAR image quality measurements on the simulated data illustrate the proposed definition.

References

- [1] A. Gustavsson, L. M. H. Ulander, B. H. Flood, P.-O. Frölind, H. Hellsten, T. Jonsson, B. Larsson, and G. Stenstrom, “Development and op-

- eration of an airborne VHF SAR system—lessons learned,” in *Proc. IEEE IGARSS’98*, vol. 1, Seattle, WA, Jul. 1998, pp. 458–462.
- [2] L. M. H. Ulander, M. Lundberg, W. Pierson, and A. Gustavsson, “Change detection for low-frequency SAR ground surveillance,” *IEE Proc.-Radar Sonar and Navigation*, vol. 152, no. 6, pp. 413–420, 2005.
 - [3] A. Martinez and J. L. Marchand, “SAR image quality assessment,” *Asoc. Española de Teledetección Revista de Teledetección*, no. 2, pp. 12–18, 1993.
 - [4] JPL SIR-C Team, DLRNE-HF X-SAR Team, and I-PAF X-SAR Team, “Data products and image quality specifications for the SIR-C/X-SAR mission,” JPL Document D-7193, Mar. 1990.
 - [5] Envisat ASAR Cal/Val Team, “Quality measurements definition for ASAR level 1 products,” ESA, Tech. Rep. Issue 1, Mar. 2002.
 - [6] L. E. Andersson, “On the determination of a function from spherical averages,” *SIAM Journal on Mathematical Analysis*, vol. 19, no. 1, pp. 214–232, 1988.
 - [7] L. M. H. Ulander and H. Hellsten, “Airborne array aperture UWB UHF radar motivation and system considerations,” *IEEE Aerosp. Electron. Syst. Mag.*, vol. 15, pp. 35–45, May 2000.
 - [8] D. R. Sheen, C. M. Strawitch, and T. B. Lewis, “UHF wideband SAR design and preliminary results,” in *Proc. IEEE IGARSS’94*, vol. 1, Pasadena, CA, Aug. 1994, pp. 289–291.
 - [9] L. Happ, K. A. Kappra, M. A. Ressler, J. P. Sichina, K. Sturgess, and F. Le, “Low-frequency ultra-wideband synthetic aperture radar 1995 Boom-SAR tests,” in *Proc. IEEE National Radar Conference*, Ann Arbor, MI, May. 1996, pp. 54–59.
 - [10] H. Wilden, J. Ender, “System design of the FGAN experimental SAR/MTI system PAMIR,” in *Proc. EuMC WS5*, Munich, Germany, Oct. 2003, pp. 5–12.
 - [11] H. Israelsson, L. M. H. Ulander, J. L. H. Askne, J. E. S. Fransson, P.-O. Frörlind, A. Gustavsson, and H. Hellsten, “Retrieval of forest stem volume using VHF SAR,” *IEEE Trans. Geosci. Remote Sensing*, vol. 35, no. 1, pp. 36–40, 1997.

- [12] L. M. H. Ulander and P.-O. Frölind, “Ultra-wideband SAR interferometry,” *IEEE Trans. Geosci. Remote Sensing*, vol. 36, no. 5, pp. 1540–1550, 1998.
- [13] V. T. Vu, T. K. Sjögren, M. I. Pettersson, H.-J. Zepernick, and A. Gustavsson, “Experimental results on moving targets detection by focusing in UWB low frequency SAR,” in *Proc. IET RADAR’2007*, Edinburgh, UK, Oct. 2007, pp. 562–566.
- [14] V. T. Vu, T. K. Sjögren, and M. I. Pettersson, “Moving target detection by focusing for frequency domain algorithms in UWB low frequency SAR,” in *Proc. IEEE IGARSS’2008*, Boston, MA, Jul. 2008, pp. 161–164.
- [15] L. M. H. Ulander and H. Hellsten, “A new formula for SAR spatial resolution,” *AEÜ International Journal of Electronics and Communications*, vol. 50, no. 2, pp. 117–121, 1996.

Part II—A

Part II–A

RFI Suppression in Ultrawideband SAR
Using Adaptive Line Enhancer

Part II–A is published as:

V. T. Vu, T. K. Sjögren, M. I. Pettersson, L. Håkansson, A. Gustavsson, and L. M. H. Ulander “RFI suppression in ultrawideband SAR using adaptive line enhancer,” *IEEE Geosci. Rem. Sens. Lett.*, vol. 7, no. 4, pp. 282–286, 2010.

RFI Suppression in Ultrawideband SAR Using Adaptive Line Enhancer

V. T. Vu, T. K. Sjögren, M. I. Pettersson, L. Håkansson,
A. Gustavsson and L. M. H. Ulander

Abstract

In this paper, we propose an approach to suppress Radio Frequency Interference (RFI) in ultrawideband (UWB) low frequency Synthetic Aperture Radar (SAR). According to the proposal, RFI is suppressed by using an Adaptive Line Enhancer (ALE) controlled by the Normalized Least Mean Square (NLMS) algorithm. The approach is tested successfully on real UWB low frequency SAR data. In order to keep the computational burden down, possible ways to integrate the RFI suppression approach into SAR imaging algorithms are also suggested.

1 Introduction

Practical issues in ultrawideband (UWB) Synthetic Aperture Radar (SAR) data processing have been described in [1]. Among these, Radio Frequency Interference (RFI) suppression has not attracted much attention in recent publications. This may be explained by the dependence of RFI on the operating frequency of the SAR systems. An early approach, which adaptively filters RFI in a simulated baseband SAR signal (40 MHz), is introduced in [2]. Another approach in the frequency-domain with amplitude normalization aiming at low-frequency UWB SAR systems is presented in [3]. The limitations of these approaches can mainly be found in the Least Mean Square (LMS) adaptive filter, which may be sensitive to non-stationary SAR scenes. In addition, the results of RFI suppression obtained with these approaches are demonstrated mainly in relation to the raw radar signal. The evaluation of their performance may be insufficient. For example, the efficiency of RFI suppression in the approaches presented in [2] and [3] is not clearly defined or it is not compared to other methods. The computational burden demanded

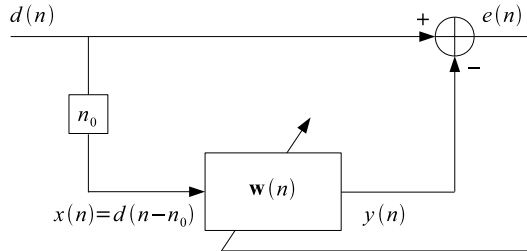


Figure 1: Adaptive Line Enhancer (ALE) structure.

by these approaches is not discussed and no solution to reduce the computational complexity is suggested. There are also other approaches such as notch filtering during the image correlation process reserved for JERS-1 SAR [4] and the filtering approach for synthesized SAR images proposed in [5] and tested with E-SAR L-band data.

In this paper, we propose to use an Adaptive Line Enhancer (ALE) [6] controlled by the Normalized Least Mean Square (NLMS) algorithm to eliminate RFI. To evaluate the performance of the proposed method, data collected by an airborne UWB low frequency SAR system, CARABAS-II [7], have been used. The collected data comprise a point target - a corner reflector - deployed in the SAR scene. Moreover, the proposed RFI suppression approach is compared to the Linear RFI Filtering (LRF) technique [8] which is currently used in CARABAS-II data processing. Also, the computational cost of the ALE in this application has been addressed and a strategy for integrating it into the SAR imaging algorithms is recommended.

2 RFI Suppression by ALE

ALE is essentially Adaptive Noise Cancellation (ANC) without a separate reference signal. In ALE, the input signal is delayed to generate the reference signal. Figure 1 shows the ALE structure. If the radar echo is used as input to the ALE, the input $d(n)$ is defined by

$$d(n) = s(n) + \nu(n) + \rho(n), \quad (1)$$

where $s(n)$ is the reflected UWB radar signal, i.e. the chirp signal, $\nu(n)$ is the thermal noise signal and the RFI signal is $\rho(n)$. Furthermore, $x(n)$ is the

reference signal to the adaptive FIR filter $\mathbf{w}(n)$ and this is a delayed version of the input signal, i.e. $x(n) = d(n - n_0)$ where n_0 is the delay in sample. If the adaptive FIR filter has the order L , its coefficient vector $\mathbf{w}(n)$ and reference signal vector $\mathbf{x}(n)$ are given by

$$\mathbf{w}(n) = [w_0(n) \ w_1(n) \cdots w_{L-1}(n)]^T \quad (2)$$

and

$$\mathbf{x}(n) = [x(n) \ x(n-1) \cdots x(n-L+1)]^T, \quad (3)$$

respectively. Assuming that the input signal $d(n)$ is a weakly stationary real stochastic process, the cross-correlation between the input signal $d(n)$ and the reference signal $x(n)$ is given by

$$r_{dx}(k) = E[d(n)x(n-k)], k \in Z \quad (4)$$

Using the fact that the RFI signal is a narrowband signal and selecting the minimum delay n_0 that de-correlates the UWB radar and the thermal noise signals in the radar echo $d(n)$ and in the reference signal $x(n)$, the cross-correlation can be shown to be

$$\begin{aligned} r_{dx}(k) &= E[d(n)x(n-k)] \\ &= E[\rho(n)\rho(n-n_0-k)], k \geq 0. \end{aligned} \quad (5)$$

If it is assumed that the ALE FIR filter has converged to its Wiener filter coefficients, the output signal of the filter will thus be an estimate of the RFI signal

$$\rho(n) \approx y(n) = \mathbf{w}^T(n)\mathbf{x}(n). \quad (6)$$

Hence, the estimation error signal $e(n)$ will be an estimate of the UWB radar signal plus the thermal noise signal

$$e(n) = d(n) - y(n) \approx s(n) + \nu(n). \quad (7)$$

An airborne UWB SAR system is usually associated with a long and nonlinear sensor trajectory. The high energy radiating from RFI sources can appear anywhere and anytime in a illuminated ground scene. To handle the non-stationary ground scene, and thus a non-stationary reference signal to the adaptive filter, the NLMS algorithm is proposed to adjust the adaptive filter coefficients

$$\mathbf{w}(n+1) = \mathbf{w}(n) + \frac{\beta}{\mathbf{x}^T(n)\mathbf{x}(n) + \epsilon}\mathbf{x}^*(n)e(n), \quad (8)$$

where $0 < \beta < 2$ and ϵ is a small positive real number. The starting set of the filter coefficient vector $\mathbf{w}(n)$ can be selected as

$$\mathbf{w}(0) = [0 \ 0 \ \cdots \ 0]^T. \quad (9)$$

3 Experimental Results and Evaluation

In this section, some experimental results are presented to illustrate and evaluate the approach proposed in the previous section. The CARABAS-II [7] data is used in the experiments. CARABAS-II operates in the lower VHF-band from 20 to 90 MHz. This means that the radar system operates in an environment with a high thermal noise level and frequency bands with very strong broadcasters. The influence of these broadcasters is considered to be extremely significant since their radiated power is much higher than the reflected power of CARABAS-II.

Fig. 2(a) shows the imaged ground scene of the island Visingsö located in southern Sweden using data collected by the CARABAS-II system. As a part of imaging the ground scene, a corner reflector was deployed in the center of the ground scene. This corner reflector should appear as a point target in the area marked by the white circle in Fig. 2(a). However, the point target is totally hidden by RFI and only very strong scatterers on the island can be seen in the SAR image. The influence of RFI on the SAR images has been shown to be affected by the integration angle [9]. However, this will not be considered in this paper and the complete aperture, i.e. the widest possible integration angle, is used.

The original range-compressed radar echo containing the RFI signal and the magnitude of its Discrete Fourier Transform (DFT) are plotted in Fig. 3(a) and 3(b), respectively. The number of range samples is $N = 16384$. RFI, e.g. at the frequency of about 27 MHz, and others in the range from 48 MHz to 68 MHz, can be observed in Fig. 3 (b). Such RFI may be caused by the Citizens' band (26.965 - 27.405 MHz) and television channels 2-6 (54-88 MHz). Fig. 3 (b) also shows the extremely high magnitude of the RFI component (up to 100 dB) compared to the magnitude of the flat UWB radar spectrum (only about 60 dB). This also means that the RFI signal dominates in the radar echo. A more illustrative analysis can be found in [9], where the radar echo is simulated according to CARABAS-II parameters.

The RFI suppression scheme is given in Fig. 4. According to this scheme, the original range-compressed radar echo containing the RFI signal is first

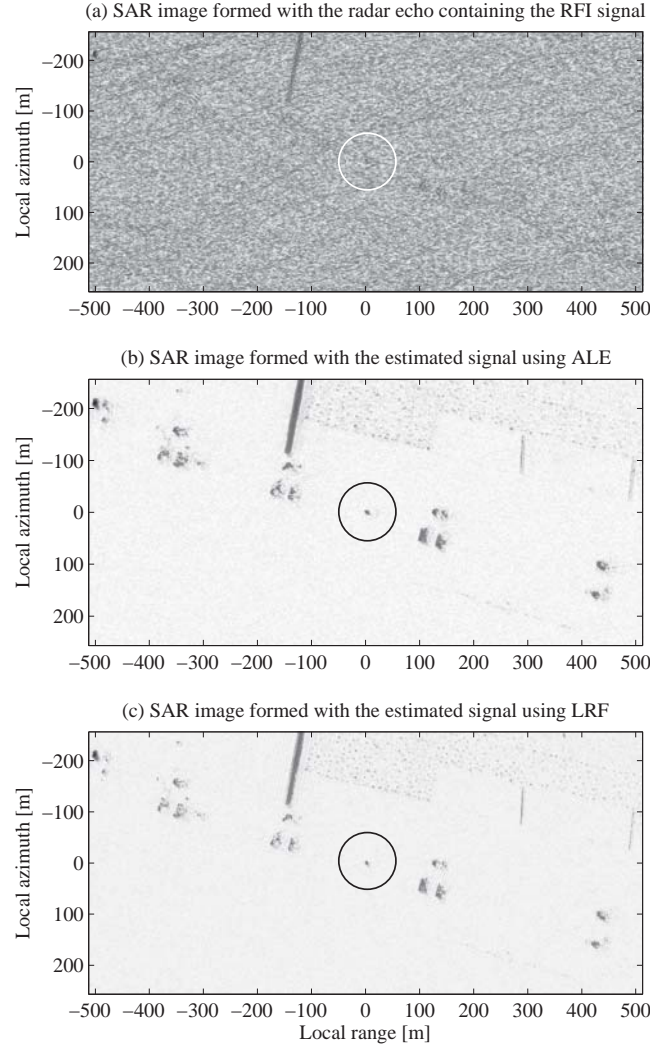


Figure 2: SAR images of the illuminated ground scene. The white/black circles in the SAR images mark the position of the corner reflector which has been deployed in the field campaign. (a) SAR image formed with the original radar echo containing the RFI signal. (b) SAR image formed with the estimated signal using ALE. (c) SAR image formed with the estimated signal using LRF.

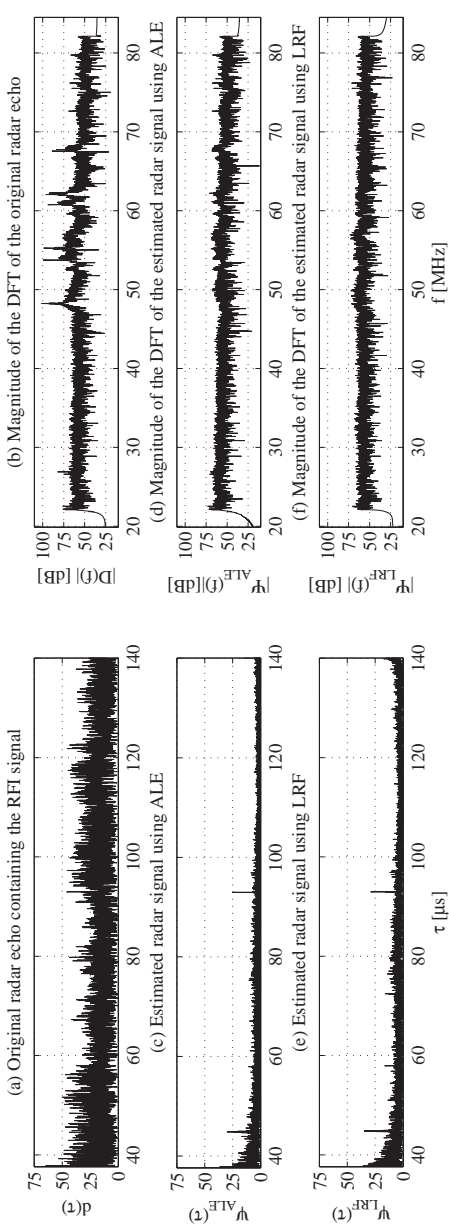


Figure 3: The range-compressed radar echo containing the RFI signal, the estimated signal using ALE, the estimated signal using LRF in the time-domain and the magnitudes of their DFT in the frequency-domain, i.e. their periodograms. The unit of the radar echo and the estimated signals are given in the dimensionless scale, and the magnitudes of their DFT in the dB scale. In the plots, the time axis τ instead of the sample axis n is used. (a) describes the radar echo containing the RFI signal and (b) the magnitude of its DFT. (c) describes the estimated signal using ALE and (d) the magnitude of its DFT. (e) describes the estimated signal using LRF and (f) the magnitude of its DFT.

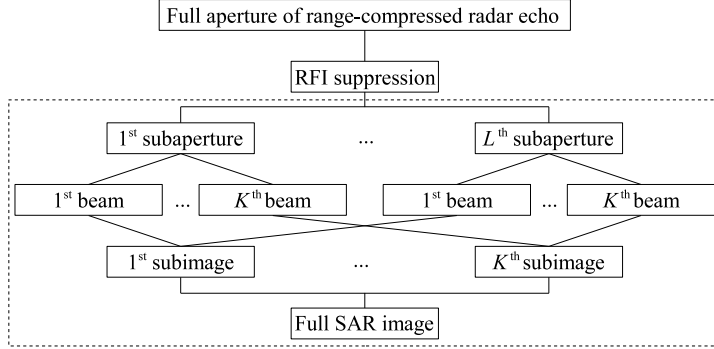


Figure 4: The proposed RFI suppression scheme. The time-domain LBP algorithm is bounded by the dashed-line rectangle.

processed by ALE and then by the Local Backprojection algorithm (LBP) [10]. This algorithm will be presented in detail in Section 4 where a possibility to integrate the RFI suppression approach into SAR imaging algorithms is suggested. In the following RFI suppression experiment, an adaptive filter of the order $L = 1024$ has been used in the ALE and the delay set to $n_0 = 1$. The selection of β is critical for the performance of the NLMS when using an ALE [6]. In this paper, the step size of NLMS is experimentally selected by $\beta = 0.1$. The estimated radar signal plus the thermal noise signal is given to $e(n)$ in Fig. 1 and is plotted in Fig. 3(c). In the context of this paper, the estimated radar signal plus the thermal noise signal using the proposed RFI suppression approach is called the estimated signal using ALE and denoted by ψ_{ALE} in the plots. Its amplitude is significantly lower than the amplitude of the radar echo containing the RFI signal which is plotted in Fig. 3(a). The magnitude of the DFT of the estimated signal using ALE is shown in Fig. 3(d) and is substantially flatter as compared to the magnitude of the DFT of the radar echo containing the RFI signal given in Fig. 3(b). A new SAR image is formed by the estimated signal using ALE and is shown in Fig. 2(b). The ground scene in general and the corner reflector in particular can now be observed.

A basic evaluation of the proposed RFI suppression approach is facilitated by comparing it to the LRF technique [8] which is currently used in CARABAS-II data processing. The linear filter in LRF is defined by inverting the averaged range frequency response. This technique has been proven

Table 1: Measured results on the point target.

	SINR	Δ_r	ISLR	PSLR
ALE IR-SAR	≈ 27 dB	≈ 2.8 m	≈ -40 dB	≈ -20 dB
LRF IR-SAR	≈ 28 dB	≈ 3.0 m	≈ -33 dB	≈ -17 dB

to be robust, non-adaptive over one aperture, non-supportive for real-time processing and unable to handle short-time RFI. The estimated radar signal using this technique is called the estimated signal using LRF and denoted by ψ_{LRF} in the plots. The estimated signal using LRF and the magnitude of its DFT are shown in Fig. 3(d) and 3(e), respectively. The estimated signal using ALE can be visually evaluated to be almost identical to the estimated signal using LRF. In the frequency-domain, the flatness of the magnitude of the DFT of the estimated signal using ALE is close to the one using LRF. However, using ALE to suppress RFI may cause frequency attenuations at the RFI frequencies. This is demonstrated in the experiments on the simulated data given in [9]. There is no clear difference between the SAR image formed with the estimated signal using ALE, given in Fig. 2(b), and the SAR image formed with the estimated signal using LRF, given in Fig. 2(c).

This situation can be further evaluated by SAR image quality assessments. These assessments are are routinely made with the help of corner reflectors which are widely used for calibration in field campaigns [11]. In the considered SAR scene, SAR image quality assessments are possible due to the corner reflector deployed in the center of the SAR scene, appearing as a point target in the SAR images. The Signal-to-Interference-Noise ratio (SINR) is estimated by the ratio of the peak intensity of the point target to the average intensity in the area ($-512 : -256, 0 : 256$) of the SAR images. In this area, backscattering from the surrounding clutter is low. The results, which are summarized in Table 1, show that SINR measured on the SAR image formed with the estimated signal using ALE is 1 dB lower in comparison to the one using LRF. This can be interpreted as the estimated error caused by ALE.

At the peak intensity of the point target in the SAR images, vectors are extracted in the range direction. The reason for this extraction is explained by the more sensitivity of the sidelobes in the range direction compared to in the azimuth direction produced by UWB SAR systems [12]. These vectors are

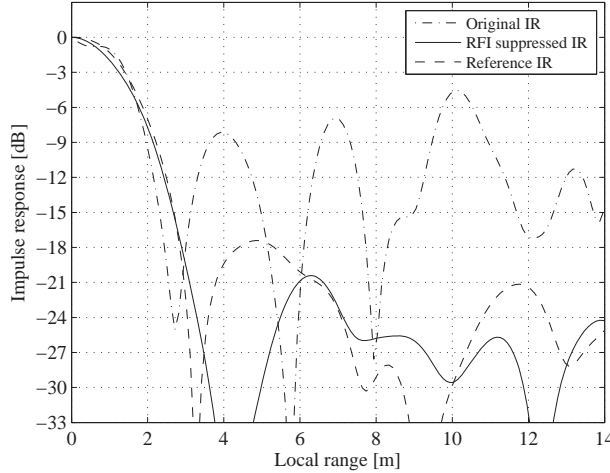


Figure 5: IR-SAR of the point target extracted in the range direction from the SAR images formed with the radar echo containing the RFI signal, the estimated signal using ALE and the estimated signal using LRF.

interpreted as measured Impulse Responses in SAR imaging (IR-SAR) [13] in the range direction of the point target. They are normalized with respect to the peak intensity of the point target, and then plotted in the same figure for comparison purposes. As shown in Fig. 5, the measured IR-SAR extracted from the SAR image formed with the radar echo containing the RFI signal, which is briefly called as original IR-SAR in this paper, is seriously distorted. For this reason, the point target is difficult to see in this SAR image. Some differences between the measured IR-SAR, which are extracted from the SAR image formed with the estimated signal using ALE (ALE IR-SAR), and the measured IR-SAR extracted from the SAR image formed with the estimated signal using LRF (LRF IR-SAR), can also be observed in Fig. 5. These differences may be generated from the non-adaptive (average) and adaptive characteristics of the two approaches. The measured results from these IR-SAR, stated as range resolution, Integrated Sidelobe Ratio (ISLR) and Peak Sidelobe Ratio (PSLR), are also summarized in Table 1. They show that in this specific case, the performance of the proposed approach is similar to that of the LRF technique.

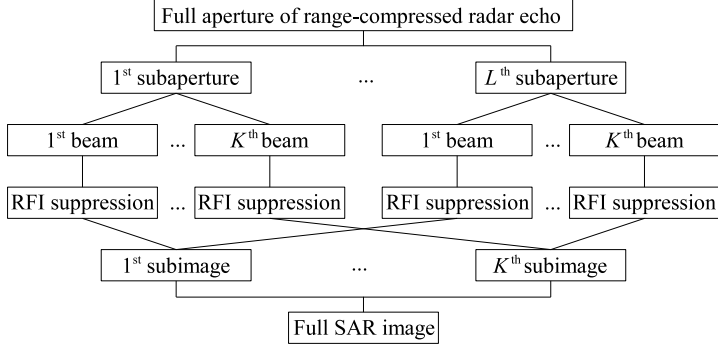


Figure 6: A scheme to integrate the RFI suppression approach into LBP.

According to (7), the performance of ALE depends strongly on the ratio of the ability to de-correlate the UWB radar signal in the radar echo $d(n)$ and in the reference signal $x(n)$. In other words, it depends on the interrelation of the UWB radar signal bandwidth and the RFI signal bandwidth. In environments where there are RFI with bandwidths so large that they might also be de-correlated by the minimum delay selection n_0 , the ALE performance is likely to decrease.

4 Possibility to Integrate The RFI Suppression Approach into SAR Imaging Algorithms

In this section, we discuss a possibility to integrate the proposed RFI suppression approach into SAR imaging algorithms. The background of this discussion is due to the computational burden required by the proposed RFI suppression. The experimental results indicate that the proposed approach using ALE allows for adaptive and efficient RFI suppression in terms of quality. However, this process may be inefficient in terms of processing time. In order to keep the computational burden down, this paper also suggests integrating the RFI suppression approach into SAR imaging algorithms. The discussion will focus on time-domain algorithms which are recommended for UWB SAR data processing [14].

In the SAR technique, a time-domain backprojection algorithm refers to a superposition of the backprojected radar echo. To save processing time, it

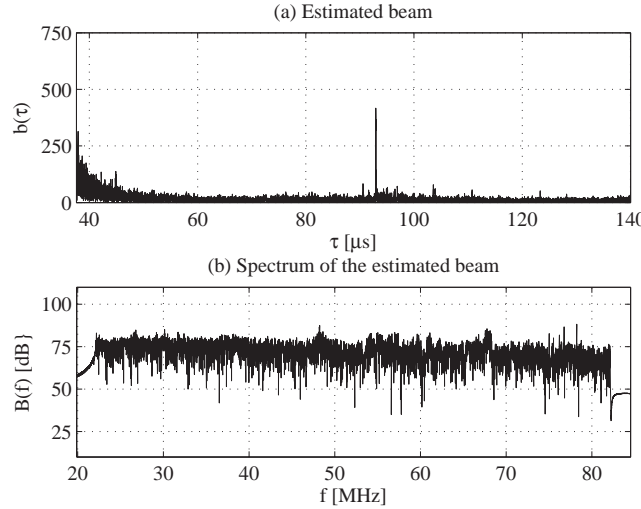


Figure 7: (a) the estimated beam using ALE and (b) the magnitude of its DFT. The original beam is formed by 32 original radar echoes containing the RFI signal.

is recommended to process the radar echo on a subaperture, subimage basis and in multiple beam-forming stages [15], i.e. Fast Factorized Backprojection (FFBP). The integration of the RFI suppression approach into any beam-forming stage helps to reduce the number of operations.

We consider here a two-stage SAR imaging algorithm, i.e. LBP [10]. In LBP, the complete aperture and the full SAR image are segmented in M subapertures and K subimages, respectively. The reconstruction of the imaged scene is therefore split into two stages, beam-forming and backprojection. In the beam-forming stage, from the center of the m -th subaperture x_m , the k -th beam, aiming at the center of the k -th subimage, is formed by a superposition of all radar echo data in the subaperture. The k -th subimage is then backprojected by the k -th beam. This procedure is repeated for all subapertures. The full SAR image is retrieved by a coherent combination of all subimages. The RFI suppression approach can be integrated into LBP between the beam-forming and backprojection stages. With such, the number

of operations required by the approach is reduced by

$$\frac{N_{sub-a} \times N_{sub-b}}{N_{sub-i}}, \quad (10)$$

where N_{sub-a} and N_{sub-i} are the number of the aperture positions in one subaperture and the number of subimages, respectively. The ratio of the original radar echo sample to the beam sample is denoted by N_{sub-b} . The proposed scheme for this integration is sketched in Fig. 6. Fig. 7 plots an example of an estimated beam using ALE. In this example, the beam is formed with a subaperture of $N_{sub-a} = 32$ aperture positions and the number of subimages is $N_{sub-i} = 4$. For illustration purposes, we use the ratio of the original radar echo sample to the beam sample $N_{sub-b} = 1$. The amplitude of the estimated beam is shown in Fig. 7(a) and the magnitude of its DFT in Fig. 7(b). The magnitude of its DFT can be evaluated as moderately flat. However, in this example, the number of operations required to run the approach is reduced by a factor of 8. The RFI suppressed beams can then be used in the backprojection stage to form a SAR image.

5 Conclusion

In this paper, an approach to suppress RFI in UWB low frequency SAR is proposed. The approach is based on the ALE mechanism controlled by NLMS. The approach is tested successfully on the CARABAS-II data. The possibility to integrate this RFI suppression approach into SAR imaging algorithms in order to obtain efficiency in processing time is also discussed.

References

- [1] R. Goodman, S. Tummala, and W. Carrara, "Issues in ultra-wideband, widebeam SAR image formation," in *Proc. IEEE International Radar Conference*, Alexandria, VA, May 1995, pp. 479–485.
- [2] C. T. Le, S. Hensley, and E. Chapin, "Adaptive filtering of RFI in wideband SAR signals," *7th Annual JPL Airborne Earth Science Workshop*, Jet Propulsion Laboratory, Pasadena, CA, Jan. 1998.
- [3] X. Luo, L.M.H. Ulander, J. Askne, G. Smith, and P.-O. Frolind, "RFI suppression in ultra-wideband SAR systems using LMS filters infrequency domain," *IET Electronics Letters*, vol. 37, no. 4, pp. 241–243, 2001.

- [4] H. Kimura, T. Nakamura, and K. P. Papathanassiou, "Suppression of ground radar interference in JERS-1 SAR data," *IEICE Trans. Commun.*, vol. 87, no. 12, pp. 3759–3765, 2004.
- [5] A. Reigber and L. Ferro-Famil, "Interference suppression in synthesized SAR images," *IEEE Geosci. Rem. Sens. Lett.*, vol. 2, no. 1, pp. 45–49, 2005.
- [6] Monson H. Hayes: *Statistical digital signal processing and modeling*, Wiley, 1996
- [7] A. Gustavsson, L. M. H. Ulander, B. H. Flood, P.-O. Frölind, H. Hellsten, T. Jonsson, B. Larsson, and G. Stenstrom, "Development and operation of an airborne VHF SAR system-lessons learned," in *Proc. IEEE IGARSS'98*, vol. 1, Seattle, WA, Jul. 1998, pp. 458–462.
- [8] L. M. H. Ulander, and P.-O. Frölind "Precision processing of CARABAS HF/VHF-band SAR data," in *Proc. IEEE IGARSS'99*, vol. 1, Hamburg, Germany, Jun. 1999, pp. 47–49.
- [9] V. T. Vu, T. K. Sjögren, M. I. Pettersson, and L. Håkansson, "An approach to suppress RF interference in Ultrawideband low frequency synthetic aperture radar," in *Proc. IEEE Radar 2010*, Washington, DC, May 2010, accepted for publication.
- [10] O. Seger, M. Herberthson, and H. Hellsten, "Real time SAR processing of low frequency ultra wide band radar data," in *Proc. EUSAR'98*, Friedrichshafen, Germany, May 1998, pp. 489–492.
- [11] M. Shimada, O. Isoguchi, T. Tadono, K. Isono, "PALSAR Radiometric and Geometric Calibration," *IEEE Trans. Geosci. Remote Sensing*, vol. 47, no. 12, pp. 3915–3932, 2009.
- [12] V. T. Vu, T. K. Sjögren, M. I. Pettersson, and A. Gustavsson, "Definition on SAR image quality measurements for UWB SAR," in *Proc. SPIE Image and Signal Processing for Remote Sensing XIV*, vol. 7109, Cardiff, UK, Sep. 2008, pp. 71091A (1–9).
- [13] V. T. Vu, T. K. Sjögren, M. I. Pettersson, and H. Hellsten, "An impulse response function for evaluation of UWB SAR imaging," *IEEE Trans. Signal Processing*, revised for publication.

- [14] V. T. Vu, T. K. Sjögren, and M. I. Pettersson, “A comparison between fast factorized backprojection and frequency-domain algorithms in UWB low frequency SAR,” in *Proc. IEEE IGARSS’2008*, Boston, MA, Jul. 2008, pp. 1293–1296.
- [15] L. M. H. Ulander, H. Hellsten, and G. Stenstrom, “Synthetic-aperture radar processing using fast factorized back-projection,” *IEEE Trans. Aerosp. Electron. Syst.*, vol. 39, no. 3, pp. 760–776, 2003.

Part II—B

Part II–B

A Comparison between Fast Factorized
Backprojection and Frequency-domain
Algorithms in UWB Low Frequency SAR

Part II–B is published as:

V. T. Vu, T. K. Sjögren, and M. I. Pettersson, “A comparison between fast factorized backprojection and frequency-domain algorithms in UWB low frequency SAR,” in *Proc. IEEE IGARSS’2008*, Boston, MA, Jul. 2008, pp. IV-1284–IV-1287.

A Comparison between Fast Factorized Backprojection and Frequency-domain Algorithms in UWB Low Frequency SAR

Viet T. Vu, Thomas K. Sjögren, and Mats I. Pettersson

Abstract

Two frequency-domain algorithms Chirp Scaling (CS) with the advantage of simplification and Range Migration (RM) with the advantage of accuracy are candidates for a comparative study to the time-domain algorithm Fast Factorized Backprojection (FFBP) with reference to a UWB system are presented in this paper. The comparison is based on UWB SAR image quality measurements such as spatial resolution, Integrated Sidelobe Ratio (ISLR) and Peak Sidelobe Ratio (PSLR) and processing time connected to computational complexity. The simulated SAR data, which is used in this study, is based on the parameters of the airborne UWB low frequency CARABAS-II system.

1 Introduction

Different algorithms have been proposed to process SAR images. The main objectives of algorithms are image quality, time consumption connected to computational cost and other aspects related to application. SAR image processing algorithm can be divided into two main groups: time-domain and frequency domain algorithms.

Global Backprojection (GBP) algorithm [1] is known as the basic of the time-domain algorithms to reconstruct the image scene. According to GBP, a SAR image is considered as a linear transformation from the radar echo data and can be considered to be a reference SAR image in UWB SAR image quality measurements. The main disadvantage of GBP which exists parallel with advantages of GBP such as perfect motion compensation, unlimited scene size, perfect focus and local processing is computation cost. For N aperture points

and SAR image of $N \times N$ pixels, the number of operations needed for GBP is proportional to N^3 . Fast time-domain algorithms were proposed to overcome the drawback of the GBP, for example Local Backprojection (LBP) [2] and Fast Factorized Backprojection (FFBP) [3] running roughly $N^2\sqrt{N}$ and $N^2\log(N)$ times faster than GBP, respectively. Range Migration algorithm (RM) [4], Range-Doppler (RD) [5] and Chirp Scaling (CS) [6] are examples of frequency-domain algorithms. Both RM and RD require computationally expensive interpolation while among CS algorithm avoids interpolation and can be efficiently performed by complex multiplications and Fast Fourier Transforms (FFT). However, in derivations of both CS and RD, high order phase terms in some steps are discarded. For this reason, RM may be the most suitable frequency-domain algorithm for UWB low frequency SAR systems.

In comparative studies between algorithms, either timedomain algorithms or frequency-domain algorithms are usually compared together. For example, a comparison of different FFBP versions is presented in [7]. In [8], a comparison of CS and RM for airborne low frequency SAR data processing is given. Another comparative study of RD and RM algorithms concentrates on focusing quality can be found in [9]. However, there have not been many comparisons between time-domain and frequency-domain algorithms even though they form two main SAR processing algorithm groups.

In this paper, two frequency-domain algorithms including CS with the advantage of simplification and RM with the advantage of accuracy are candidates for a comparative study to a fast time-domain algorithm FFBP using simulated CARABAS-II data [10]. The comparison is based on UWB SAR image quality measurements such as spatial resolution, Integrated Sidelobe Ratio (ISLR) and Peak Sidelobe Ratio (PSLR) [11] and processing time connected to computational complexity.

The paper is organized as follows: Section 2 describes briefly different algorithms. Theory of SAR image quality measurements is presented in Section 3. A comparative study of different algorithms is given in Section 4. Section 5 provides the conclusions.

2 Algorithms to Process UWB SAR Data

2.1 Factorized Fast Backprojection

FFBP [3] which is based on LBP [2] can be interpreted as LBP processing data in multiple beamforming stages socalled factorization. For FFBP, the range

compressed data is mapped into first order beams. The beams are formed by short first order subaperture and the beam size should be large to cover the first order large images. A number of first order beams are combined together to form a second order beam corresponding to the combination of a number of first order subapertures. The size of second order beam is smaller and covers the second order subimages which are created by the division of the first order subimages. Beamforming stages are repeated until the final beamforming stage. The number of beamforming stages or factorizations depends strongly on SAR system parameters, required image quality and processing time. In the final stage, the subimages are mapped by beams formed at the final beamforming stage. A full SAR image is obtained by a coherent combination of all subimages processed by the full aperture.

2.2 Range Migration

RM [4] enables to reconstruct the image of large scenes at fine resolution. RM requires the so-called Stolt interpolation which can be interpreted as a change of variables in the frequency domain by the relationship

$$\omega = \frac{c}{2} \sqrt{k_x^2 + k_r^2} \quad (1)$$

where ω is the signal frequency, k_x and k_r are azimuth and range wavenumbers, respectively, and c is the speed of light. The focusing equation of RM can be rewritten as

$$h(x, r, -t_0) = \frac{c}{8\pi^2} \int \int G(k_x, r=0, k_r) \frac{k_r}{\sqrt{k_x^2 + k_r^2}} \exp \left\{ -i \frac{ct_0}{2} \sqrt{k_x^2 + k_r^2} \right\} \exp \{i(k_x x + k_r r)\} dk_x dk_r \quad (2)$$

where $G(k_x, r=0, k_r)$ is measured field which has been changed variable at $r=0$ of the superposition of plane waves with different wavelengths and azimuth wavenumbers in two-dimensional frequency domain at the emitted time t_0 .

2.3 Chirp Scaling

Approximations in derivation of the original CS [6] by Taylor expansion to second order are valid for conventional narrow band SAR systems but might not completely valid for UWB systems associated with large integration angle.

A conventional approach to such a problem is to introduce a Taylor expansion up to higher order phase terms and take spatial variant range migration into account. Nonlinear CS (NCS) proposed in [12] with the consideration up to cubic phase terms for Taylor expansion combined with cubic order nonlinear chirp rate to process squint mode SAR data is therefore a good candidate to process UWB mode SAR data. According to NCS [12], the range frequency rate K_r is assumed to vary linearly with the range-time from reference trajectory

$$K_r = K_{ref} + K_s \frac{2(r_0 - r_{ref})}{c\beta} \quad (3)$$

where r_0 and r_{ref} are minimum range distance to a point target and reference range, respectively. β is a function of azimuth frequency f_x and defined in [6] as

$$\beta = \sqrt{1 - \left(\frac{cf_x}{2f_c v_{pl}} \right)^2} \quad (4)$$

An extra cubic phase filter is performed in two-dimensional frequency domain by

$$H_{Cubic}(f_t, f_\tau) = \exp \left\{ i \frac{2\pi}{3} \left[\frac{K_s}{2K_{ref}^2} \left(\frac{2-\beta}{1-\beta} \right) - \frac{3r_0}{cf_c^2} \left(\frac{\beta^2-1}{\beta^5} \right) \right] f_\tau^3 \right\} \quad (5)$$

References functions including chirp scaling, range compression and residual error compensation functions are

$$H_{CS,3}(f_t, f_\tau) = H_{CS,2}(f_t, f_\tau) \cdot \exp \left\{ i \frac{\pi}{3} \left[K_s \left(\frac{1-\beta}{\beta} \right) \left(\tau - \frac{2r_{ref}}{c\beta} \right) \right] \right\} \quad (6)$$

$$H_{RC,3}(f_t, f_\tau) = H_{RC,2}(f_t, f_\tau) \cdot \exp \left\{ i \frac{\pi}{3} \left[\frac{1}{K_{ref}} (1+\beta) \right] f_r^3 \right\} \quad (7)$$

and

$$H_{RES,3}(f_t, f_\tau) = H_{RES,2}(f_t, f_\tau) \cdot \exp \left\{ i \frac{\pi}{3} \left[\frac{K_{ref}}{f_c} \frac{(1-\beta)^2(1+\beta)}{\beta^5} \right] \left[\frac{2(r_0 - r_{ref})}{c} \right]^3 \right\} \quad (8)$$

where $H_{CS,2}(f_t, f_\tau)$, $H_{RC,2}(f_t, f_\tau)$ and $H_{RES,2}(f_t, f_\tau)$ are the reference functions of original CS which can be found in [6].

Table 1: CARABAS-II's main parameters.

Parameter	Value
The highest frequency channel processed	82 MHz
The lowest frequency channel processed	22 MHz
Platform speed v_{pl}	128 m/s
Flight altitude	3700 m
Minimum range to the aim point	7150 m
PRF	137 Hz

3 SAR Image Quality Measurements

Analyses in [12] have shown that the mainlobe and sidelobe areas are more suitably defined by ellipses. Based on these analyses, definitions on SAR image quality measurement such as Integrated Sidelobe Ratio (ISLR) and Peak Sidelobe Ratio (PSLR) have been proposed. Due to the fact that UWB SAR system is always associated with large integration angle to handle azimuth focusing, investigations of spatial resolution, ISLR and PSLR under different integration angles are also proposed in [12]. In this comparative study, we consider spatial resolutions, ISLR and PSLR to evaluate quantitatively the performance of the algorithms mentioned in Section 2.

4 SAR Comparative Studies

The simulated data which is used in this study is based on parameters of the CARABAS-II system given in Table 1. To obtain a fair comparison, no weighting function or sidelobe control approach is used. With the CARABAS-II parameters given in Table 1, we can consider the integration angles in the range from 5 to 70 degrees in this comparative study [11]. Three algorithms FFBP, RM and NCS are subjects to be compared. However, not all of these algorithms are completely valid for CARABAS-II data processing and this can be explained as follows. In SAR system design, the PRF must be chosen larger or equal to two times maximum Doppler frequency which is a function of maximum integration angle and signal fractional bandwidth. For CARABAS-

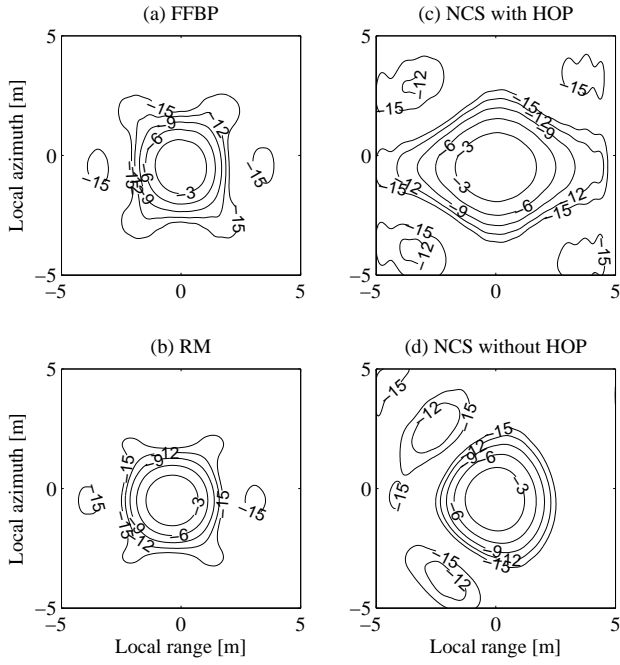


Figure 1: The contour plots of a point target processed by different algorithms at integration angle of 35 degrees. Level steps from 0 to -15 dB are taken into account.

II, high PRF with regard to extremely large integration angle (up to 150 degrees) may make both original CS and NCS invalid since the term β may get complex values at certain azimuth frequencies. Neither FFBP nor RM suffers from such problem. For comparison purposes, the data is simulated with low PRF (only 68.5 Hz instead of 137 Hz).

For NCS, we also need to eliminate Higher Order Phase (HOP) terms (from 4th order) in the Taylor expansion to avoid effects such as azimuth-range coupling [12] caused by unconsidered HOP terms. Figure 1.c shows the degrading of the SAR image quality caused by HOP terms.

Nearest neighbor interpolator is used in both RM and FFBP in change of variable and beam forming stages after 10 times upsampling data, respectively.

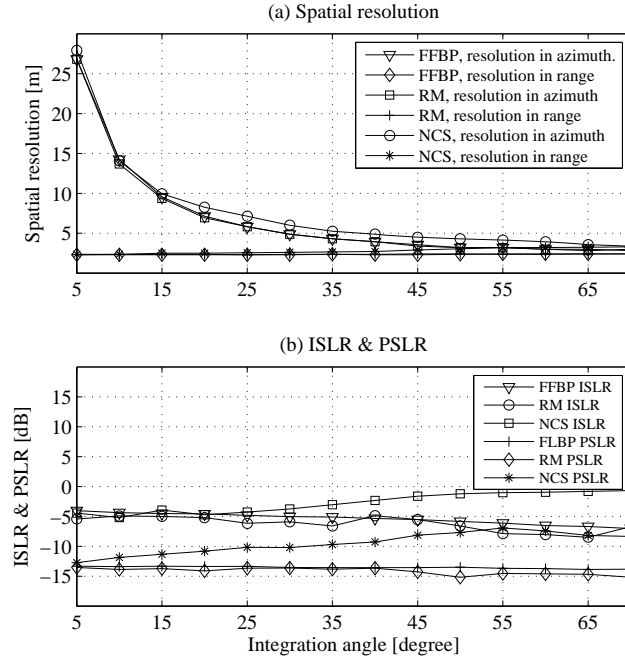


Figure 2: SAR image quality measurements.

For FFBP, we process the data in 3 stages with the factorization of 4 for both subaperture and subimage in every stage. The numbers of the subaperture positions and subimages are 16 and 4, respectively. Figure 1.a, 1.b and 1.d show the contour plots of a point target processed by FFBP, RM and NCS. At the first glance, we can see a better image quality obtained by FFBP and RM than by NCS at a large integration angle.

Measured spatial resolutions which are interpreted to be the distance between two objects on the ground at which the objects appear distinct and separate on SAR images are shown in Figure 2.a. If there is no motion error, RM can obtain the same spatial resolutions in azimuth and range as FFBP. Comparative resolutions are achieved by NCS at small integration angles. However, they go slightly bad at large integration angles (from 20 degrees). The measurement results of ISLR in Figure 2.b show again the worse perfor-

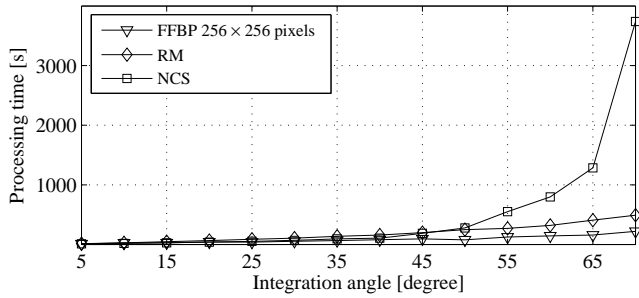


Figure 3: Processing time measured by Matlab.

mance of NCS at large integration angles when much more energy spills over to the sidelobes compared to RM and FFBP. Figure 2.b also shows the high sidelobe level of NCS even at small integration angles. This can be explained by phase errors caused by approximation in derivation steps of NCS. This leads to poor ability of NCS to image weak reflective targets affected by a strong reflective target nearby. NCS may therefore not be totally suitable for UWB SAR processing.

A comparison in term of processing time connected to computational complexity may be hard to be performed in an analytic way due to different basic operations used in time-domain and frequency-domain algorithms. For RM and NCS, operations which are mainly used are FFT, IFFT and multiplication while among FFBP uses only addition and multiplication. Figure 3 shows a comparison of the processing time taken by FFBP, RM and NCS for the same numbers of image pixels. At small integration angles (up to 45 degrees) NCS which can be performed efficiently by FFT/IFFT and multiplications and does not require any interpolation shows the best performance in term of the processing time. However, computational cost of NCS increases rapidly at large integration angles due to extra steps required by NCS (not required by original CS) such as cubic phase filter and HOP elimination performed in twodimensional frequency domain. With a simple interpolator such as a linear one, the computational cost of RM can be kept small at large integration angles. Computational cost will increase for both RM and NCS if motion compensation is included. As mentioned, processing time taken by FFBP depends strongly on factorization. However, in this comparison FFBP requires

highest computational cost as shown in Figure 3 since the local processing is not taken into account.

5 Conclusion

Algorithms FFBP, RM and NCS are subjects to be compared in this study. If there is no motion error caused by airborne SAR systems, RM is an excellent candidate for UWB SAR processing in terms of SAR image quality and processing time. The study shows also that NCS may not be totally suitable for UWB SAR processing, especially at large integration angles (from 20 degrees). Although FFBP shows the best performance in term of SAR image quality, the processing time is still the problem for time-domain algorithms in general and FFBP in specific.

References

- [1] L. E. Andersson, "On the determination of a function from spherical averages," *SIAM Journal on Mathematical Analysis*, vol. 19, no. 1, pp. 214–232, 1988.
- [2] O. Seger, M. Herberthson, and H. Hellsten, "Real time SAR processing of low frequency ultra wide band radar data," in *Proc. EUSAR'98*, Friedrichshafen, Germany, May 1998, pp. 489–492.
- [3] L. M. H. Ulander, H. Hellsten, and G. Stenstrom, "Synthetic-aperture radar processing using fast factorized back-projection," *IEEE Trans. Aerosp. Electron. Syst.*, vol. 39, no. 3, pp. 760–776, 2003.
- [4] J. R. Bennett and I. G. Cumming, "Digital processor for the production of Seasat synthetic aperture radar imagery," in *Proc. International Conference On Seasat-SAR Processor*, Frascati, Italy, Dec. 1979, ESA-SP-154.
- [5] C. Cafforio, C. Prati, and F. Rocca, "SAR data focusing using seismic migration techniques," *IEEE Trans. Aerosp. Electron. Syst.*, vol. 27, pp. 194–207, Mar. 1991.
- [6] R. K. Raney, H. Runge, R. Bamler, I. G. Cumming, and F. H. Wong, "Precision SAR processing using chirp scaling," *IEEE Trans. Geosci. Remote Sensing*, vol. 32, no. 4, pp. 786–799, 1994.

- [7] T. K. Sjögren, V. T. Vu, M. I. Pettersson, "A comparative study of the polar version with the subimage version of fast factorized backprojection in UWB SAR," in *Proc. IEEE IRS'08*, Wroclaw, Poland, May. 2008, pp. 156–159.
- [8] A. Potsis, A. Reigber, E. Alivizatos, A. Moreira, and N. K. Uzunoglu, "Comparison of chirp scaling and wavenumber domain algorithms for airborne low-frequency SAR," in *Proc. SPIE SAR Image Analysis, Modeling, and Techniques V*, vol. 4883, Agia Pelagia, Greece, Mar. 2003, pp. 11–19.
- [9] R. Bamler, "A comparison of range-doppler and wavenumber domain SAR focusing algorithms," *IEEE Trans. Geosci. Remote Sensing*, vol. 30, no. 4, pp. 706–713, 1992.
- [10] A. Gustavsson, L. M. H. Ulander, B. H. Flood, P.-O. Frölind, H. Hellsten, T. Jonsson, B. Larsson, and G. Stenstrom, "Development and operation of an airborne VHF SAR system—lessons learned," in *Proc. IEEE IGARSS'98*, vol. 1, Seattle, WA, Jul. 1998, pp. 458–462.
- [11] V. T. Vu, T. K. Sjögren, M. I. Pettersson, and A. Gustavsson, "Definition on SAR image quality measurements for UWB SAR," in *Proc. SPIE Image and Signal Processing for Remote Sensing XIV*, vol. 7109, Cardiff, UK, Sep. 2008, pp. 71091A (1–9).
- [12] G. W. Davidson, I. G. Cumming, and M. R. Ito, "A chirp scaling approach for processing squint mode SAR data," *IEEE Trans. Aerosp. Electron. Syst.*, vol. 32, no. 1, pp. 121–133, 1996.

Part II—C

Part II–C

On Apodization Techniques
for Ultra-wideband SAR Imaging

Part II–C is published as:

V. T. Vu, T. K. Sjögren, and M. I. Pettersson, “On apodization techniques for ultra-wideband SAR imaging,” in *Proc. EURAD’2009*, Roma, Italy, Sep. 2009, , pp. 529–532.

On Apodization Techniques for Ultra-wideband SAR Imaging

V. T. Vu, T. K. Sjögren, and M. I. Pettersson

Abstract

Ultra-wideband (UWB) SAR imaging suffers from a number of inherent problems in which the apodization has not been investigated appropriately. This paper presents a discussion on apodization techniques and possibilities to apply these techniques to UWB SAR imaging.

1 Introduction

Over the last decades, Synthetic Aperture Radar (SAR) has attracted considerable interest as the number of applications in geosciences, remote sensing, surveillance and reconnaissance increases. The ability to effectively collect data in severe conditions such as rain, clouds and/or darkness is considered to be the main advantage of SAR systems as compared to other imaging sensors. Ultra-wideband (UWB) SAR is understood as SAR systems utilizing a large fractional bandwidth and a widebeam antenna. Experimental UWB SAR systems such as CARABAS-II [1] and LORA [2] allow detecting changes in dense forested areas or under camouflage as well as moving objects. More importantly, the UWB SAR systems facilitate high resolution imaging.

UWB SAR imaging faces inherent challenges such as the choice of processing algorithm, integration angle, apodization, motion compensation and RF interference. These challenges have ever been indicated in [3]. Investigations into UWB SAR imaging algorithms associated with the motion compensation issue have been mentioned in some recent publications. For example, a comparison between time- and frequency-domain imaging algorithms for UWB SAR can be found in [4] and a research on focusing SAR data acquired from nonlinear sensor trajectories in [5]. In these publications, time-domain algorithms have shown the superiority in UWB SAR imaging over frequency-domain algorithms due to their inherent characteristics like adjustable scene

size imaging, local processing and manageable motion compensation. A general view of the ability to handle azimuth focusing associated with integration angle in UWB SAR imaging is presented in [6]. However, the apodization in UWB SAR imaging has either been mentioned sparsely, for example in [7], or studied inappropriately.

Unlike narrowband and narrowbeam SAR imaging, where only orthogonal sidelobes are dominant, there exists both orthogonal and non-orthogonal sidelobes in UWB SAR imaging, which if not be handled will degrade the SAR image quality significantly. An example of this degradation, which is based on Integrated Sidelobe Ratio (ISLR) and Peak Sidelobe Ratio (PSLR) measurements, is demonstrated in [6].

Applying two-dimensional (2D) weighting functions to the spectrum of SAR images in wave-domain can be seen as the simplest appodization techniques. Mostly used weighting functions are Rectangle, Hamming, Hanning and Blackman. Although such techniques can somewhat control the sidelobe level they are usually accompanied with a loss in spatial resolutions. Nonlinear apodization techniques such as Dual-apodization, Complex Dual Apodization (CDA) and Spatially Variant Apodization (SVA) [8], which are known as a class of nonlinear operators, enable to suppress sidelobes and maintain the spatial resolution, simultaneously.

The objective of this paper is to discuss several apodization techniques for UWB SAR imaging. Simulated SAR data is used in the demonstrations. The reference system in this study is the airborne UWB low frequency SAR system CARABAS-II [1]. Global Backprojection (GBP) [9] is selected as the UWB SAR imaging algorithm due to its accuracy, ability to handle large integration angles and manageable motion compensation.

The paper is organized as follows. Section 2 reviews the apodization techniques and evaluates their validity for UWB SAR imaging. Section 3 presents the simulation results of apodization in UWB SAR imaging. Section 4 provides the conclusions.

2 Apodization Technique

In this section, we review the currently used apodization techniques as well as examine the possibilities to apply them to UWB SAR imaging. Applying 2D weighting functions to the spectrum of SAR images in wave-domain is called the linear apodization techniques to distinguish from the nonlinear apodization techniques in this paper. Analysis in this section is based on the

spectrum of a SAR image in wave-domain, as shown in Fig. 1. The azimuth wave number k_x , the range wave number k_r and the radar frequency ω are connected together by the relationship

$$\omega = \frac{c}{2} \sqrt{k_x^2 + k_r^2} \quad (1)$$

where c is the speed of light.

2.1 Linear Apodization Technique

Applying 2D weighting functions to the spectrum of SAR images in wave-domain for apodization always accompanies with a loss in resolution. For narrowband and narrowbeam SAR imaging, where the spectrum is approximated to a rectangular area, this loss is generally acceptable. However, this exchange may be either inefficient or extremely expensive in UWB SAR imaging since the rectangular approximation is not valid. The inefficiency is here interpreted as the existence of the non-orthogonal sidelobes after applying 2D weighting functions whereas the expensiveness regards the loss in resolution.

To illustrate this, we investigate effects of a weighting function, for example Rectangle, on UWB SAR imaging. The weighting function is denoted by the continuous-line rectangle in Fig. 1 and represented mathematically by

$$W_1(k_x, k_r) = \text{rect}\left(\frac{k_x}{2k_c \sin\frac{\phi_0}{2}}\right) \cdot \text{rect}\left(\frac{k_r - k_c}{\Delta k_r}\right) \quad (2)$$

where k_c is the center wave number, ϕ_0 is the integration angle and

$$\Delta k_r = k_{r,max} - k_{r,min} \quad (3)$$

with $k_{r,max}$ and $k_{r,min}$ are maximum and minimum range wave numbers, respectively. This weighting function results in a new spectrum marked by the dark gray area in Fig. 1. Although the spatial resolutions can approximately be maintained the non-orthogonal sidelobes are not suppressed. This is interpreted as the result of missing corners in the new spectrum. To suppress the non-orthogonal sidelobes, we can use a narrower weighting function, e.g. $W_2(k_x, k_r)$ which is marked by the fine-dashed-line rectangle in Fig. 1

$$W_2(k_x, k_r) = \text{rect}\left(\frac{k_x}{2k_{r,min} \tan\frac{\phi_0}{2}}\right) \cdot \text{rect}\left(\frac{k_r - k'_c}{\Delta k'_r}\right) \quad (4)$$

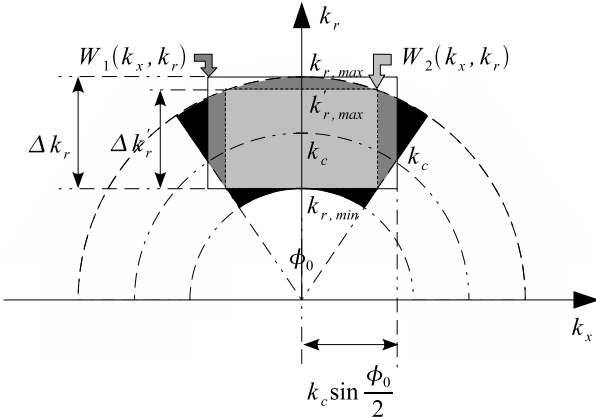


Figure 1: An example of UWB SAR spectrum (black area). Applying a Rectangle weighting function (fine-dashed-line rectangle) $W_1(k_x, k_r)$ results in a new spectrum (dark gray area). If another Rectangle weighting function (continuous-line rectangle) $W_2(k_x, k_r)$ is used, the spectrum is limited by a narrower area (the light gray area).

where

$$\Delta k'_r = \sqrt{k_{r,max}^2 - k_{r,min}^2 \tan^2 \frac{\phi_0}{2}} - k_{r,min} < \Delta k_r \quad (5)$$

and

$$k'_c = k_{r,min} + \frac{\Delta k'_r}{2} < k_c \quad (6)$$

The reductions in the center frequency, i.e. k_c , and the bandwidth, i.e. Δk_r cause the loss in azimuth and range resolutions, respectively. Based on the later weighting function $W_2(k_x, k_r)$, the loss in azimuth resolution can be predicted to be more sensitive than in range. For a UWB SAR system such as CARABAS-II with the fractional bandwidth $B_r \approx 1.3$ and the maximum integration angle $\phi_0 \approx 110^\circ$, the loss in azimuth resolution can be up to 200%. Other weighting functions such as Hamming, Hanning and Blackman are alternatives for the linear apodization technique. However, due to their large mainlobe broadening factors, the loss in resolutions caused by these weighting functions is even higher than Rectangle with the same window size.

2.2 Nonlinear Apodization Technique

Nonlinear apodization techniques are known as the techniques which can control sidelobes efficiently but avoid the loss in spatial resolutions. Basically, such techniques can be used for UWB SAR imaging since they are only a combination of the linear apodization techniques and nonlinear operators in which the nonlinear operators is used to maintain the spatial resolutions. For Dual-apodization, a SAR scene is imaged with and without a weighting function, i.e. unweighted and weighted SAR images, respectively. An apodized SAR image is assigned the minimum magnitudes from this pair of SAR images on a pixel-by-pixel basis. If the apodization is based on three or more weighting functions, it can be named Tri-apodization or Multi-apodization, respectively.

To retain the phase information, the pair of unweighted and weighted SAR images should be analyzed in real (I or in-phase) and imaginary (Q or quadrature) parts. The assignment is performed separately on both real and imaginary parts. On the pixel-by-pixel basic, the real part of an apodized SAR image is assigned either zeros, if the values from the pair of SAR images posses opposite signs, or minimum absolute values otherwise. The assigning zero is interpreted as an intermediate weighting function. A similar assignment is implemented for the imaginary part. Due to a separated consideration of the real and imaginary parts of SAR images, this procedure is named as CDA technique. The intermediate weighting function in CDA is synonymous with that there exists neither Complex Tri- nor Multi-apodization.

The selection of the weighting functions for Dual-apodization or CDA is obviously critical for the apodized SAR images. However, there is no optimum weighting function for all SAR scenes. A weighting function, which is optimum for one SAR scene, may not be optimum for the others. Nonlinear apodization technique using a dynamic weighting function, i.e. cosine-on-pedestal, is known as SVA. The dynamical weighting factor is assigned by values from 0, i.e. Rectangle, to 0.5, i.e. Hanning. Unfortunately, this technique supports only rectangular SAR image's spectrum and therefore is not suitable for UWB SAR imaging.

Nonlinear apodization in UWB SAR imaging usually requires more than two weighting functions due to the non-rectangular spectrum and the criticalness of the weighting function selection. With such, Tri-apodization and Multi-apodization seem to be good candidates for UWB SAR imaging. However, using the cosine-on-pedestal function to design optimized weighting functions, i.e. optimize the trade-off between the non-orthogonal sidelobe suppres-

sion and the loss in resolution, for linear apodization and Tri-apodization or Multi-apodization is promising.

3 Apodization in UWB SAR Imaging

In this section, we demonstrate the apodization techniques which have been discussed in the previous section. The demonstrations are based on the SAR data simulated according to the parameters of the airborne UWB low frequency SAR system CARABAS-II. Contours at level from -30 to 0 dB -3 dB with a step of -3 dB are used to plot SAR images. Fig. 2.a shows an example of a point target imaged by a UWB SAR system with the fractional bandwidth $B_r \approx 1.3$ and an arbitrary integration angle $\phi_0 = 65^0$. Both orthogonal and non-orthogonal sidelobes are seen clearly in the SAR image.

3.1 Linear Apodization in UWB SAR Imaging

In this demonstration, we apply the Rectangle weighting function $W_2(k_x, k_r)$ given in (4) to the image's spectrum, effects of the apodization on the image, which has been proved in the previous section, can now be seen clearly in the Rectangle-apodized image in Fig. 2.b. The non-orthogonal sidelobes are suppressed significantly compared to Fig. 2.a. The loss in azimuth resolution is moderately high (about 200%), whereas the range resolution decreases slightly. Fig. 2.c. shows another apodized image being applied a Hanning weighting function

$$W_3(k_x, k_r) = \left[0.5 + \xi_x \cos \left(\frac{\pi k_x}{k_c \tan \frac{\phi_0}{2}} \right) \right] \cdot \left[0.5 + \xi_r \cos \left(\frac{2\pi (k_r - k_c)}{\Delta k_r} \right) \right] \quad (7)$$

where $\xi_x = \xi_r = 0.5$. The predicted effects on the SAR image are here illustrated. The non-orthogonal sidelobes are totally removed. Due to the broadening factor (about 1.62) of the Hanning weighting function, the loss in both azimuth and range resolutions is about 62% compared to the non-apodized case. The loss in resolution and the non-orthogonal sidelobe suppression can be optimized by a Cosine-on-pedestal function (7) with a reasonable selection of the weighting factors in azimuth ξ_x and range ξ_r . In this demonstration, the weighting factors are selected as $\xi_x = \xi_r = 0.17$. The apodized image is shown in Fig. 2.d with sufficiently suppressed non-orthogonal sidelobes and a loss in resolutions of about 33%.

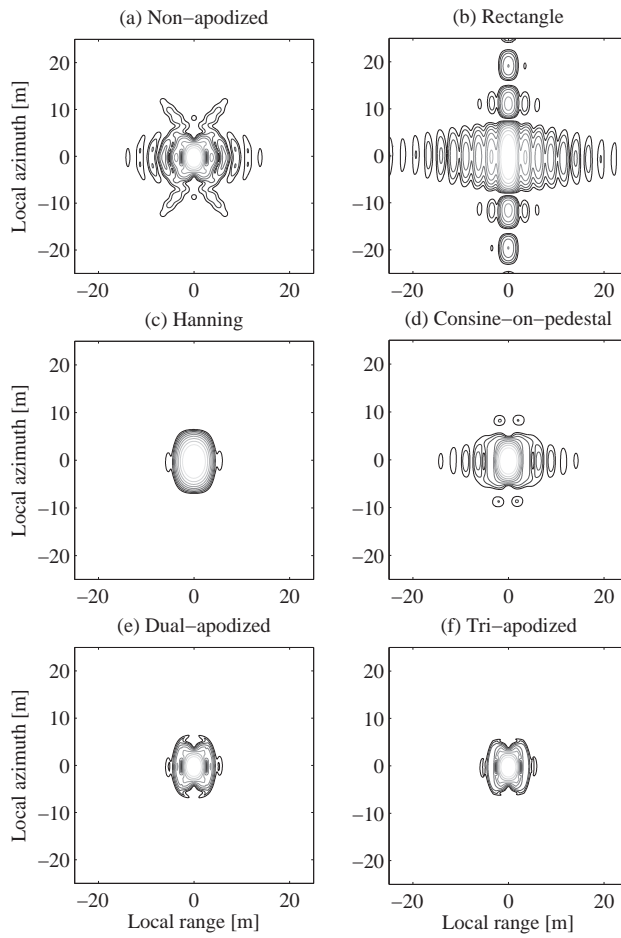


Figure 2: A point target is imaged by a UWB SAR system with the fractional bandwidth $B_r \approx 1.3$, the integration angle $\phi_0 = 65^0$, and the minimum range to the point target $r_0 = 7200$ m. (a) Non-apodized, (b) Rectangle weighting function, (c) Hanning weighting function, (d) Consine-on-pedestal, (e) Dual-apodized, (f) Tri-apodized.

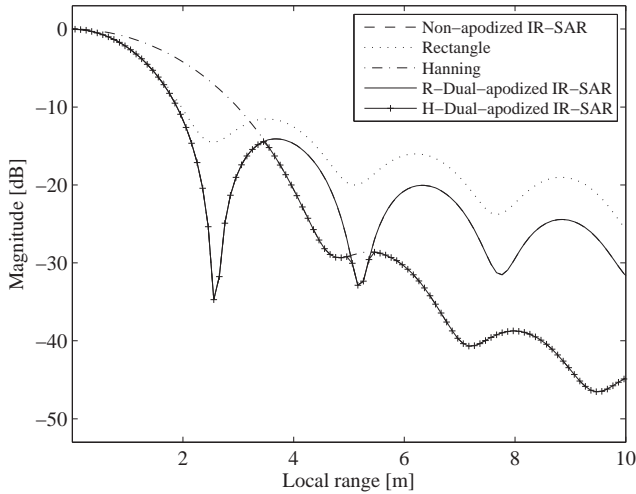


Figure 3: Dual-apodization incorporated with the Rectangle and Hanning windows. The R-Dual-apodized IR-SAR denotes the result of the Dual-apodization incorporated with the Rectangle weighting function and H-Dual-apodized with the Hanning weighting function.

3.2 Nonlinear Apodization in UWB SAR Imaging

The original- (non-apodized), Rectangle-apodized, Hanning-apodized and Cosine-on-pedestal images are seen as the inputs for a linear operator in the nonlinear apodization techniques. The output is an apodized image without degrading spatial resolutions. Fig. 3 illustrates the nonlinear operator, which can be seen as the key step to avoiding the loss in resolutions. The Impulse Responses in SAR imaging (IR-SAR) in range direction of a point target are dual-apodized with the Rectangle and Hanning weighting functions whose the mainlobe broadening factors are 1 and 1.62, respectively. As shown in Fig. 3, Dual-apodization has no almost effect if it is incorporated with the Rectangle weighting function. This confirms again the criticalness of the weighting function selection.

The Dual-apodization incorporated with the Hanning weighting function sketched in Fig. 3 indicates that the first sidelobe is not apodized enough

Table 1: ISLR and PSLR Measured Results.

	Non-apodized	Dual-apodized	Tri-apodized
ISLR	-7 dB	-10 dB	-12 dB
PSLR	-14 dB	-14.5 dB	-19 dB

whereas the higher order sidelobes are suppressed efficiently and drop below -30 dB. The Dual-apodized image is given in Fig. 2.e where both orthogonal and non orthogonal are suppressed significantly without any loss in resolutions. To get a better evaluation of the Dual-apodization, we measure ISLR and PSLR on the Dual-apodized image and compare to the non-apodized results. The measured ISLR and PSLR are summarized in Table 1 where the gain in PSLR with the Dual-apodization is low (only about 0.5 dB). An extra weighting function is still needed to suppress the first sidelobe. The requirement for the weighting function is to utilize a suitable mainlobe broadening factor. One possibility is based on the Kaiser windows with a suitable sidelobe attenuation factor. An alternative is to use the Cosine-on-pedestal which is mentioned in the previous section.

In the next demonstration, the linear operator considers the original- (non-apodized), Hanning-apodized and Cosine-on-pedestal images as its inputs, i.e. Tri-apodization. The Tri-apodization result is presented in Fig 4 where the first sidelobe level is reduced to -19 dB. The Tri-apodized SAR image is sketched in Fig. 2.e. The gains in ISLR and PSLR with the Tri-apodization are about 5 dB. As mentioned, the selection of the weighting functions for nonlinear apodization is always critical. To avoid this, the apodization should be incorporated with even more weighting functions, i.e. Multi-apodization.

4 Conclusions

In this paper, we present a discussion on the apodization techniques and the possibilities to apply them to UWB SAR imaging. The linear apodization techniques are usually associated with either the high loss in resolution or the inefficiency in controlling the non-orthogonal sidelobes. However, they can still be used for UWB SAR imaging by suitable weighting functions. Nonlinear apodization techniques are promising for UWB SAR imaging thanks to their

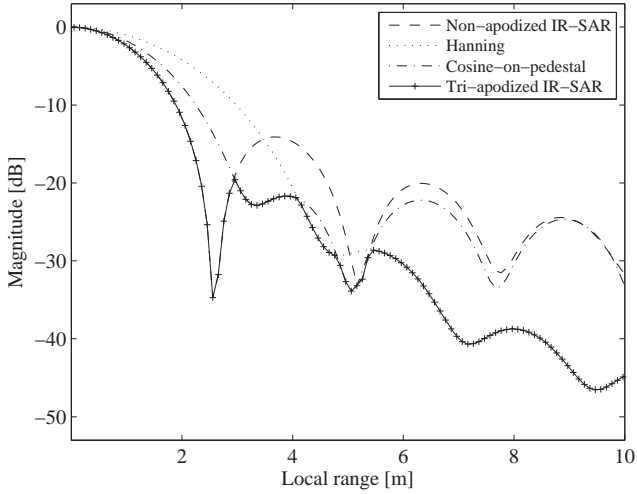


Figure 4: Tri-apodization incorporated with the Hanning and Cosine-on-pedestal weighting functions. The first sidelobe is suppressed about 5 dB.

characteristic - without degrading the spatial resolutions. However, among currently used nonlinear apodization techniques, Multi-apodiation including Tri-apodization can facilitate the apodization in UWB SAR imaging due to the criticalness of the weighting function selection. These conclusions are illustrated by tests and measurements on the simulated SAR data, which is based on the CARABAS-II parameters.

References

- [1] H. Hellsten, L. M. H. Ulander, A. Gustavsson, and B. Larsson, “Development of VHF CARABAS II SAR,” in *Proc. SPIE Radar Sensor Technology*, vol. 2747, Orlando, FL, Apr. 1996, pp. 48–60.
- [2] L. M. H. Ulander and H. Hellsten, “Low-frequency ultrawideband array-antenna SAR for stationary and moving target imaging,” in *Proc. SPIE Radar Sensor Technology IV*, vol. 3704, Orlando, FL, Apr. 1999, pp. 149–158.

- [3] R. Goodman, S. Tummala, and W. Carrara, "Issues in ultra-wideband, widebeam SAR image formation," in *Proc. IEEE International Radar Conference*, Alexandria, VA, May 1995, pp. 479–485.
- [4] V. T. Vu, T. K. Sjögren, and M. I. Pettersson, "A comparison between fast factorized backprojection and frequency-domain algorithms in UWB low frequency SAR," in *Proc. IEEE IGARSS'2008*, Boston, MA, Jul. 2008, pp. 1293–1296.
- [5] O. Frey, C. Magnard, M. Rüegg, and E. Meier, "Focusing SAR data acquired from non-linear sensor trajectories," in *Proc. IEEE IGARSS'2008*, Boston, MA, Jul. 2008, pp. 415–418.
- [6] V. T. Vu, T. K. Sjögren, M. I. Pettersson, and A. Gustavsson, "Definition on SAR image quality measurements for UWB SAR," in *Proc. SPIE Image and Signal Processing for Remote Sensing XIV*, vol. 7109, Cardiff, UK, Sep. 2008, pp. 71091A (1–9).
- [7] X. Xu and R. M. Narayanan, "Enhanced resolution in SAR/ISAR imaging using iterative sidelobe apodization," *IEEE Trans. Image Processing*, vol. 14, no. 4, pp. 537–547, 2005.
- [8] H. C. Stankwitz, R. J. Dallaire, and J. R. Fienup, "Nonlinear apodization for sidelobe control in sar imagery," *IEEE Trans. Aerosp. Electron. Syst.*, vol. 31, no. 1, pp. 267–279, 1995.
- [9] L. E. Andersson, "On the determination of a function from spherical averages," *SIAM Journal on Mathematical Analysis*, vol. 19, no. 1, pp. 214–232, 1988.

Part III—A

Part III–A

Detection of Moving Targets by Focusing in
UWB SAR—Theory and Experimental Results

Part III–A is published as:

V. T. Vu, T. K. Sjögren, and M. I. Pettersson, “Detection of moving targets by focusing in UWB SAR – Theory and experimental results,” *IEEE Trans. Geosci. Remote Sensing*, vol. 48, no. 10, pp. 3799–3815, 2010.

Detection of Moving Targets by Focusing in UWB SAR—Theory and Experimental Results

V. T. Vu, T. K. Sjögren, M. I. Pettersson,
A. Gustavsson and L. M. H. Ulander

Abstract

Moving target detection in ultrawideband (UWB) synthetic aperture radar (SAR) is associated with long integration time and must accommodate azimuth focusing for reliable detection. This paper presents the theory on detection of moving targets by focusing and experimental results on single-channel SAR data aimed at evaluating the detection performance. The results with respect to both simulated and real data show that the ability to detect moving targets increases significantly when applying the proposed detection technique. The improvement in signal-to-clutter noise ratio (SCNR) which is a basic requisite for evaluating the performance reaches approximately 20 dB using only single-channel SAR data. This gain will be preserved for the case of multi-channel SAR data. The reference system for this study is the airborne UWB low frequency SAR CARABAS-II.

1 Introduction

Over the last decades, synthetic aperture radar (SAR) has attracted considerable interest as the number of applications in geoscience, remote sensing, surveillance and reconnaissance increases. The ability to effectively collect data in severe conditions such as rain, clouds and/or darkness is considered to be the main advantage of SAR systems as compared to other imaging sensors. Ultrawideband (UWB) SAR is understood as SAR systems utilizing either a large absolute bandwidth or a large fractional bandwidth signal and a wide antenna beamwidth. Examples of experimental UWB SAR systems are CARABAS-II operating in the lower VHF-band from 20 to 90 MHz [1], LORA in the VHF- and UHF-bands from 200 to 800 MHz [2], P-3 with a bandwidth

of 515 MHz in the VHF/UHF-bands 215-900 MHz [3], ground-based Boom-SAR with a spectral response extending from 50 MHz to 1200 MHz [4] and PAMIR with a very high simultaneous bandwidth of 1820 MHz in X-band [5]. Such systems usually enable high resolution imaging. Systems operating at low radar frequencies, e.g. CARABAS, allows to detect changes in dense forested areas or under camouflage [6]. Such applications are of interest to both military and civilian end-users.

In this paper, we concentrate on another application of UWB SAR: detection of moving targets which is most commonly realized by ground moving target indication (GMTI) implementations based on antenna array solutions. A moving object is displaced and defocused as an elliptic or a hyperbolic curve in a SAR image [7]. For conventional SAR, i.e. small bandwidth signal and narrow beamwidth, the displacement and defocusing in a SAR image is mainly caused by movements in the range and azimuth directions, respectively. For UWB SAR, objects moving in the range direction can be both displaced and defocused in a SAR image due to long integration time. The detection of moving targets, however, cannot be based on such features. A stationary target with an elliptic or hyperbolic shape can give rise to a false detection. Disappearance of moving targets in a SAR image is also possible due to the dispersion of the energy reflected from them. In many cases, the target may be fully obscured by surrounding clutter.

Several moving target detection methods have been proposed. The detection of moving targets can be based on Doppler effect [8]. However, the detection is only possible if the speed of the target is high enough to produce Doppler frequencies which are distinguishable from the surrounding stationary clutter. Alternatively, moving target detection can be achieved by using displaced phase center antenna (DPCA) [9] or space time adaptive processing (STAP) [10] techniques. Access to an array antenna gives the opportunity to also correct for the displacement caused by the SAR process. An overview of multi-channel SAR GMTI is given in [11]. However, such techniques are not available for single-channel SAR data. The detection can also be based on the phenomenon that the shadow projected by the target will produce zeros in a SAR image [12]. Strong back scattering from the background is required for this approach. Detection based on phase-errors caused by moving targets is suggested in [13]. A complex SAR image is divided into patches where the phase-error is estimated separately in each patch. The magnitude of the phase-error estimate is measured and, if it exceeds a given threshold, indicates the presence of a moving target. In addition, there are also new detection methods based on, for example, the capabilities of dual-frequency

millimeter wave SAR with monopulse processing for GMTI [14] or PolSAR imagery for moving target detection/ ship detection [15].

The goal of this paper is to present the theory of the moving target detection by focusing technique in UWB SAR and experimental results aimed at evaluating the gain in detection ability. This detection technique is based on the detection scheme proposed in [16] and the optimum relative speed discretisation derived in [17]. The experimental results upon single-channel UWB low frequency SAR data shows a significant improvement in detection ability achieved with this detection technique. This improvement will be preserved when the detection technique is performed on multi-channel SAR data. The moving targets in our experiments are selected in the areas with low backscattering. This makes the evaluation of the gain in detection ability more efficient. In the experiments, we use both real and simulated data based on the airborne UWB low frequency SAR CARABAS-II. The real data have been collected by CARABAS-II in two different field campaigns.

The paper is organized as follows. Section 2 briefly describes the likelihood ratio test (LRT) for moving target detection. Section 3 describes in detail the relative speed concept. Issues related to moving target focusing are presented in Section 4. Section 5 presents the theory of the moving target detection by focusing technique and experiments upon simulated data. Experimental results on real data collected in the two field campaigns are given in Sections 6 and 7. Section 8 provides the conclusions and outlines future work.

2 Likelihood Ratio Test for Moving Target Detection

The most commonly used radars for GMTI are based on antenna array solutions but often without SAR capabilities. However, SAR systems are becoming more and more important for GMTI since in SAR GMTI systems the moving target will not only be detected but also imaged in its surroundings.

For moving target detection, two hypotheses on the sampled radar echo \mathbf{Y} can be given: a moving object exists, i.e. the received signal consists of the reflection from the moving object \mathbf{S} , (hypothesis H_1) or no moving object exists (hypothesis H_0). In both cases, the received signal contains clutter connected to the radar backscattering \mathbf{C} and noise \mathbf{N} originating from

thermal noise in the system

$$\begin{aligned} H_1 : \mathbf{Y} &= \mathbf{S} + \mathbf{C} + \mathbf{N} \\ H_0 : \mathbf{Y} &= \mathbf{C} + \mathbf{N}. \end{aligned} \quad (1)$$

The LRT for moving target detection, known as an optimal detection scheme in the maximum likelihood sense, is given by

$$\Lambda = \frac{P(\mathbf{Y} | H_1)}{P(\mathbf{Y} | H_0)}. \quad (2)$$

Different optimal schemes for detection in the maximum likelihood sense have been proposed. In [18], with an assumption of Gaussian probability density functions (PDF) for clutter and noise, the optimal scheme for detection can be written as

$$\Lambda = \max \left| \mathbf{Y}^T \mathbf{R}^{-1} \mathbf{S}^* (f_D, k_D) \right| \begin{cases} \geq \lambda \text{ decision for } H_1 \\ < \lambda \text{ decision for } H_0 \end{cases} \quad (3)$$

where \mathbf{R} is the covariance matrix and λ is a suitable threshold. This is equivalent to multiplying the received signal by a weighting vector

$$\mathbf{w}_{opt} = \mathbf{R}^{-1} \mathbf{S}^* (f_D, k_D) \quad (4)$$

where knowledge of Doppler frequency f_D and Doppler chirp rate k_D can be obtained by an open-loop technique or a closed-loop technique [18].

Another solution for LRT in the case of local backprojection (LBP) [19] SAR processing is given in [16] as

$$\Lambda = \left| \sum_{l=1}^{N_a} \frac{1}{R_{c,l}^2} \sum_{m=0}^{N_f-1} e^{j k_m r_l} \mathbf{A}_{ml}^H (\theta'_l) \mathbf{R}_{ml}^{-1} \tilde{\mathbf{Y}}_{ml} \right|^2 \begin{cases} \geq \lambda \text{ decision for } H_1 \\ < \lambda \text{ decision for } H_0 \end{cases} \quad (5)$$

where l is the subaperture number, m is the frequency number, r_l is the range to a moving target in the l -th subaperture beam, k_m is the wavenumber at m -th frequency, $R_{c,l}$ is the range from the center of the l -th subaperture to subimage, $\tilde{\mathbf{Y}}_{ml}$ is the subaperture beam measurement vector, \mathbf{R}_{ml} is the covariance matrix, and $\mathbf{A}_{ml} (\theta'_l)$ is the steering vector at m and l for the moving target. If only single-channel data is used, the steering vector $\mathbf{A}_{ml} (\theta'_l)$ is

equal to one. The detection here is carried out as follows: First, multi-channel subapertures are formed from multi-channel SAR data. The clutter suppression is then performed on these subapertures by the covariance \mathbf{R}_{ml} and the target steering vector $\mathbf{A}_{ml}(\theta'_l)$. The subapertures are combined together using different r_l (dependent on the difference velocity of the platform velocity and the target velocity) to focus the target energy. In [16], the clutter suppression step was tested with good results on the multi-channel C-band data. In this paper, the experiments on the single-channel UWB low frequency SAR data shows a significant increase in detection ability when using the correct difference velocity in the SAR image formation.

3 Normalized Relative Speed

Let the ground coordinates be given by a Cartesian coordinate system (ξ, η, ζ) as shown in Fig. 1. If all movements are assumed to have constant speeds, i.e. no acceleration, and to be linear, the movement of the target can then be represented by the coordinates

$$\begin{aligned}\xi_{tg}(t) &= v_\xi \cdot (t - t_0) + \xi_0 \\ \eta_{tg}(t) &= v_\eta \cdot (t - t_0) + \eta_0 \\ \zeta_{tg}(t) &= 0\end{aligned}\tag{6}$$

where t_0 is the time at the minimum range r_0 . The ground coordinates of the target at r_0 are ξ_0 and η_0 . On the other hand, the linear movement of the platform is given by

$$\begin{aligned}\xi_{pl}(t) &= v_{plt} \\ \eta_{pl}(t) &= 0 \\ \zeta_{pl}(t) &= h.\end{aligned}\tag{7}$$

Given the coordinates of the ground target and the platform, the slow-time dependent range is defined by

$$\bar{r}_t(t) = \sqrt{[\xi_{pl}(t) - \xi_{tg}(t)]^2 + [\eta_{pl}(t) - \eta_{tg}(t)]^2 + [\zeta_{pl}(t) - \zeta_{tg}(t)]^2}.\tag{8}$$

A moving target can be considered as a stationary target in the SAR formation process if the platform carrying the SAR equipment is assumed to move with the difference velocity \vec{v}_s of the original platform velocity \vec{v}_{pl} and the target velocity \vec{v}_{tg} [16]. Hence, the slow-time dependent range in image

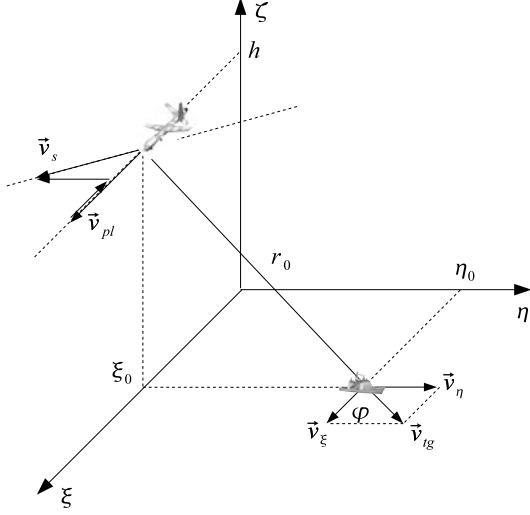


Figure 1: SAR system geometry, \vec{v}_{pl} is the velocity and h is the altitude of the platform. The velocity of the target \vec{v}_{tg} can be analyzed by velocities \vec{v}_ξ and \vec{v}_η in ξ and η directions, respectively and φ is the moving direction of the target with respect to the flight track. The ground coordinates ξ_0 and η_0 are positions at the minimum range r_0 and \vec{v}_s is the difference vector of \vec{v}_{pl} and \vec{v}_{tg} .

coordinates (x, r) can also be written as

$$\bar{r}_t(t) = \sqrt{(v_{st} - x_0)^2 + r_0^2} \quad (9)$$

where x_0 is the platform position at the minimum range. The terms r_0 , v_s , t_0 and x_0 are connected together by the relationship

$$x_0 = v_s t_0 \quad (10)$$

If we substitute (6) and (7) into (8) and then equalize the coefficients of t^2 , t and the constants in (8) and (9), v_s and the position of the moving target in the image coordinates are found to be

$$v_s = \sqrt{(v_{pl} - v_\xi)^2 + v_\eta^2}, \quad (11)$$

$$r_0 = \sqrt{\eta_0^2 \cdot \left[1 + \left(\frac{v_\eta}{v_{pl} - v_\xi} \right)^2 \right] + h^2}, \quad (12)$$

and

$$x_0 = \frac{v_s}{v_{pl}} \left(\xi_0 - \frac{v_\eta}{v_{pl} - v_\xi} \eta_0 \right). \quad (13)$$

The normalized relative speed (NRS) γ_t is defined by the length of the difference velocity \vec{v}_s which is normalized with respect to the platform speed v_{pl}

$$\gamma_t = \sqrt{\frac{(v_{pl} - v_\xi)^2 + v_\eta^2}{v_{pl}^2}}, \quad (14)$$

With such, (9) can be rewritten in a more convenient form as

$$\bar{r}_t(t) = \sqrt{\gamma_t^2 \cdot (v_{plt} - x'_0)^2 + r_0^2} \quad (15)$$

where

$$x'_0 = \xi_0 - \frac{v_\eta}{v_{pl} - v_\xi} \eta_0. \quad (16)$$

Equation (15) is called the focusing equation and can be found also in [16]. A moving target can be focused in the SAR image simply by scaling the speed of the platform with γ_t .

4 Moving Target Focusing

The focusing approach can be carried out differently depending on which image formation algorithm is used. In general, algorithms can be divided into two groups: time- and frequency-domain. Both of them have been proved to be applicable to the focusing approach [20, 21].

Global backprojection (GBP) [22], a time-domain algorithm, has been used in [20] to focus moving target for detection. The moving target focusing is obtained exactly by (9). However, this algorithm normally requires extremely long processing time. To save the processing time, we can use faster time-domain algorithms such as LBP [19] or fast backprojection (PBP) [23]. To avoid distance compensation and subimage shifts associated with LBP [24], we propose to use PBP. Beside this, fast factorized backprojection (FFBP) [25, 26] can also be an option for the moving target focusing.

In [21], the moving target focusing is based on a frequency-domain algorithm, range migration (RM) [27]. A new wavenumber in azimuth k_x' scaled with γ_t to focus the moving target is given by

$$k_x' = \frac{2\pi f_x}{\gamma_t v_{pl}} \quad (17)$$

where f_x is the azimuth frequency. However, RM requires the Stolt interpolation and this leads to high computational complexity. Ultrawideband chirp scaling (UCS) [28], which is a candidate for UWB SAR data processing, does not require interpolation and can be efficiently performed by complex multiplications and fast Fourier transforms (FFT); it thus has the advantage of short processing time and is also selected as a candidate for the focusing approach. In this section, we present guidelines to focus moving targets using PBP and UCS.

4.1 Moving Target Focusing Using PBP

In PBP [23], two concepts - polar image and slant-range image - are used. Similar to LBP, PBP divides the complete aperture into subapertures. The selection of subaperture size is based on the SAR system parameters and has a direct influence on image quality and processing time. However, any selection must ensure that the phase error is smaller than $\pi/8$ (far field condition). From the center of each subaperture, a polar grid ($\cos\hat{\alpha}, \hat{r}$) is created. The polar grid must cover the full slant-range image and meet the Nyquist sampling requirements for $\hat{\alpha}$ and \hat{r}

$$\Delta\cos\hat{\alpha} < \frac{c}{2f_{max}L_s} \quad (18)$$

$$\Delta\hat{r} < \frac{c}{2B} \quad (19)$$

where f_{max} is the maximum radar signal frequency, L_s is the subaperture size, c is the speed of light and B is the signal bandwidth. In PBP, the polar images are retrieved by superposition of backprojected data in polar grids. The range from a position in the l -th subaperture to a pixel (m, n) of the l -th polar image is determined by

$$\tilde{r}_{l,m,n}(t) = \sqrt{(v_{pl}t - x_l - \hat{r}_n \cos\hat{\alpha}_m)^2 + (\hat{r}_n \sin\hat{\alpha}_m)^2}. \quad (20)$$

The slant-range image is obtained by a linear mapping from all the polar images. The range from the center of the l -th subaperture to a slant-range image pixel (x_i, r_j) and cosine of the angle between the range and the flight track vectors are derived as

$$\bar{r}_{l,i,j} = \sqrt{(x_l - x_i)^2 + r_j^2} \quad (21)$$

$$\cos(\bar{\alpha}_{l,i,j}) = \frac{x_l - x_i}{\bar{r}_{l,i,j}}. \quad (22)$$

Moving target focusing can be obtained by scaling the speed of the platform with NRS in (20), i.e. focusing in the polar image formation

$$\begin{aligned} \tilde{r}_{l,m,n}(t) = \\ \sqrt{\gamma_t^2 \cdot (v_{plt} t - x_l - \hat{r}_n \cos \hat{\alpha}_m)^2 + (\hat{r}_n \sin \hat{\alpha}_m)^2}. \end{aligned} \quad (23)$$

The focusing can also be carried out by scaling the speed of the platform with γ_t in (21), i.e. focusing in the slant-range image formation

$$\bar{r}_{l,i,j} = \sqrt{\gamma_t^2 \cdot (x_l - x_i)^2 + r_j^2}. \quad (24)$$

For FFBP, the focusing can be performed on either any beam forming stage or the image formation stage. This issue is presented in detail in [29, 30].

4.2 Moving Target Focusing Using UCS

Due to the approximations in chirp scaling (CS) [31], it may only be valid for a limited number of SAR systems which utilize small fractional bandwidth and narrow beamwidth. A proposal to apply nonlinear chirp scaling (NCS) to process CARABAS-II data has been given in [32]. However, with such proposal, we must reduce the PRF (considering one out of several adjacent radar echo data) to keep the term β real at all azimuth frequencies with a high possibility of aliasing

$$\beta = \sqrt{1 - \left(\frac{c f_x}{2 f_c v_{plt}} \right)^2} \quad (25)$$

where f_c is the center frequency and f_x is the azimuth frequency. The idea behind UCS is to manipulate a higher speed of the SAR platform in processing,

i.e. scaling the speed of the SAR platform with NRS $\gamma_u > 1$, to keep β in real at all azimuth frequencies [28]

$$\beta = \sqrt{1 - \left(\frac{c f_x}{2 f_c \gamma_u v_{pl}} \right)^2}. \quad (26)$$

The condition for γ_u is retrieved directly from (26) as

$$\gamma_u > \frac{\lambda_c}{4 \Delta L} \quad (27)$$

where ΔL is the space between two adjacent SAR platform positions. Defocusing caused by γ_u will be compensated in the phase functions. In addition, the space-variant range migration existing in UWB SAR is handled by using the nonlinear FM filtering method [33], i.e. NCS. An extra phase filter $\psi_0(f_t, f_\tau)$ in the two-dimensional (2D) frequency domain is introduced in [28] as

$$\psi_0(f_t, f_\tau) = \exp [i\pi Y(f_t) f_\tau^3 + i\pi Z(f_t) f_\tau^4] \quad (28)$$

where f_τ is the range frequency, $Y(f_t)$ and $Z(f_t)$ are the azimuth frequency varying phase filter coefficients. UCS phase functions of chirp scaling, range compression and residual phase correction, which include the compensation for the defocusing caused by γ_u , are presented in details in [28]. For UCS, moving target focusing can be reached by scaling again the platform speed using the true NRS γ_t in (26) as

$$\beta = \sqrt{1 - \frac{1}{\gamma_t^2} \left(\frac{c f_x}{2 f_c \gamma_u v_{pl}} \right)^2}. \quad (29)$$

4.3 Moving Target Focusing Tests

In moving target focusing tests, we use simulated data based on the parameters of the airborne UWB low frequency SAR CARABAS-II [1] in order to keep consistency with the later experiments. These parameters were used in the data collection campaign in the Simrishamn area in 1999 and are given in Table 1. Experiments on real data will be given in Sections 6 and 7.

To test the ability of focusing a moving target with NRS, we assume that there are two known moving point targets. One moves with speed $v_{tg} = 5.34$ m/s toward $\varphi = 81.5^\circ$ with respects to the flight track as shown in Fig. 1 and the other toward $\varphi = -65.2^\circ$ with the same speed. Estimated NRS are

Table 1: The parameters used in the measurement campaign in Simrishamn.

Parameter	Value
The highest frequency processed	82 MHz
The lowest frequency processed	22 MHz
Platform speed v_{pl}	128 m/s
Full aperture length	19200 m
Full aperture positions	20480
Flight altitude	3700 m
Minimum range to the aim point	7150 m
PRF	137 Hz

$\gamma_t = 0.959$ and $\gamma_t = 1.0378$. The radar cross section (RCS) of the target with $\gamma_t = 1.0378$ is normalized to $\sigma = 1$, the other with $\gamma_t = 0.959$ $\sigma = 0.25$. In addition, a number of stationary point targets with RCS $\sigma = 0.25, 0.5, 0.75$ and 1 are also present in order to investigate the effects caused by the focusing approach to a SAR image. The thermal noise is assumed to be additive white Gaussian noise (AWGN) at the level of -10 dB. Fig. 2.a shows the 250 m \times 250 m SAR image of the five stationary targets and two moving targets processed by PBP. However, the size of a SAR image processed by UCS is specified by the considered number of aperture positions and the number of range data. Fig 2.d shows part of the original SAR image processed by UCS.

The moving targets are displaced and defocused in the SAR images. One appears on the left hand side of the SAR images as elliptic curves and the other on the right hand side is surrounded by four stationary targets. Fig. 2.b and 2.e show the SAR images of the stationary point target and the moving targets after applying the focusing approach using a known NRS $\gamma_t = 0.959$. The stationary targets in the center and surrounding the moving target on the right hand side of the SAR images are now defocused and appear as elliptic curves. The moving target on the left hand side of the SAR images is strongly defocused and appears almost as a straight line. Meanwhile, the moving target surrounded by the stationary targets on the right hand side of the SAR images is now focused to the original shape (point) and can be

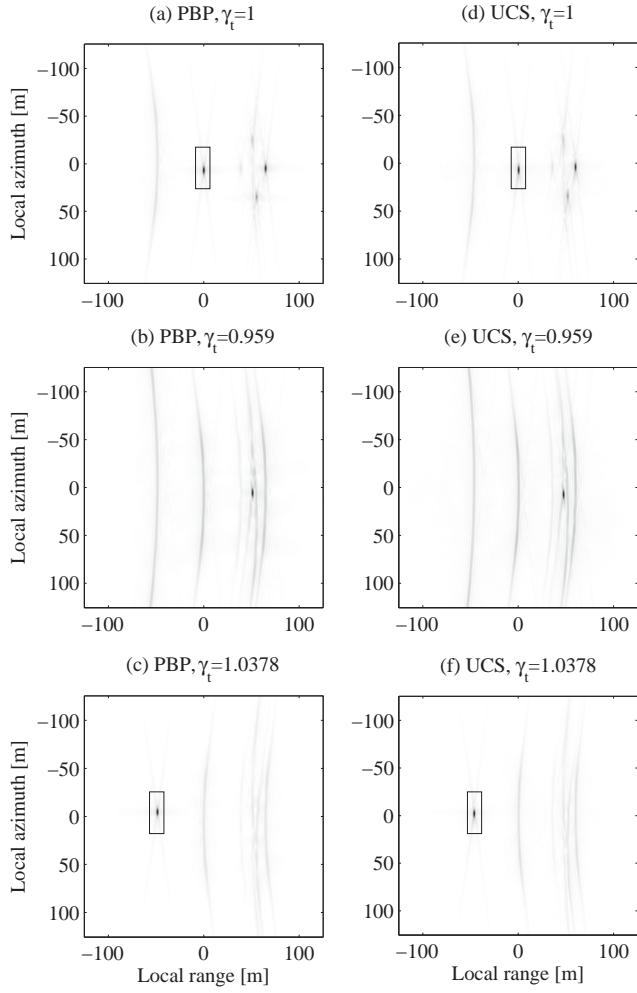


Figure 2: SAR images of the simulated stationary and moving targets processed by PBP and UCS. The integration angle $\theta = 15^\circ$ is chosen arbitrarily. In the SAR scene, the moving target with $\gamma_t = 1.0378$, which appears on the left hand side of the SAR images, has RCS of $\sigma = 1$ and the one with $\gamma_t = 0.959$ on the right hand side $\sigma = 0.25$. There are one stationary target with $\sigma = 1$ in the middle of SAR images and four other stationary targets on the right hand side with $\sigma = 0.25, 0.5, 0.75$ and 1 surrounding the moving target $\gamma_t = 0.959$. The black rectangles mark the areas of detection (containing the moving target $\gamma_t = 1.0378$ and $\sigma = 1$) and the areas of reference (containing the stationary target and $\sigma = 1$) which are used for evaluation purposes. Other targets are used mainly for moving target detection illustration. (a) Original SAR image processed by PBP. (b) SAR image processed by PBP with $\gamma_t = 0.959$. (c) SAR image processed by PBP with $\gamma_t = 1.0378$. (d) Part of original SAR image processed by UCS. (e) Part of SAR image processed by UCS with $\gamma_t = 0.959$. (f) Part of SAR image processed by UCS with $\gamma_t = 1.0378$.

seen clearly. Similar effects can be seen in the SAR images in Fig. 2.c and 2.f after applying the focusing approach using another known NRS $\gamma_t = 1.0378$. The superposition of the hyperbolic curves caused by the defocusing of the stationary targets as well as the moving target can result in higher energy concentration in some image pixels.

5 Detection of Moving Targets by Focusing

As illustrated a moving object can be focused to its original shape in the SAR image by simply processing SAR data with NRS, i.e scaling the platform speed with NRS, while any stationary objects are instead defocused. However, this focusing approach can only be carried out if motion parameters of the moving object, e.g. speed and motion direction, are known. In reality, these parameters are not usually known and therefore require complex estimation procedures if they are to be retrieved. These procedures can be applied if, and only if, the presence of a moving object is indicated; in other words, the moving object must be detected first before applying estimation procedures.

For detection, different blind hypotheses γ_p , so-called NRS under test, must be tested on either (23) or (24) and (29) until the optimum moving target focusing for detection is reached. In this paper, the subscript p is used to denote the processed variables. The energy reflected from moving objects as well as stationary objects at each hypothesis γ_p is therefore either concentrated or dispersed. If there is a moving object with γ_t , at the hypothesis $\gamma_p \approx \gamma_t$, the energy reflected from the moving object is highly concentrated and the energy reflected from the stationary objects is dispersed due to the smearing.

The subsequent problem is then how to adapt the value of γ_p between the tests. In other words, how large should the step size be between different blind hypotheses in the detection scheme? A trade-off between the probability of detection and the computational cost must be taken into account. The highest probability of detection can be obtained for the smallest step size. However, depending on the false alarm rate, different step sizes may be used.

5.1 Optimum Step Size of NRS for Detection

An optimum quantization step size $\Delta\gamma$ for detection is proposed in [17]. The derivation of the step size is based on the decrease of the SAR image intensity of a point target given by the GBP integral [22]. This decrease can be

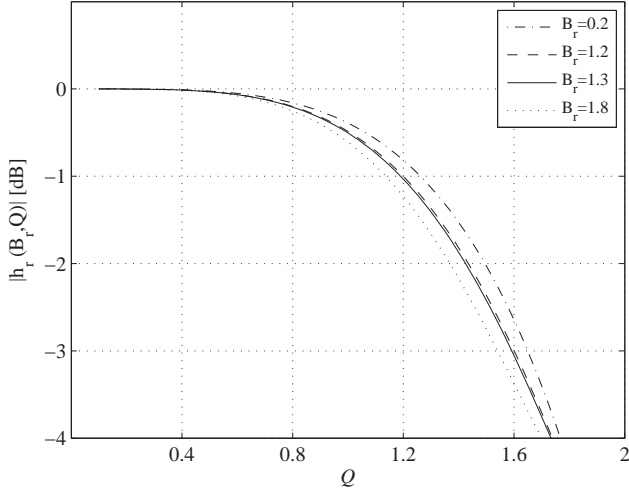


Figure 3: The absolute values of $|h_r(\gamma_p, t_0)|$ as a function of the fractional bandwidth B_r (PAMIR: $B_r \approx 0.2$, LORA and P-3: $B_r \approx 1.2$, CARABAS-II: $B_r \approx 1.3$, and BoomSAR: $B_r \approx 1.8$) and Q .

estimated by the ratio

$$h_r(\gamma_p, t_0) = \frac{\int_{-\infty}^{+\infty} g\left(t, \sqrt{\gamma_p^2 \cdot [v_{plt}t - x_p(t_0)]^2 + r_p^2(t_0)}\right) dt}{\int_{-\infty}^{+\infty} g\left(t, \sqrt{\gamma_t^2 \cdot [v_{plt}t - x_0]^2 + r_0^2}\right) dt} \quad (30)$$

where $g(t, r)$ is the band limited radar pulse after range compression. Hence, the denominator of the ratio (30) defines the peak intensity of a point target, i.e. $\gamma_p = \gamma_t$. The numerator determines the intensity of a point target corresponding to a blind hypothesis γ_p . An incorrect hypothesis smears the point target into the shape of an ellipse or a hyperbola and thereby causes a reduction of the ratio (30).

If we assume that a chirp signal is transmitted, Fig. 3 shows the absolute values of the integral (30) as a function of the fractional bandwidth B_r and

the scalar variable Q

$$Q = v_{pl} t_i \sqrt{\frac{\pi f_c |\gamma_p^2 - \gamma_t^2|}{2 c r_0}} \quad (31)$$

where t_i is the integration time. With the parameters given in Table 1, the CARABAS-II fractional bandwidth is estimated about 1.3. Assuming that the maximum acceptable ratio $|h_r(\gamma_p, t_0)|$ is given by h_{lim} , then the condition for $\Delta\gamma$ can then be found using the following inequality

$$\left| h_r \left(\gamma_t \pm \frac{\Delta\gamma}{2}, t_0 \right) \right| \leq h_{lim}. \quad (32)$$

A threshold h_{lim} should be set as desired to meet the demand of the acceptable detection failure. With the threshold h_{lim} , the optimum discretization step can be approximated by

$$\Delta\gamma \approx \frac{Q^2 c r_0}{2 \pi f_c \gamma_t v_{pl}^2 t_i^2}. \quad (33)$$

Equation (33) is derived for short apertures. However, it is shown in [17] that this approximate solution can also be applied to long apertures with a discretization step error of less than 10%, i.e. the discretization step derived with the approximation of short apertures (33) is always smaller than the discretization step for long apertures. The range of NRS being tested can be derived from another form of (14) as

$$\gamma_t = \sqrt{\left(\frac{v_{tg}}{v_{pl}} \right)^2 - 2 \left(\frac{v_{tg}}{v_{pl}} \right) \cos\varphi + 1} \quad (34)$$

where φ is the moving direction of the object. The minimum and maximum values of γ_t correspond to moving directions of 0° and 180°, respectively

$$\gamma_{t,min} = 1 - \max \left\{ \frac{v_{tg}}{v_{pl}} \right\} \quad (35)$$

$$\gamma_{t,max} = 1 + \max \left\{ \frac{v_{tg}}{v_{pl}} \right\}. \quad (36)$$

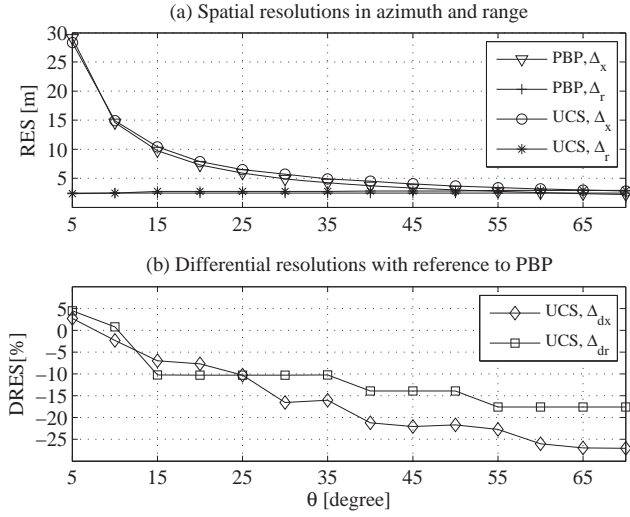


Figure 4: (a) Spatial resolutions in azimuth Δ_x and range Δ_x (RES) obtained by PBP and UCS at different integration angles. (b) UCS differential resolution (DRES) with reference to PBP.

5.2 Procedures and Practical Considerations for Detection

The procedure to perform the moving target detection by focusing technique in this paper can be listed as follows:

- Processing data with different hypotheses in SAR image formation (using either (23) or (24) and (29)).
- Examining image pixels after the data processing.
- Detecting the presence of moving objects based on intensity.

Some practical issues should also be considered in the tests. For example, it may not be necessary and efficient to use the complete aperture for detection. The assumption of no acceleration in Section 3 is also more likely to hold with small integration times associated with small integration angles. Image pixel spacing is another practice issue since it affects the number of the tested

hypotheses and therefore the processing time. We propose to use the spatial resolutions, i.e. -3 dB widths, in azimuth and range for the image pixel spacing in the detection stage. Fig. 4.a shows measurement results on spatial resolutions (RES) obtained by PBP and UCS at different integration angles using the simulated data. The azimuth and range resolutions can also be approximately estimated by [34]

$$\Delta_x \approx \frac{c}{2f_c\theta} \quad (37)$$

$$\Delta_r \approx \frac{c}{2B} \quad (38)$$

respectively, where θ is the processed integration angle and B is the signal bandwidth.

5.3 Moving Target Detection Tests on the Simulated Data

In this paper, SAR images are represented in local azimuth and local range coordinates. The formats (azimuth 1: azimuth 2, range 1: range 2), (azimuth, range) and azimuth \times range are used to locate an area, a position and the dimension of an area, respectively.

Moving target detection tests in this section use the same simulated SAR data in Section 4. The tests follows the detection procedures given in Section 5.2. An arbitrary integration angle, e.g. $\theta = 15^\circ$, is selected for the tests. The corresponding image pixel spacing which can be found from Fig. 4.a, should be $10\text{m} \times 2.5\text{m}$. Different blind hypotheses γ_p are tested on the whole imaged SAR scene in Fig. 2.a, i.e. $250\text{m} \times 250\text{m}$. Depending on the expected detection ability, different optimum discretization step sizes can be found based on (33). In general, we can decide on an optimum quantization step size corresponding to the threshold $h_{lim} = -3$ dB, i.e. giving a maximum loss of 3 dB from the peak intensity. With such threshold, (33) results in the optimum discretization step size $\Delta\gamma \approx 0.005$. The range of hypotheses γ_p can be estimated by (35) and (36). It is assumed that a slow moving point target is the subject to be detected. The maximum speed of the simulated target is 12.8 m/s and the moving direction is not known. Equations (35) and (36) result in a range of different blind hypotheses $\gamma_p \in [0.9, 1.1]$.

In the first test in this section, the SAR data is processed by PBP with the image pixel spacing of $10\text{m} \times 2.5\text{m}$. Fig. 5 shows the measured normalized intensities of the image pixels belonging to the tested area at the hypothesis

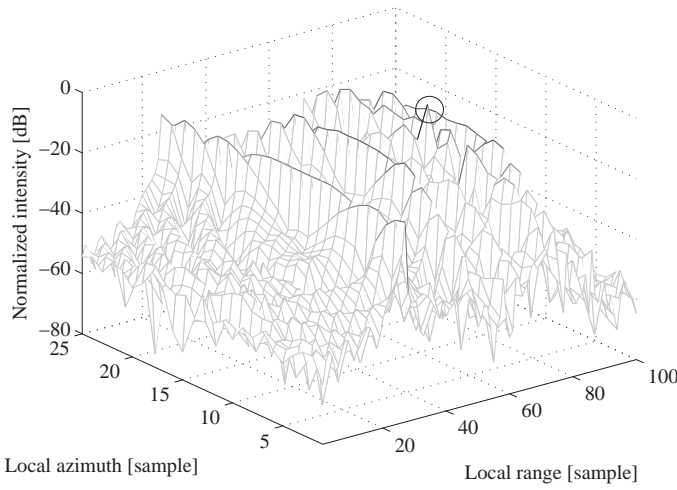


Figure 5: The measured normalized intensities on 2500 image pixels $10\text{m} \times 2.5\text{m}$ belonging to the tested area $250\text{m} \times 250\text{m}$ processed by PBP at the hypothesis $\gamma_p = 0.96$. The black circle denote the peak value of normalized intensities at this hypothesis. The peak corresponds to the moving target with $\sigma = 0.25$.

$\gamma_p = 0.96$. The number of image pixels within this area is $N_{pixel} = 2500$. The behavior of the normalized intensities belonging to the tested area at all hypotheses γ_p can be investigated by mapping them in a 2D plot. Fig. 6 shows the relationship between the NRS being tested and the normalized intensities. The peak values of the normalized intensities are retrieved at the hypotheses $\gamma_p = 0.96$ and $\gamma_p = 1.04$ indicating the highest possibility of the presence of the two simulated moving targets. Another is retrieved at the hypothesis $\gamma_p = 1$ indicating the presence of the simulated stationary target. The detection of the moving target with $\text{NRS} \approx 0.96$ indicates that the moving target detection by focusing technique facilitates detecting weak moving targets which are obscured by strong surrounding stationary targets.

For UCS, we must perform blind tests γ_p on a area whose dimensions are defined by the number of aperture positions and the number of range data.

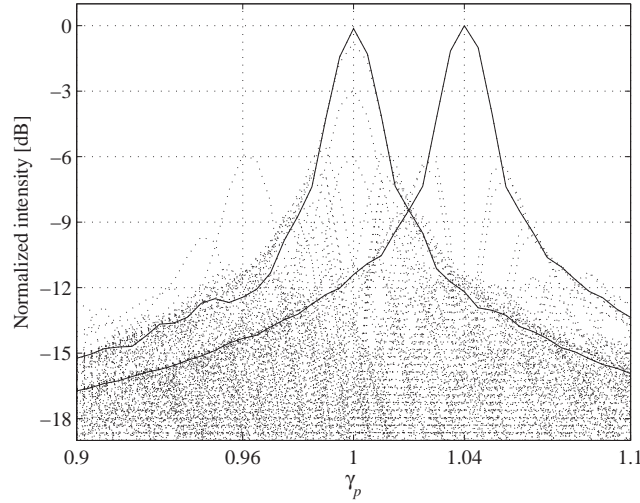


Figure 6: The measured normalized intensities on 2500 image pixels $10\text{m} \times 2.5\text{m}$ belonging to the tested area $250\text{m} \times 250\text{m}$ processed by PBP with different γ_p . The solid black plots denote the peaks of the targets with $\sigma = 1$, the peak -6 dB at $\gamma_p = 0.96$ corresponds to the moving target with $\sigma = 0.25$.

The data belonging to the areas of interest is then extracted. The image pixel spacing is fixed and depends on the distance between two adjacent aperture positions, i.e. the ratio of the platform speed v_{pl} to PRF, and the range sampling frequency. With the parameters given in the Table 1, the image pixel spacing in azimuth is estimated to be 0.9375 m. The range sampling frequency 160 MHz results in the image pixel in range of 0.9375 m. For the same tested area $250\text{m} \times 250\text{m}$ which is a part of the SAR image processed by UCS, the number of image pixels raises to $N_{pixel} = 71289$. Fig. 7 shows the plot of the measured normalized intensities in the tested area with respect to NRS under test.

The plot shows that there seems to be more than one moving target with $\text{NRS} \approx 0.96$ and more than one moving target with $\text{NRS} \approx 1.04$. However, all normalized intensities around the $\text{NRS} \approx 0.96$ or $\text{NRS} \approx 1.04$ belong to adjacent image pixels and are smeared from a single moving target. Such effect is caused by the small image pixel spacing. If the tested area is downsampled

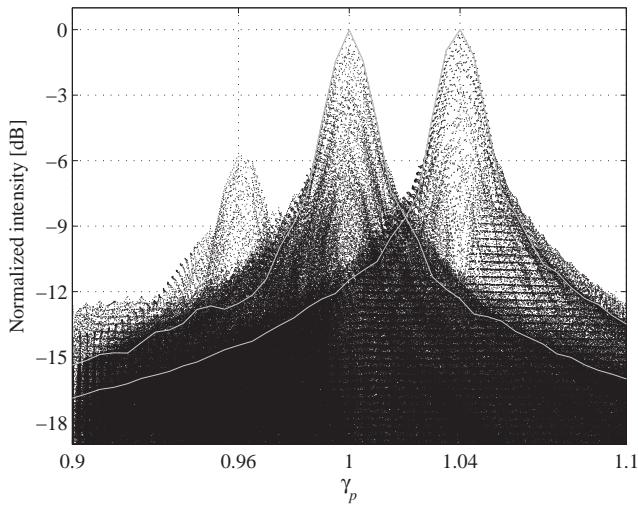


Figure 7: The measured normalized intensities on 71289 image pixels $0.9375\text{m} \times 0.9375\text{m}$ belonging to the tested area $250\text{m} \times 250\text{m}$ processed by UCS with different γ_p . The solid gray plots denote the peaks of the targets with $\sigma = 1$, the peaks -6 dB at $\gamma_p = 0.96$ correspond to the moving target with $\sigma = 0.25$.

with factors of about 10 in azimuth and 3 in range, the number of image pixels belonging to the tested area is reduced to $N_{pixel} = 2500$. A similar detection of moving targets with $\text{NRS} \approx 0.96$ and $\text{NRS} \approx 1.04$ is then achieved with UCS.

5.4 Evaluation of the Moving Target Detection by Focusing Technique

The moving target detection by focusing technique can be evaluated by terms of ability of detection and processing time for the detection. The ability of detection can be based on the improvement in signal-to-clutter noise ratio (SCNR). If we define the area of detection and the area of reference by a focused moving target and a stationary point target, respectively, surrounded by low backscattering areas, the evaluation using the improvement in SCNR

is introduced in [20] as follows:

$$G_{SCNR} = 20\log\left(\frac{\mu_2}{\mu_1}\right) - 20\log\left(\frac{\nu_2}{\nu_1}\right) \quad (39)$$

where μ_1 and μ_2 are the retrieved peak intensities in the area of detection before and after focusing, respectively. Similarly, ν_1 and ν_2 are the peak intensities in the area of reference. Both areas of detection and reference in this simulation can be chosen relatively small. For PBP, we need only to process these small areas with different hypotheses γ_p on γ_t . For UCS, we must process the whole SAR image and search for the peak intensities on these smaller areas.

At hypothesis $\gamma_p = 1.04$, the energy reflected from the moving target with $NRS \approx 1.04$ is highly focused while the energy reflected from the stationary target is dispersed. The area of detection in this test is marked by black rectangles as shown in Fig. 2.b and 2.e. Black rectangles in Fig. 2.a and 2.d delineate the area of reference containing the stationary point target in the center of the SAR image. In this simulation, we can find μ_1 , μ_2 , ϵ_1 and ϵ_2 values by extracting information in the detection stage (solid black plots in Fig. 6 and solid gray plots in Fig. 7). The improvement in SCNR given by (39) can be visually estimated as $G_{SCNR} \approx 20$ dB for both PBP and UCS as the result of 10 dB concentration of the moving target's energy as well as -10 dB dispersion of the point target's energy. This improvement depends both on the radar system and on the velocity of the moving target. With such an improvement, this technique even accommodates detecting moving objects surrounded by a considerable number of stationary targets.

The processing time for the detection is related to the computational cost. For PBP, the processing time is also affected by the subaperture length. As mentioned in Section 4.1, the focusing approach can be performed on either the polar image formation or the slant-range image formation using γ_t . Both proposals give advantages of processing time compared to GBP. If N_h is the number of hypotheses, N_a is the number of aperture positions corresponding to the integration angle handling the detection, N_x and N_r are the dimensions of the tested area, the optimum numbers of aperture positions to form subapertures are given by

$$N_s = \sqrt{N_x} \quad (40)$$

for the former proposal and

$$N_s = \sqrt{N_h \times N_x} \quad (41)$$

Table 2: Numbers of operations for detection required by PBP and UCS.

Algorithm	Number of operations
PBP on polar	$2 \times N_h \times N_a \times N_r \times (1 + \sqrt{N_x})$
PBP on slant-range	$2 \times N_a \times N_r \times (1 + \sqrt{N_h \times N_x})$
UCS	$N_h \times N_a \times N_d \times [3 \times \log_2 (N_a \times N_d) + 4]$

for the latter one. The optimum numbers of operations for detection are summarized in Table 2. It is obvious that the latter proposal even runs approximately $\sqrt{N_h}$ times faster than the former one.

UCS always processes a matrix of size $N_a \times N_d$ for each hypothesis γ_p where N_d is the number of range data. Since the number of range data is very large, such processing requires huge memory. In the case where the requirement of memory is fulfilled, the technique embedded UCS runs much faster than GBP. The number of operations for detection required by UCS is also given in Table 2.

5.5 A Possibility to Use the Moving Target Detection by Focusing Technique for Estimation

As soon as the moving target is detected, an appropriate method can be used to estimate such parameters as speed, moving direction, and dimension of the moving object. One of the NRS estimation methods, which is proposed in [35], works in an iterative way and is based on a chirp rate estimator in azimuth direction of the SAR image. The investigation in [20] demonstrated that the technique not only facilitates detecting moving objects but also estimating motion parameters such as NRS. Hence, a better estimate of NRS can be achieved by testing different hypotheses γ_p with smaller steps close to the retrieved peak intensity. Using the same integration angle for the detection stage, a new step size for estimation $\Delta\gamma_e$ can be retrieved by (33) with a more strict threshold h_{lim} . However, there are also other ways to find a step size for estimation $\Delta\gamma_e$, for example, the one proposed in [36] from the speed estimation's point of view. Using PBP, the extra computational cost for the

NRS estimate with a smaller step size carried out by (24) is

$$N_{h,e} \times N_{a,e} \times \frac{N_x \times N_r}{N_s} \quad (42)$$

where $N_{h,e}$ is the number of hypotheses in the estimation stage and $N_{a,e}$ is the number of aperture positions used in the estimation stage. The estimation step can be performed on extremely small areas since small displacement caused by directional reflection has been compensated in the detection stage. Using PBP, the computational cost for this extra step is small enough to be insignificant. Estimations regarding acceleration or moving direction are possible if we test different hypotheses γ_p with a smaller step and different integration angles. These aspects are not, however, presented in detail in this paper.

5.6 A Comparison between PBP and UCS with Regard to the Moving Target Detection by Focusing Technique

Fig. 4.a shows measurement results on spatial resolution (RES), considered to be the most significant parameter for image quality measurements when evaluating quantitatively the performance of the PBP and UCS algorithms where no motion error is assumed. With regard to the detection ability, RES is related to the retrieved peak intensity, the optimum quantization step and the image pixel spacing for detection. The measurements should also be performed at different integration angles since different azimuth focusing obtained at different integration angles results in different spatial resolution in azimuth in UWB SAR [37]. To facilitate the comparison between PBP and UCS in terms of spatial resolution, we use the differential resolution terms (DRES) which are introduced in [37]. The references for these measurements are given by PBP spatial resolutions. The measured results are plotted in Fig. 4.b. The DRES measurement results indicate that if there is no motion error, UCS can obtain approximately the same spatial resolutions in azimuth and range as PBP at small integration angles (up to 15°). These resolutions in both azimuth and range are up to 25% and 15% lower than PBP at larger integration angles, respectively. Although there is no motion error introduced, the ability of UCS to image objects distinctly and separately on a SAR image is inferior to that of PBP at large integration angles. The moving target detection by focusing technique is associated with a large integration angle

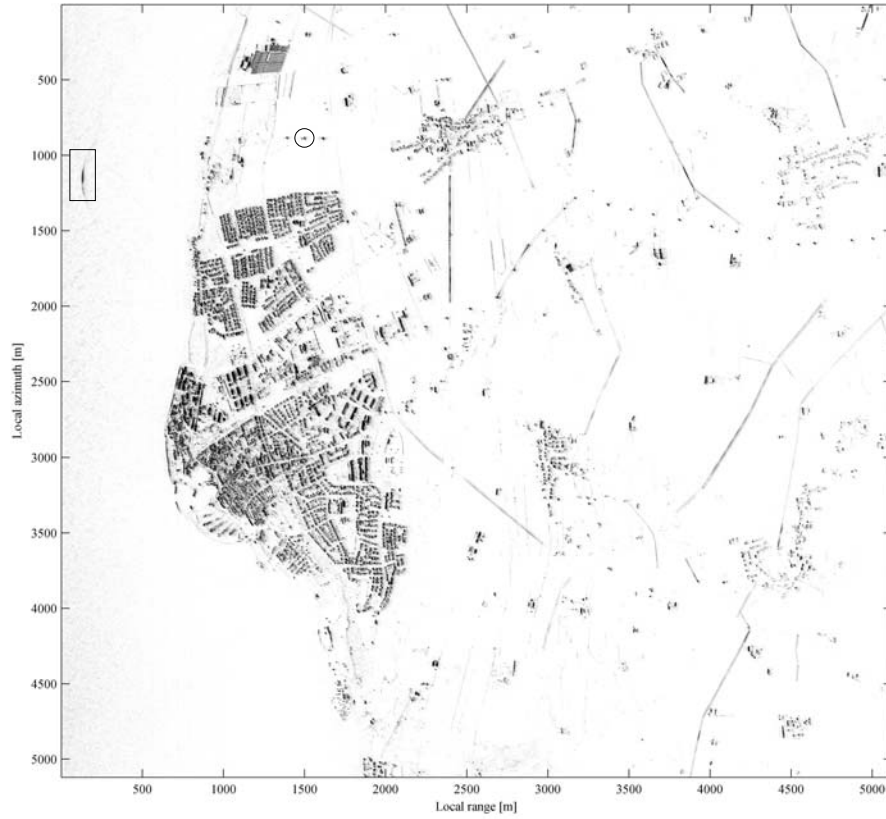


Figure 8: Ground scene in the area of Simrishamn, located along the Baltic coastline in southern Sweden, is imaged by CARABAS-II with parameters given in Table 1. The image is processed by the complete aperture which refers to an integration angle of about 110° with respect to the aim point. The area surrounding a hyperbolic curve visible in a SAR image, where the presence of a moving target is predicted, is delineated by a black rectangle. A pointlike scatterer, which is marked by a black circle, is used to observe the effects of the focusing approach to the SAR image.

and must handle azimuth focusing for reliable detection. In such cases, PBP has advantages over UCS. Due to the approximations still existing in UCS as

well as NCS, the ability to image weak reflective targets affected by a strong reflective target nearby of these algorithms in UWB SAR is restricted. This is demonstrated by the measured results of integrated sidelobe ratio (ISLR) and peak sidelobe ratio (PSLR) given in [32]. In reality, there are always motion errors caused by any airborne SAR system and these motion errors need to be compensated. However, there may not be a manageable motion compensation method for UCS as for time-domain algorithms [38].

As also shown in [32], the computational cost for NCS accelerate with the increase of the integration angle. This also holds for UCS. For UWB SAR processing in general and moving target detection in UWB SAR in particular, some extra computational costs must be counted for UCS such as elimination of higher order phase (HOP) terms in the Taylor expansion (from fourth order for NCS and fifth order for UCS) and motion error compensation.

As shown in the tests in Section 5.3, using PBP in the detection of moving target by focusing technique has the advantage of the flexible tested area thanks to PBP's local processing characteristics. In addition, the image pixel spacing can be set as desired. For UCS, the hypotheses must be tested on a larger area since its dimensions are decided by the considered number of aperture positions and the number of range data. The image pixel spacing is also limited by the required PRF and the range sampling frequency.

A comparison in terms of processing time related to the computational cost for the detection may be difficult to present in an analytical way due to the different matrix sizes to be processed. However, in our tests with simulated data, the detection embedded UCS has no advantage in terms of processing time over PBP.

For these reasons, experiments on the real CARABAS-II data in the following sections are focused on the detection embedded PBP. With an appropriate selection of processing parameters and an appropriate method for embedding PBP in the moving target detection by focusing technique, this technique can be carried out efficiently both in terms of image quality for detection and processing time.

6 The First Experiment on Real Data

In the first experiment on real data, we used CARABAS-II SAR data collected in the area of Simrishamn, located along the Baltic coastline in southern Sweden. The latitude and longitude of the aim point are 55.5° N and 14.3° E, respectively. The parameters for the registration are given in Table 1 and

have also been used to generate the simulated data in Sections 4 and 5. The imaged ground scene is shown in Fig. 8.

Using PBP, the SAR image in Fig. 8 is formed by a complete aperture of 20480 positions, equally spaced 0.9375 m. The dimensions are 5120 m \times 5120 m with 1 m sampling in each direction. With such dimensions, an optimum subaperture size in PBP of 72 aperture positions is retrieved by (41) with $N_h = 1$. With the available data, a selection of the tested area can be the full SAR scene 5120m \times 5120m. However, due to illustration purposes, we select an area 400m \times 100m surrounding (1159, 128) marked by a black rectangle in Fig. 8. In this area, moving targets can be detected as well as imaged easily. An arbitrary integration angle $\theta = 15^\circ$ is considered for handling the detection. Equations (37) and (38) result in 10m \times 2.5m as the image pixel spacing. The number of image pixels belonging to the tested area is therefore $N_{pixel} = 1600$. Since the selected area belongs to the territorial waters in Simrishamn, moving objects can be a boat, a ferry-boat or a ship. The speed of such vessels may be up to 50 km/h or 14 m/s. The NRS range is set approximately from 0.9 to 1.1 based on (35) and (36). Using the parameters given in Table 1, an optimum quantization step size $\Delta\gamma = 7.5 \cdot 10^{-3}$ is retrieved by (33) based on the threshold $h_{lim} = -3$ dB and $Q = 1.6$. The number of hypotheses γ_p needed for detection is therefore $N_h = 27$. Fig. 9 shows the normalized intensities of the image pixels processed with different hypotheses γ_p .

Measurement results on the normalized intensities indicate the presence of a moving targets with $NRS \approx 0.96$ in the tested area. The three peaks shown in Fig. 9 belong to three adjacent image pixels and should therefore be associated to one single moving target. The difference in NRS may be explained by waves in the territorial waters in Simrishamn at time of data collection. The strong waves cause roll of the vessel which change its velocity during the integration time. This affects severely the detection ability.

Fig. 10 shows the same imaged scene as in Fig. 8 but processed with $\gamma_p = 0.96$. Some effects on the new formed SAR image can be seen directly. The elliptic curve in the selected area marked by the black rectangle is now focused on a small bright spot in Fig. 10. This again confirms the presence of only one vessel in the tested area. Meanwhile, pointlike scatters, e.g. the one marked by the black circle, either smear as elliptic curves or disappear since the reflected energy may drop below the clutter noise level as a result of this dispersion. The effects on the SAR image can be explained as follows. The stationary objects on the ground can now be defocused in the moving frame processed at $\gamma_p = 0.96$ (smearing as elliptic curves). All moving objects surrounding $\gamma_p = 0.96$ are focused to original shape. However, large stationary

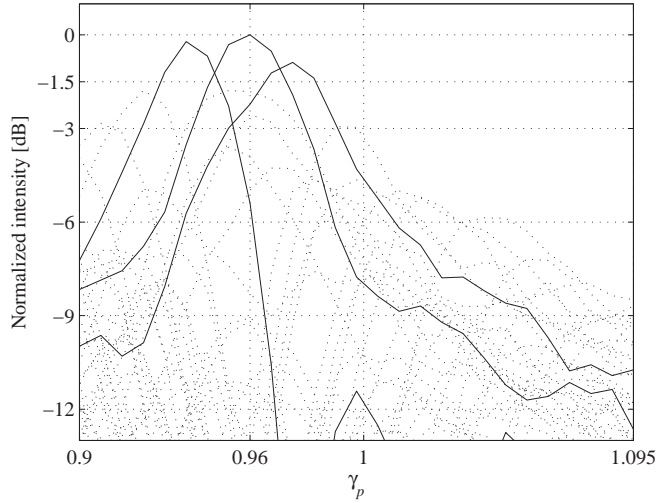


Figure 9: The measured normalized intensities on 1600 image pixels $10\text{m} \times 2.5\text{m}$ belonging to the tested area $400\text{m} \times 100\text{m}$ processed by PBP with different γ_p . Optimum quantization step size for detection $\Delta\gamma = 7.5 \cdot 10^{-3}$, integration angle $\theta = 15^\circ$, minimum range $r_0 \approx 4700 \text{ m}$. The solid black plots denote the peak values of normalized intensities.

objects such as power lines are not affected by the focusing approach due to strong specular reflection, i.e. non-pointlike scatters.

A SAR image of the detected moving object is also shown as contour plots at levels -3 dB , -6 dB , -9 dB , -15 dB and -21 dB in the lower right corner of Fig. 10. The 3 dB width of the target is estimated to be about $7 \text{ m} \times 3 \text{ m}$. This is a quite good result since it is close to what one would expect for an extended boat, ferry-boat or ship.

Since the moving object in this experiment is a strong scatter in a low backscattering environment, it can be visually detected at all of the proposed NRS. However, as shown in Fig 9, the concentration of the moving target's energy at $\gamma_p = 0.96$ is only 3 dB higher than at $\gamma_p = 1$. If the moving target was not in the territorial waters and surrounded by a number of the very strong non-pointlike scatters, the possibility to detect this moving target would be low. This specific experiment shows that, applying this technique to single-

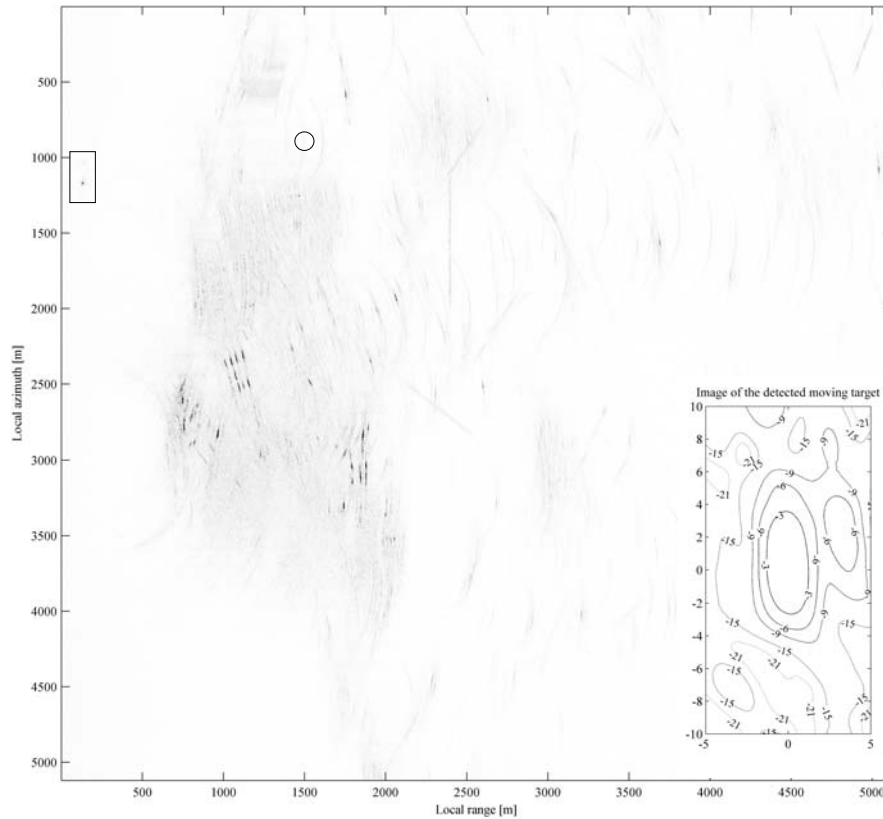


Figure 10: Same imaged scene as in Fig. 8 but processed with $\gamma_p = 0.96$. The image is also processed by an integration angle of about 110° with respect to the aim point. The hyperbolic curve in the selected area marked by the black rectangle is now focused on a small bright spot. The pointlike scatterer marked by the black circle smears as an elliptic curve.

channel and using it directly to detect moving targets at small integration angles is suboptimal in urban areas with many strong non-pointlike scatterers. In this case, a large integration angle is required to get a better improvement in SCNR for detection. Another experimental result on the data collected in the Simrishamn scene is presented in [20]. The improvement in SCNR is also

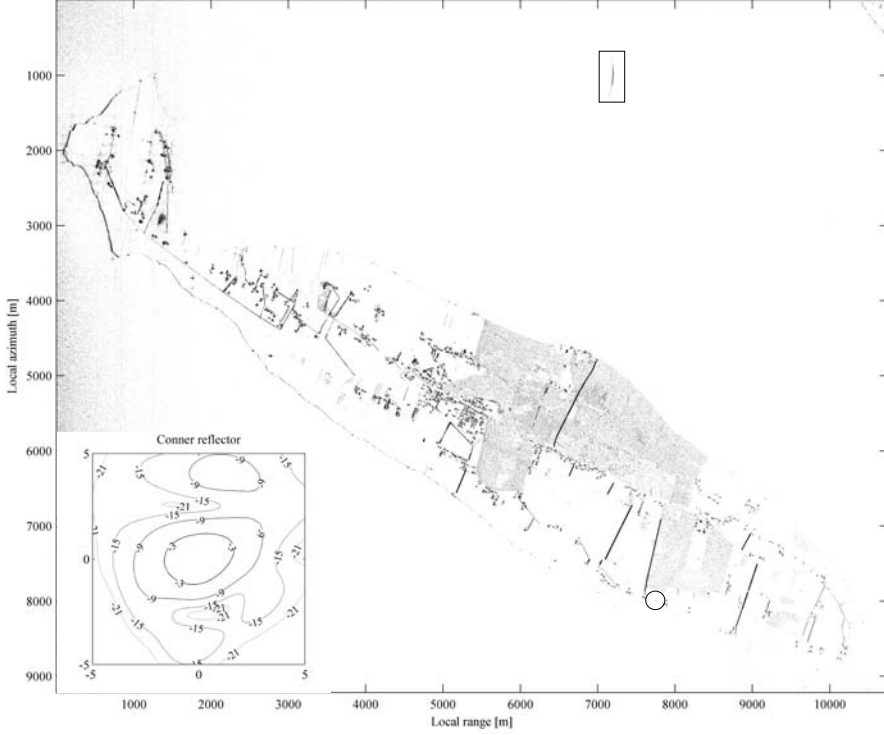


Figure 11: Ground scene of the island Visingsö, located in the fresh water lake Vättern in southern Sweden, is imaged by CARABAS-II with the parameters given in Table 3. The image is processed by the complete aperture which refers to an integration angle of about 110° with respect to the aim point. The area surrounding a elliptic curve visible in a SAR image, where the presence of a moving target is predicted, is delineated by a black rectangle. A corner reflector, which appears as a point target in the SAR image and is marked by a black circle, is used to observe the effects of the focusing approach to the SAR image as well as evaluate the performance of the detection.

about 18 dB, however at an integration angle $\theta \approx 110^\circ$, i.e. the complete aperture. However, using the complete aperture is synonymous with long processing time and may violate seriously the assumptions of linear movements with constant speeds. An alternative is to combine the moving target

detection by focusing technique with multi-channel techniques, e.g. DPCA and STAP, to suppress the surrounding non-pointlike scatters [30, 39]. The improvement in SCNR obtained with the moving target detection by focusing technique will still be preserved when combining with the multi-channel techniques.

7 The Second Experiment on Real Data

In the second experiment on real data, we use CARABAS-II SAR data collected in a field campaign at the northern part of the island Väringö, located in the fresh water lake Vättern in southern Sweden. The latitude and longitude of the aim point are 58.0° N and 14.4° E, respectively. The parameters used in the data collection are summarized in Table 3.

The imaged SAR scene processed with complete aperture is shown in Fig. 11. Dimensions of the SAR image are 9210×10752 pixels at $1 \text{ m} \times 1 \text{ m}$ pixel spacing. Equation (41) results in an optimum subaperture size of 104 aperture positions, equally spaced 0.9375 m. In this experiment, we concentrate on evaluating the gain in detection ability.

The moving object considered in this experiment is known. It is the EBBA BRAHE ferry operating in the lake Vättern. The dimensions of the ferry are $40 \text{ m} \times 17 \text{ m}$. At the time when the data were collected, the ferry was moving toward the island at a speed of $v_{tg} \approx 10$ knots or $v_{tg} \approx 5.14 \text{ m/s}$. The moving direction of the ferry is $\varphi \approx 180^{\circ}$ with respect to the platform velocity. Equation (34) results in an approximate true NRS $\gamma_t = 1.04$. During this SAR data collection campaign, corner reflectors for system calibration located at different areas with low scattering background were deployed. Corner reflectors appear as point targets in a SAR image. They can therefore be seen as reference point targets and used to evaluate the gain in detection ability using (39).

7.1 Moving Target Detection by Focusing Experiment

The EBBA BRAHE ferry appears in the SAR image as an elliptic curve in the area surrounding (962, 7196) as shown in Fig. 11. The tested area is in this case $400\text{m} \times 100\text{m}$ and marked by a black rectangle in Fig. 11. With the similar image pixel spacing of $10\text{m} \times 2.5\text{m}$, the number of image pixels is the same as the number used in the first experiment, i.e. $N_{pixel} = 1600$.

Table 3: The parameters used in the measurement campaign in Visingsö.

Parameter	Value
The highest frequency processed	82 MHz
The lowest frequency processed	22 MHz
Platform speed v_{pl}	126 m/s
Full aperture length	33600 m
Full aperture positions	35840
Flight altitude	4943 m
Minimum range to the aim point	11250 m
PRF	134 Hz

The speed of the ferry is limited by 50 km/h or 14 m/s. With given speed of the aircraft, different hypotheses γ_p are tested on the selected area in the interval 0.85 to 1.15 derived by (35) and (36). If the integration angle $\theta = 15^\circ$ is selected for detection, an optimum quantization step size $\Delta\gamma = 3 \cdot 10^{-3}$ can be estimated using (33) based on the threshold $h_{lim} = -3$ dB and $Q = 1.6$. The number of hypotheses γ_p needed for detection is therefore $N_h = 101$.

As shown in Fig. 12, the EBBA BRAHE ferry moving with an NRS ≈ 1.036 in the tested area is detected. Since the EBBA BRAHE ferry is not strongly affected by the waves while moving in the fresh water lake Vättern, it gets more focused compared to the vessel in the first experiment. Fig. 13 shows the same imaged scene as given in 11 but processed with $\gamma_p = 1.036$, where the moving target has the highest possibility of detection.

Processing data with NRS = 1.036 causes some effects which can be seen directly in Fig. 13. The curve found earlier in the selected area (marked by the black rectangle) is now focused on a small bright spot. Meanwhile, the corner reflector in the area of reference disappears (marked by a black circle in Fig. 11) since the energy reflected from the reflector is dispersed and drops below the clutter noise level as a result of about -10 dB energy loss at $\gamma_p = 1.036$. Similar to the first experiment, large stationary objects, in this case fences, are also not affected by defocusing.

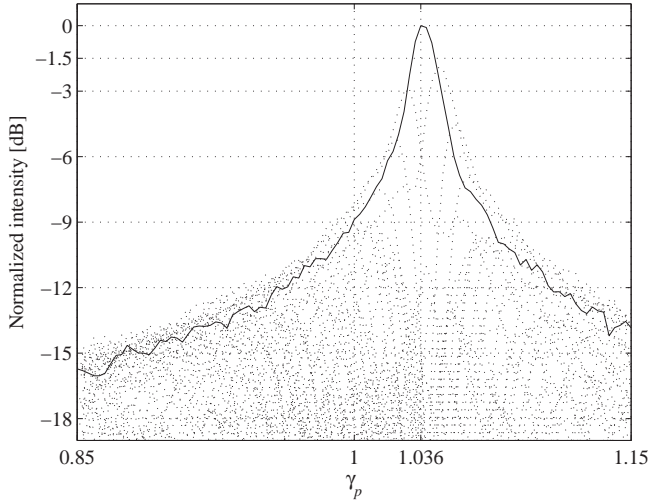


Figure 12: The measured normalized intensities on 1600 image pixels $10\text{m} \times 2.5\text{m}$ belonging to the tested area $400\text{m} \times 100\text{m}$ processed by PBP with different γ_p . Optimum quantization step $\Delta\gamma = 3 \cdot 10^{-3}$, integration angle $\theta = 15^\circ$, minimum range to the object $r_0 \approx 7600$ m. The solid black plot denotes the peak value of normalized intensities.

7.2 Evaluation of the Detection Ability

To evaluate the detection ability using (39), an area $50\text{m} \times 12.5\text{m}$ surrounding the focused EBBA BRAHE is selected to be the area of detection. As mentioned, some corner reflectors were deployed to calibrate the CARABAS-II system during this data collection campaign. One of them is located at (7982, 7751) in the local azimuth and range coordinates and is marked by a black circle in Fig. 11. Its contour plots at levels -3 dB, -6 dB, -9 dB, -15 dB and -21 dB is in the lower left corner of Fig. 11. This reflector appears in the SAR image as a point target and can be used for evaluation purposes. The area surrounding the corner reflector defines the area of reference.

As mentioned, the area can be affected by surrounding objects when the focusing approach is applied. The area of reference should thus be small enough to avoid the smearing of other objects which may cause inexact mea-

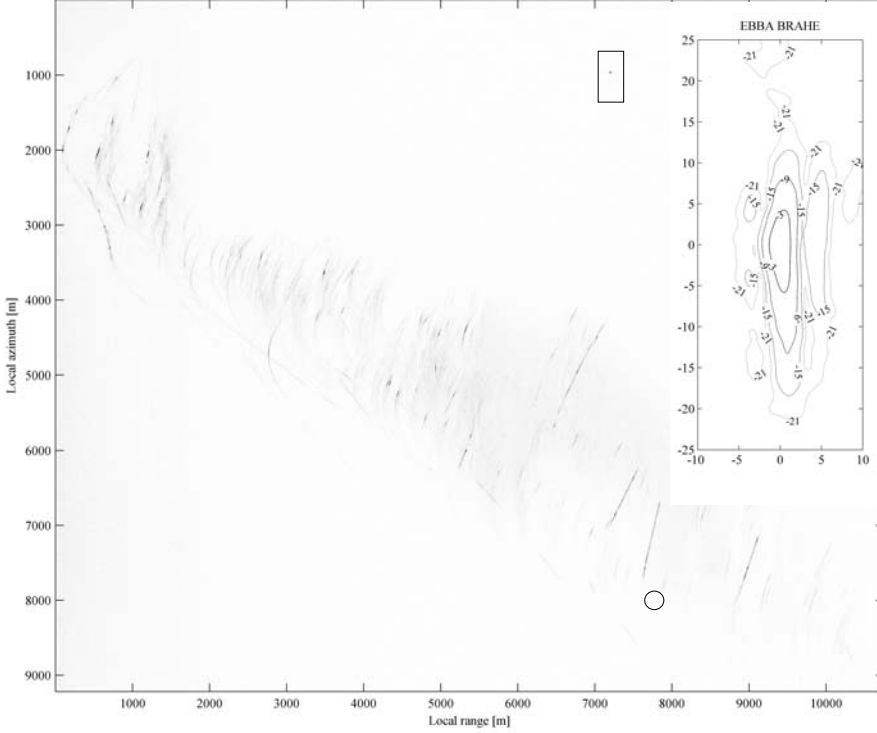


Figure 13: Same area as in Fig. 11 but processed with $\gamma_p = 1.036$. The image is also processed by an integration angle of about 110° with respect to the aim point. Similar effects, which have been seen in Fig. 10, are again shown in this image. However, the corner reflector in the area of reference, marked by a black circle, disappears due to the energy dispersion.

surements. The dimensions of the area of reference are therefore selected by $30\text{m} \times 7.5\text{m}$. The defined area of detection and area of reference are processed with different hypotheses γ_p . This evaluation is only based on normalized peak intensities. The normalized peak intensities measured in those areas are plotted in Fig. 14 with respect to the NRS under test γ_p . The improvement in SCNR can be determined visually by looking at Fig. 14. In this experiment, the improvement was approximately 18 dB as the result of 8 dB concentration of the moving target's energy as well as -10 dB dispersion of the point target's

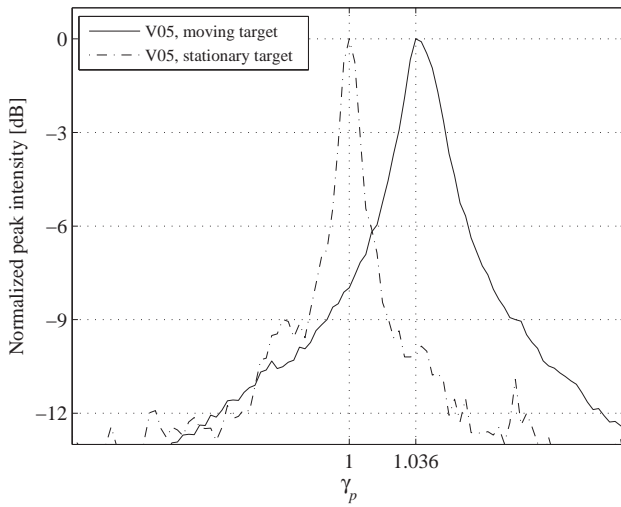


Figure 14: The measured normalized peak intensities on the area of detection $50\text{m} \times 12.5\text{m}$ and the area of reference $30\text{m} \times 7.5\text{m}$ processed by PBP with different γ_p . Optimum quantization step $\Delta\gamma = 3 \cdot 10^{-3}$, integration angle $\theta = 15^\circ$, minimum range to the object $r_0 \approx 7600$ m.

energy. This result is similar to the SCNR obtained from the simulations in Section 5.3.

7.3 Moving Target Estimation by Focusing

NRS can be estimated by testing new hypotheses $\gamma_{p,e}$ around the NRS=1.036 retrieved in the detection stage. Using the same integration angle for the detection stage $\theta = 15^\circ$, a new step size for this estimation $\Delta\gamma_e = 6 \cdot 10^{-4}$ is retrieved by (33) with a more strict threshold $h_{lim} = -0.1$ dB corresponding to $Q = 0.7$. The new hypotheses $\gamma_{p,e}$ are tested on the interval $[\text{NRS} - \Delta\gamma, \text{NRS} + \Delta\gamma]$, i.e. $[1.033, 1.039]$. The number of hypotheses $\gamma_{p,e}$ needed for estimation is therefore $N_{h,e} = 11$. The image pixel spacing for estimation can be reduced, for example, to $0.5\text{m} \times 0.5\text{m}$. The new hypotheses $\gamma_{p,e}$ are tested on a smaller area $10\text{m} \times 2.5\text{m}$ which is called the area of estimation. The number of image pixels is given by $N_{pixel} = 100$. An investigation

of the normalized peak intensities around the value $\text{NRS} = 1.036$ is given in Fig. 15.

A more accurate $\text{NRS} = 1.0372$ is retrieved in this estimation stage. Hence, the moving target detection by focusing technique, when applied with a smaller step size than the optimum for detection, can be seen as an NRS estimation method. However, if we perform the NRS estimation method with different integration angles, other motion parameters may be retrieved. In this experiment, we perform the NRS estimation method with another integration angle, i.e. $\theta = 30^\circ$, but use the same step size $\Delta\gamma_e = 6 \cdot 10^{-4}$. The retrieved peak intensities corresponding to different $\gamma_{p,e}$ is also plotted in Fig. 15. The maximum value of the peak intensities is reached at $\gamma_{p,e} = 1.0378$. The new estimated $\text{NRS} = 1.0378$ is different from the old estimated value 1.0372. In our other experiments where we estimated the NRS with the complete aperture, $\text{NRS} = 1.04$ was retrieved. The differences may be caused in part by the acceleration or the directional change of the moving object during the time interval of data collection. Movement of the ferry caused by sea waves and wind gives also rise to an imprecise estimation of NRS. The effects of such factors to NRS estimation are proportional to the increase of the integration angle. The different estimated NRS by different integration angle θ open also possibilities to estimate the speed, the acceleration and therefore the moving direction of the moving object by nonlinear tracking filters, i.e. Kalman filters [40]. For the multi-channel cases, such estimations can be simplified and accurate with the estimated NRS. However, these topics will not be presented in this paper.

The small figure in the upper right corner in Fig. 13 shows the contour plot of the EBBA BRAHE ferry after being focused with the estimated $\text{NRS} = 1.0378$. Contour plots at -3 dB , -9 dB , -15 dB and -21 dB are considered. A 3 dB reduction in the peak signal power corresponds to the smallest curve in the center of the contour plot. The dimensions of the -3 dB contour are approximately $10 \text{ m} \times 3 \text{ m}$. This should not be considered as the dimensions of the ferry but rather as the strongest reflector on the starboard side. In this case, the ferry has its large board side against the radar with a triangular shape with the wheelhouse on the top. This triangle probably causes the reflection with a maximum at the wheelhouse. Looking at the total reflection, it has an extension of $30\text{-}40 \text{ m}$ which is in agreement of the length of the ferry board. Apart from this long reflector is another one that is probably related to the second side of ferry, i.e. the port side of the car deck.

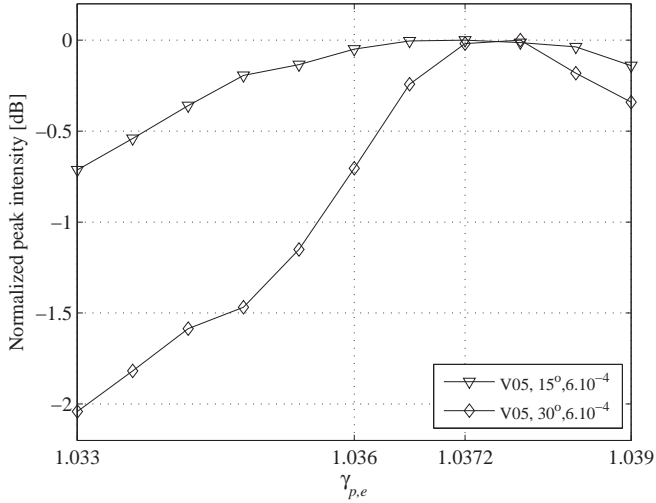


Figure 15: The measured normalized peak intensities on the area of estimation $10\text{m} \times 2.5\text{m}$ processed by PBP with different γ_p . Optimum quantization step $\Delta\gamma = 6 \cdot 10^{-4}$, integration angle $\theta = 15^\circ$ and $\theta = 30^\circ$, minimum range $r_0 \approx 7600$ m.

8 Conclusion

Moving target detection by focusing is a promising technique when UWB SAR systems are used, especially at low frequencies. Both time- and frequency-domain algorithms can be integrated into this technique, i.e. as the basic prerequisite for the focusing approach. The moving target detection by focusing technique does not require multi-channel data. However, applying this technique to single-channel is suboptimal. A combination of this technique with multi-channel techniques, e.g. DPCA and STAP to suppress clutter, will provide even better detection and estimation results. An important advantage of using this technique is that the ability of detection increases significantly even when a moving target may be surrounded by a considerable number of stationary targets or clutter. In the experiment on the simulated data, the improvement in SCNR is up to 20 dB at an integration angle $\theta = 15^\circ$. The second experimental results on the CARABAS-II data show a similar

improvement in SCNR (about 18 dB) using the same integration angle. This gain will be at least preserved when combining with multi-channel techniques.

The selection of integration angle for detection is critical. Wide integration angle allows better azimuth focusing and therefore higher possibility of the moving target detection. However, this is synonymous with long processing time and may be violate seriously the assumptions such as linear movements.

A fast time-domain algorithm PBP integrated into the moving target detection by focusing technique can easily be implemented on small areas with a manageable motion compensation. This may be a challenge for frequency-domain algorithms. Investigations in this paper also show that the number of operations needed for the detection also depends on the method for embedding the PBP. In the experiments where we concentrate on illustration and evaluation, the technique works well in the sea environments. However, to get a better performance and shorter processing time in reality, processing small areas and parallel processing are advised. The technique also shows the ability to estimate NRS and to indicate the existence of acceleration as well as changing direction. Other motion parameters such as the speed, the acceleration and therefore the moving direction are also possible to be estimated.

References

- [1] A. Gustavsson, L. M. H. Ulander, B. H. Flood, P.-O. Frölin, H. Hellsten, T. Jonsson, B. Larsson, and G. Stenstrom, “Development and operation of an airborne VHF SAR system—lessons learned,” in *Proc. IEEE IGARSS’98*, vol. 1, Seattle, WA, Jul. 1998, pp. 458–462.
- [2] L. M. H. Ulander and H. Hellsten, “Low-frequency ultrawideband array-antenna SAR for stationary and moving target imaging,” in *Proc. SPIE Radar Sensor Technology IV*, vol. 3704, Orlando, FL, Apr. 1999, pp. 149–158.
- [3] D. R. Sheen, C. M. Strawitch, and T. B. Lewis, “UHF wideband SAR design and preliminary results,” in *Proc. IEEE IGARSS’94*, vol. 1, Pasadena, CA, Aug. 1994, pp. 289–291.
- [4] L. Carin, N. Geng, M. McClure, J. Sichina, and L. Nguyen, “Ultra-wideband synthetic-aperture radar for mine-field detection,” *IEE Antennas and Propagation Magazine*, vol. 41, no. 1, pp. 18–33, 1999.

- [5] A. R. Brenner and J. H. G. Ender, "Demonstration of advanced reconnaissance techniques with the airborne SAR/GMTI sensor PAMIR," *IEE Proc.-Radar Sonar and Navigation*, vol. 153, no. 2, pp. 152–162, 2006.
- [6] L. M. H. Ulander, M. Lundberg, W. Pierson, and A. Gustavsson, "Change detection for low-frequency SAR ground surveillance," *IEE Proc.-Radar Sonar and Navigation*, vol. 152, no. 6, pp. 413–420, 2005.
- [7] J. K. Jao, "Theory of synthetic aperture radar imaging of a moving target," *IEEE Trans. Geosci. Remote Sensing*, vol. 39, no. 9, pp. 1984–1992, 2001.
- [8] R. Linnehan, L. Perlovsky, I. C. Mutz, M. Rangaswamy, and J. Schindler, "Detecting multiple slow-moving targets in SAR images," in *Proc. IEEE Sensor Array and Multichannel Signal Processing Workshop*, Barcelona, Spain, Jul. 2004, pp. 643–647.
- [9] M. I. Skolnik, *Radar Handbook*, 2nd ed. New York, NY: McGraw-Hill, 1990, ch. 16, pp. 8–17.
- [10] L. E. Brennan, J. D. Mallett, and I. S. Reed, "Adaptive arrays in airborne MTI radar," *IEEE Trans. Antennas Propagat.*, vol. 24, no. 5, pp. 607–615, 1976.
- [11] J. H. G. Ender, "Space-time processing for multichannel synthetic aperture radar," *IEE Electronics & Communication Engineering Journal*, vol. 11, no. 1, pp. 29–38, 1999.
- [12] M. Jahangir and C. P. Moate, "Utilising signal absence in SAR imagery for moving target detection," in *The IET Forum on Waveform Diversity and Design in Communications, Radar and Sonar*, London, UK, Nov. 2006, pp. 41–46.
- [13] J. R. Fienup, "Detecting moving targets in SAR imagery by focusing," *IEEE Trans. Aerosp. Electron. Syst.*, vol. 37, no. 3, pp. 749–809, 2001.
- [14] M. Rüegg, E. Meier, and D. Nüesch, "Capabilities of dual-frequency millimeter wave SAR with monopulse processing for ground moving target indication," *IEEE Trans. Geosci. Remote Sensing*, vol. 45, no. 3, pp. 539–553, 2007.
- [15] C. Liu and C. H. Gierull, "A new application for PolSAR imagery in the field of moving target indication/ship detection," *IEEE Trans. Geosci. Remote Sensing*, vol. 45, no. 2, pp. 3426–3436, 2007.

- [16] M. I. Pettersson, "Detection of moving targets in wideband SAR," *IEEE Trans. Aerosp. Electron. Syst.*, vol. 40, no. 3, pp. 780–796, 2004.
- [17] M. I. Pettersson, "Optimum relative speed discretisation for detection of moving objects in wide band SAR," *IET Radar, Sonar & Navigation*, vol. 1, no. 3, pp. 213–220, 2007.
- [18] S. Barbarossa, "Detection and imaging of moving objects with synthetic aperture radar. 1. Optimal detection and parameter estimation theory," *IEE Proc.-Radar and Signal Processing*, vol. 139, no. 1, pp. 79–88, 1992.
- [19] O. Seger, M. Herberthson, and H. Hellsten, "Real time SAR processing of low frequency ultra wide band radar data," in *Proc. EUSAR'98*, Friedrichshafen, Germany, May 1998, pp. 489–492.
- [20] V. T. Vu, T. K. Sjögren, M. I. Pettersson, H.-J. Zepernick, and A. Gustavsson, "Experimental results on moving targets detection by focusing in UWB low frequency SAR," in *Proc. IET RADAR'2007*, Edinburgh, UK, Oct. 2007, pp. 562–566.
- [21] V. T. Vu, T. K. Sjögren, and M. I. Pettersson, "Moving target detection by focusing for frequency domain algorithms in UWB low frequency SAR," in *Proc. IEEE IGARSS'2008*, Boston, MA, Jul. 2008, pp. 161–164.
- [22] L. E. Andersson, "On the determination of a function from spherical averages," *SIAM Journal on Mathematical Analysis*, vol. 19, no. 1, pp. 214–232, 1988.
- [23] A. F. Yegulalp, "Fast backprojection algorithm for synthetic aperture radar," in *Proc. IEEE RadarCon'99*, Waltham, MA, Apr. 1999, pp. 60–65.
- [24] M. I. Pettersson, "Focusing of moving targets in an ultra wide band SAR GMTI system," in *Proc. EUSAR'2000*, Munich, Germany, May 2000, pp. 837–840.
- [25] L. M. H. Ulander, H. Hellsten, and G. Stenstrom, "Synthetic-aperture radar processing using fast factorized back-projection," *IEEE Trans. Aerosp. Electron. Syst.*, vol. 39, no. 3, pp. 760–776, 2003.
- [26] P.-O. Fröling and L. M. H. Ulander, "Evaluation of angular interpolation kernels in fast back-projection SAR processing," *IEE Proc.-Radar Sonar and Navigation*, vol. 153, no. 3, pp. 243–249, 2006.

- [27] C. Cafforio, C. Prati, and F. Rocca, “SAR data focusing using seismic migration techniques,” *IEEE Trans. Aerosp. Electron. Syst.*, vol. 27, pp. 194–207, Mar. 1991.
- [28] V. T. Vu, T. K. Sjögren, and M. I. Pettersson, “Ultra-wideband chirp scaling,” *IEEE Geosci. Rem. Sens. Lett.*, vol. 7, no. 2, pp. 282–286, 2010.
- [29] V. T. Vu, T. K. Sjögren, and M. I. Pettersson, “Fast detection of moving targets by focusing in Ultra-wideband SAR,” in *Proc. IEEE Radar Con’2009*, Pasadena, CA, May 2009, pp. (5p).
- [30] V. T. Vu, T. K. Sjögren, and M. I. Pettersson, “Fast detection of moving targets by focusing in multi-channel Ultra-wideband SAR,” in *EuRAD 2009*, Rome, Italy, Sep. 2009, pp. 218–221.
- [31] R. K. Raney, H. Runge, R. Bamler, I. G. Cumming, and F. H. Wong, “Precision SAR processing using chirp scaling,” *IEEE Trans. Geosci. Remote Sensing*, vol. 32, no. 4, pp. 786–799, 1994.
- [32] V. T. Vu, T. K. Sjögren, and M. I. Pettersson, “A comparison between fast factorized backprojection and frequency-domain algorithms in UWB low frequency SAR,” in *Proc. IEEE IGARSS’2008*, Boston, MA, Jul. 2008, pp. 1293–1296.
- [33] G. W. Davidson, I. G. Cumming, and M. R. Ito, “A chirp scaling approach for processing squint mode SAR data,” *IEEE Trans. Aerosp. Electron. Syst.*, vol. 32, no. 1, pp. 121–133, 1996.
- [34] L. M. H. Ulander and H. Hellsten, “A new formula for SAR spatial resolution,” *AEÜ International Journal of Electronics and Communications*, vol. 50, no. 2, pp. 117–121, 1996.
- [35] T. K. Sjögren, V. T. Vu, M. I. Pettersson, H.-J. Zepernick, and A. Gustavsson, “Speed estimation experiments for ground moving targets in UWB SAR,” in *Proc. IET RADAR’2007*, Edinburgh, UK, Oct. 2007, pp. 519–523.
- [36] V. T. Vu, T. K. Sjögren, M. I. Pettersson, and P. A. C. Marques, “Application of moving target detection by focusing technique in civil traffic monitoring,” in *Proc. IEEE IGARSS’2010*, Honolulu, HI, Jul. 2010, pp. (4p).

- [37] V. T. Vu, T. K. Sjögren, M. I. Pettersson, and A. Gustavsson, “Definition on SAR image quality measurements for UWB SAR,” in *Proc. SPIE Image and Signal Processing for Remote Sensing XIV*, vol. 7109, Cardiff, UK, Sep. 2008, pp. 71091A (9p).
- [38] O. Frey, C. Magnard, M. Rüegg, and E. Meier, “Focusing of airborne synthetic aperture radar data from highly non-linear flight tracks,” *IEEE Trans. Geosci. Remote Sensing*, vol. 47, no. 6, pp. 1844–1858, 2009.
- [39] V. T. Vu, T. K. Sjögren, and M. I. Pettersson, “Integrating space-time processing into time-domain backprojection process to detect and image moving object,” in *Proc. IEEE IGARSS’2010*, Honolulu, HI, Jul. 2010, pp. (4p).
- [40] B. Ristic, S. Arulampalam, and N. Gordon, *Beyond the Kalman filter - Particle filters for tracking application*, London, UK: Artech House, 2004, ch. 5, pp. 85–102.

Part III—B

Part III–B

Fast Detection of Moving Targets by Focusing
in UWB Low Frequency SAR

Part III–B is published as:

V. T. Vu, T. K. Sjögren, and M. I. Pettersson, “Fast detection of moving targets by focusing in UWB low frequency SAR,” in *Proc. IEEE RadarCon’2009*, Pasadena, CA, May 2009, pp. 1–5.

Fast Detection of Moving Targets by Focusing in UWB Low Frequency SAR

V. T. Vu, T. K. Sjögren, and M. I. Pettersson

Abstract

Moving target detection in Ultra-Wideband (UWB) SAR is associated with long integration time and has to handle azimuth focusing for reliable detection. This paper presents the theory and simulation results of the Fast Detection of Moving Targets by Focusing method (FDMTF) which is understood as the Detection of Moving Targets by Focusing method (DMTF) incorporating fast time-domain algorithms in the process. Two fast time-domain algorithms Fast Backprojection (PBP) and Fast Factorized Backprojection (FFBP) are considered. The results show that FDMTF performs very efficiently and still retains the ability of detection.

1 Introduction

Detection of Moving Targets by Focusing (DMTF) [1] is known as a promising detection technique used in Ultra-Wideband (UWB) SAR. This technique facilitates slow moving target detection which may be challenging for the detection techniques with short integration time. The technique supports both single- and multi-channel SAR data. The improvement in Signal-to-Clutter Ratio (SCR) measured in the experiments on single-channel SAR data is up to approximately 20 dB [2]. This gain will at least be preserved for the case of multi-channel SAR data. The experimental results in [2] also show the ability to detect moving targets, which may be fully obscured by a considerable number of stationary targets, i.e. clutter. In addition, motion parameters of the detected targets can also be initially estimated. However, the processing time for detection needed by DMTF is usually long. One reason for the long processing time is the large number of blind hypotheses which need to be tested. The other is that the detection technique is built on the

SAR imaging algorithm Global Backprojection (GBP) [3]. This algorithm always requires high computational cost itself.

Several research works to overcome this shortcoming of DMTF have been managed in which using frequency-domain algorithms in DMTF can be seen as a temporary solution. Investigations in [4] have shown that the frequency-domain algorithms, e.g. Range Migration (RM) [5], can be selected to be the basis for the focusing approach in DMTF. Without motion error, the performance of RM and GBP are almost identical in terms of image quality which refers to the ability of detection. Since DMTF does not always require very large integration angle, other frequency-domain algorithms such as Ultra-wideband Chirp Scaling (UCS) [6] can also be integrated into DMTF. However, RM or UCS may not exploit strong points of DMTF. Thanks to the local processing characteristic of GBP using in DMTF, the area of interest, where blind hypotheses are tested, can be from a small area to the whole SAR scene. The image pixel spacing can also be set as desired. These flexibilities may not be valid for the frequency-domain algorithms. For frequency-domain algorithms, we always need to process whole SAR scene with a fixed image pixel spacing, which is decided by the ratio of platform speed to Pulse Repetition Frequency (PRF) and the range sampling frequency. Extra steps such as extracting the defined areas of interest from whole SAR scene and either down- or upsampling to reach the expected image pixel spacing are needed. Beside this, motion error compensation, which can be seen as an inherent challenge of the frequency-domain algorithms, also requires computational cost and is difficult to handle [7]. For those reason, the frequency-domain algorithms are not at an advantage compared with the time-domain algorithms in DMTF.

Basically, if we replace GBP in DMTF by fast time-domain algorithms such as Fast Backprojection (PBP) [8] or Fast Factorized Backprojection (FFBP) [9], the processing time needed for the detection will be reduced significantly. However, the processing time can be reduced further, depending on the methods to integrate these algorithms into DMTF. DMTF integrated one fast time-domain algorithm is called the Fast Detection of Moving Targets by Focusing method and denoted by FDMTF.

The objective of this paper is to present theory and simulation results of the FDMTF on single channel SAR data. Different methods to integrate the fast time-domain algorithms into FDMTF to achieve the best performance in terms of processing time are discussed in details. Simulated data used in this study is based on the parameters of CARABAS-II system [10] which is known as an airborne UWB low frequency SAR system. However, FDMTF is also available for other single- or multi-channel SAR systems, e.g. LORA [11].

The paper is organized as follows. Section 2 reviews the fast time-domain algorithms which are the subjects to integrate into DMTF. Methods to integrate these algorithms into DMTF to reduce the processing time are proposed in Section 3. Simulation results and evaluations of the FDMTF are presented in Section 4. Section 5 provides the conclusions.

2 Fast Time-Domain Algothirms

In this section, we review two fast time-domain algorithms PBP and FFBP. These algorithms will be the subjects to integrate into DMTF.

A SAR image is considered as a linear transformation from the radar echo data. The global backprojection process [3] places a position (x_i, r_j) in the SAR image and is simply interpreted by an integral

$$h(x_i, r_j) = \int_{-\frac{L}{2}}^{+\frac{L}{2}} g\left(v_{plt}, \sqrt{(v_{plt} - x_i)^2 - r_j^2}\right) d(v_{plt}) \quad (1)$$

where L is the aperture length and $g(x, r)$ represents the range-compressed data.

2.1 Fast Backprojection

In the PBP, two concepts - polar image and slant-range image - are used [8]. PBP splits the complete aperture into subapertures. From the center of each subaperture, a polar grid $(\cos\hat{\alpha}, \hat{r})$ is created. The polar grid must cover the full slant-range image and meet the Nyquist sampling requirements for $\cos\hat{\alpha}$ and \hat{r}

$$\Delta\cos\hat{\alpha} < \frac{c}{2f_{max}L_s} \quad (2)$$

$$\Delta\hat{r} < \frac{c}{2B} \quad (3)$$

where f_{max} is the maximum radar signal frequency, L_s is the subaperture size, c is the speed of light and B is the signal bandwidth. The polar images are retrieved by superposition of backprojected data in polar grids. The range from a position in the l -th subaperture to a pixel (m, n) of the l -th polar image is determined by

$$\tilde{r}_{l,m,n}(t) = \sqrt{(v_{plt} - x_l - \hat{r}_n \cos\hat{\alpha}_m)^2 + (\hat{r}_n \sin\hat{\alpha}_m)^2}. \quad (4)$$

The slant-range image is obtained by a linear mapping from all the polar images. The range from the center of the l -th subaperture to a slant-range image pixel (x_i, r_j) and the cosine of the angle between the range and the flight track vectors are derived as

$$\bar{r}_{l,i,j} = \sqrt{(x_l - x_i)^2 + r_j^2} \quad (5)$$

$$\cos(\bar{\alpha}_{l,i,j}) = \frac{x_l - x_i}{\bar{r}_{l,i,j}}. \quad (6)$$

2.2 Fast Factorized Backprojection

Two versions of FFBP, one based on Local Backprojection (LBP) [12] and the other on PBP, are proposed in [9]. The latter is aimed at in this paper. FFBP based on PBP can be interpreted as PBP processing data in multiple polar-mapping stages so-called factorization. The polar grids in the polar-mapping stages must be large enough to cover the slant-range grid. In the first polar-mapping stage, the complete aperture is divided into a number of first-stage subapertures. From the center of each first-stage subaperture, the first-stage polar grid is created. The range compressed data is mapped into the first-stage polar grids to form the first-stage polar images. In the second polar-mapping stage, a number of the first-stage subapertures are combined together to create the second-stage subaperture. The second-stage polar grids are formed from the center of the second-stage subapertures. The second-stage polar image is retrieved by a coherent mapping from the first-stage polar images into the second-stage polar grid. The polar-mapping stages are repeated until the final polar-mapping stage. The number of the polar-mapping stages or factorizations depends strongly on SAR system parameters, required image quality and processing time.

3 Fast Detection of Moving Targets by Focusing

A moving target can be considered as a stationary target in the SAR formation process if the platform carrying the SAR equipment is assumed to move with a velocity which is the vector sum of the original platform velocity and the target velocity. The normalized relative speed (NRS) is the absolute value of

the assumed velocity vector [1]

$$\gamma_t = \sqrt{\frac{(v_{pl} - v_\xi)^2 + v_\eta^2}{v_{pl}^2}}. \quad (7)$$

where v_{pl} is the speed of the platform, v_ξ and v_η are the moving target velocity components in ξ and η directions, respectively. All movements are assumed to have constant speeds, i.e. no acceleration. As mentioned in [1], the moving target can be focused with NRS if its motion parameters such as v_ξ and v_η are known. In reality, these parameters are usually unknown and will therefore require complicated estimate procedures to be retrieved. These procedures can be applied only if the presence of the moving target is indicated or in other words, the moving target must be detected before applying estimate procedures. For detection, different hypotheses γ_p (so-called NRS under test) on γ_t have to be tested until the detection is reached. The highest probability of detection can be obtained for the smallest step size between the tests. An optimum quantization step size $\Delta\gamma$ for detection is proposed in [13]. The derivation of the step size is based on the decrease of the Impulse Response in SAR imaging (IR-SAR) of a point target given by the GBP integral [3] and approximated by

$$\Delta\gamma \approx \frac{Q^2 c r_0}{2\pi f_c \gamma_t v_{pl}^2 t_i^2}. \quad (8)$$

where Q is the detection constant given by a threshold h_{lim} which should be set as desired to meet the requirement of the acceptable detection failure. The minimum range to the predicted position of a moving target is denoted by r_0 , f_c is the center frequency and t_i is the integration time for the detection. Based on the maximum speed of the target, which is expected to detect in the area of interest, different hypotheses are tested in the range [1]

$$\gamma_p \in \left[1 - \max \left\{ \frac{v_{tg}}{v_{pl}} \right\}, 1 + \max \left\{ \frac{v_{tg}}{v_{pl}} \right\} \right] \quad (9)$$

For DMTF, the number of operations to perform the detection method on an area of interest $N \times N$ pixels is counted as

$$\Sigma_0 = N_h \times N_a \times N^2 \quad (10)$$

where N_h is the number of hypotheses and N_a is the number of aperture positions considered for the DMTF. To increase the performance of the detection method in term of processing time with a defined area of interest, we

might reduce N_h and N_a . A reduction of N_h is synonymous with a reduction of probability of detection since N_h is a function of $\Delta\gamma$. Decreasing N_h is therefore not realistic. We may select smaller N_a i.e. smaller integration angle. However, the integration angle must be chosen large enough to handle azimuth focusing and to obtain a significant improvement in Signal to Clutter Ratio (SCR) [1].

We propose here several methods to integrate PBP and FFBP, which are reviewed in Section II, into DMTF to make the detection method become much more efficient. It is obvious that moving target focusing can be done in the polar image formation or slant-range image formation. In the first case, FDMTF scales the platform speed with different values of γ_p in (4) as

$$\tilde{r}_{l,m,n}(t) = \sqrt{\gamma_p^2 \cdot (v_{plt}t - x_l - \hat{r}_n \cos \hat{\alpha}_m)^2 + (\hat{r}_n \sin \hat{\alpha}_m)^2}. \quad (11)$$

FDMTF needs to calculate coordinates of the polar grid, backproject data on the polar grids, upsample polar images and map the polar images to slant-range image for all subaperture and all hypotheses. The number of operations required to perform FDMTF integrated PBP is estimated as

$$\Sigma_1 = N_h \times N_a \times N \times \left(2 + N_s + \frac{N}{N_s} \right) \quad (12)$$

where N_s is the number of aperture positions in one subaperture. The optimum value of N_s can be retrieved by solving the first derivative of (12) with respect to N_s as

$$\frac{\partial}{\partial N_s} \left\{ N_h \times N_a \times N \times \left(2 + N_s + \frac{N}{N_s} \right) \right\} = 0 \quad (13)$$

The solution of (13) is shown to be

$$N_s = \sqrt{N} \quad (14)$$

The optimum number of operations for detection is therefore given by

$$\Sigma_{1,o} = 2 \times N_h \times N_a \times N \times \left(1 + \sqrt{N} \right) \quad (15)$$

In the second case, where the blind hypotheses are tested on the slant-range image formation, the platform speed component existing in x_l in (5) is scaled by γ_p as

$$\bar{r}_{l,i,j} = \sqrt{\gamma_p^2 \cdot (x_l - x_i)^2 + r_j^2}. \quad (16)$$

In such case, it is not necessary to repeat calculating coordinates of the polar grid, backprojection data on polar grid and upsampling polar image steps for each hypothesis. Basically, the optimum number of operations needed for detection is reduced to

$$\Sigma_2 = N_a \times N \times \left(2 + N_s + \frac{N_h \times N}{N_s} \right) \quad (17)$$

With the optimum value of N_s retrieved from the first derivative of (17) with respect to N_s

$$N_s = \sqrt{N_h \times N}, \quad (18)$$

the number of operations for detection is optimized as

$$\Sigma_{2,o} = 2 \times N_a \times N \times \left(1 + \sqrt{N_h \times N} \right). \quad (19)$$

It is seen clearly that the FDMTF integrated PBP with γ_p tested on the slant-range image formation give advantages of processing time over on the polar image formation. For large areas of interest ($N \gg 1$), the detection by moving target focusing in the slant-range image formation, i.e. using (16), runs faster than in the polar image formation, i.e. using (11), approximately $\sqrt{N_h}$ time.

Similarly, FDMTF integrated FFBP can also be performed either on the polar image formation in any polar-mapping stages or the slant-range image formation. Testing different blind hypotheses γ_p on the latter polar-mapping stages gives advantages of processing time over the beginning polar-mapping stages. However, testing on the slant-range image formation requires shortest processing time. Hence, in the last case, where different blind hypotheses γ_p are tested on the slant-range image formation using (16), the number of operations for detection is estimated by

$$\Sigma_3 = N_a \times N \times \left[2 + N_s + (L - 1) \times (2 + N_f) + \frac{N_h \times N}{N_s \times N_f^{L-1}} \right] \quad (20)$$

where L is the number of the polar-mapping stages and N_f is the factorization factor. The optimum value of N_s can also be derived from the first derivative of (20) with respect to N_s as

$$N_s = \sqrt{\frac{N_h \times N}{N_f^{L-1}}}. \quad (21)$$

Table 1: The CARABAS-II Simulated Parameters

Parameter	Value
The highest frequency processed	82 MHz
The lowest frequency processed	22 MHz
Platform speed v_{pl}	128 m/s
Flight altitude	3700 m
Minimum range to the aim point	7150 m
Pulse Repetition Frequency (PRF)	137

Substituting (21) to (20) results in an optimum number of operations for detection as

$$\Sigma_{3,o} = 2 \times N_a \times N \times \left[1 + \sqrt{\frac{N_h \times N}{N_f^{L-1}}} + (L-1) \times \left(1 + \frac{N_f}{2} \right) \right]. \quad (22)$$

If $L = 1$, i.e. only one polar-mapping stage or in other word PBP, (19) and (22) are identical. Since N_s given in (18) and (21) are functions of N_h , they must comply with (8).

4 Simulation Results and Evaluations

In this section, we present simulation results and give evaluations for FDMTF. We use simulated CARABAS-II SAR data. The main parameters of this system are summarized in Table 1. The simulated ground scene consists of one moving target which is the subject to be detected and another stationary target which can be used to evaluate the performance of the FDMTF. The moving target is assumed to be a ship, a boat or a ferry as in [2] with point-like scattering. The maximum speed of such vessels is about 25 knots (≈ 12.8 m/s). The moving direction is unknown. The stationary target is also assumed to be point target. In reality, a corner reflector can be seen a point target in a SAR image. The simulated SAR scene is imaged by both PBP and 3-stage FFBP with the factorization factor $N_f = 4$ and given in Fig. 1.a and

1.b. The SAR images are processed with 2000 aperture positions which refers to an integration angle of about $\phi_0 = 15^\circ$ with respect to the aim point. The moving target on the right hand side of the SAR images is defocused and appears in the SAR images as black ellipse curves. Small black points on the left hand side are images of the stationary target.

FDMTF is assumed to processes the same integration angle $\phi_0 = 15^\circ$. The total number of the aperture positions is therefore $N_a = 2000$. With the given parameters in Table 1 and based on (8), an optimum quantization step size for detection is shown to be $\Delta\gamma = 5 \cdot 10^{-3}$ which corresponds to the threshold of $h_{lim} = 3$ dB allowing maximum loss of 3 dB from the peak IR-SAR. Equation (9) results in a hypothesis range $\gamma_p \in [0.9, 1.1]$. The number of blind hypotheses with the optimum quantization step size and the hypothesis range is $N_h = 41$. For testing purposes, both the area of interest and reference in this simulation can be chosen relatively small and are defined by areas surrounding the center of the ellipse curves and the points in the imaged SAR scene, respectively. In reality, areas of interest are usually very large, e.g. forest where moving targets can be hidden by thick foliage or a long road where over speed vehicles need to be indicated.

Fig. 2 shows the relationship between γ_p and the retrieved peak IR-SAR in the areas of interest and reference. At $\gamma_p = 1.04$, the peak IR-SAR is reached with both PBP and FFBP. This indicates the presence of an moving with $\gamma_t \approx 1.04$ in the area of interest. The simulated SAR scene is again imaged with the assumed platform speed $1.04 \cdot v_{pl}$ and shown in Fig. 1.c and 1.d. The reference point target is now defocused in the SAR images whereas the moving target is focused to the original shape (point-like).

The evaluation is based on a comparison between DMTF and FDMTF in terms of detection ability and processing time. The detection ability can be measured directly by the improvement in SCR which is proposed in [1]. The measurement consider the retrieved peak IR-SAR in the area of interest before and after focusing as well as in the area of reference. Fig. 2 also plots the detection results of DMTF with the same parameters processed by FDMTF. The improvement in SCR can be visually estimated about 20 dB for two FDMTF versions, i.e. integrated PBP and FFBP. This result approximates the same improvement in SCR obtained with DMTF (less than 1 dB difference).

Since the processing time is always proportional to the number of operations needed for detection, an investigation on this number is sufficient for evaluation purposes. Fig. 3 shows a comparison between numbers of operations required by DMTF and two FDMTF versions which are described by

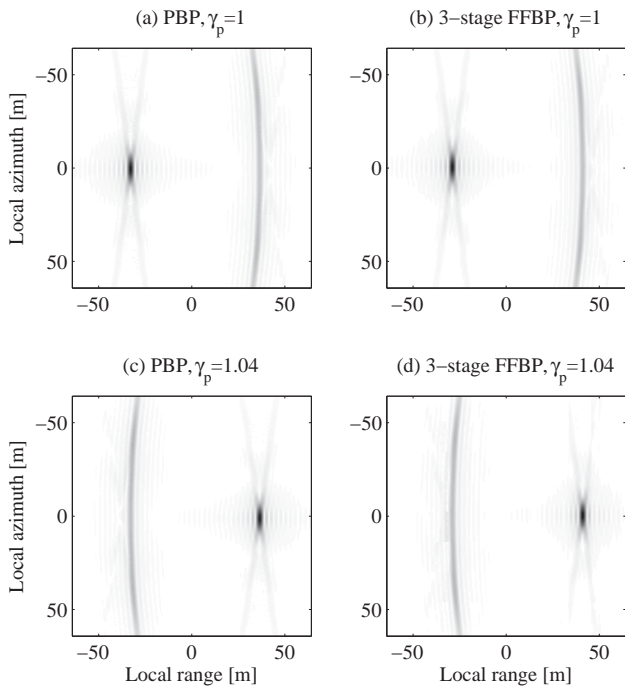


Figure 1: Simulated SAR scene imaged by PBP and FFBP with parameters given in Table 1. The image is processed with 2000 aperture positions which refers to an integration angle of about $\phi_0 = 15^\circ$ with respect to the aim point. (a) PBP, (b) FFBP, (c) PBP and $\gamma_p = 1.04$, (d) FFBP and $\gamma_p = 1.04$.

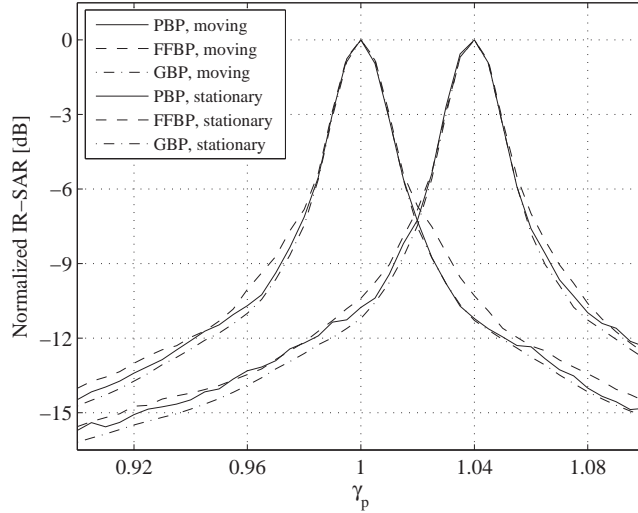


Figure 2: The measured normalized IR-SAR on the areas of interest and reference in dB scale. The simulated SAR scene is processed by PBP and FFBP with different NRS undertest γ_p . For evaluation purposes, the simulated SAR scene is processed by GBP. Both DMTF and two FDMTF versions process with the optimum quantization step size for detection $\Delta\gamma = 5 \cdot 10^{-3}$, the integration angle $\theta = 15^0$, the hypothesis range $\gamma_p \in [0.9, 1.1]$ and the minimum range $r_0 \approx 7150$ m.

(19) and (21), i.e. testing on the slant-range image formation. Since the area of interest can be chosen arbitrarily from extremely small areas to the whole SAR scene, areas from $1 \text{ m} \times 1 \text{ m}$ to $5120 \text{ m} \times 5120 \text{ m}$, full SAR scene given in [1], with 1 m sampling in each direction will be investigated. The results plotted in the Fig. 3 show that if the area of interest is small, the difference in the numbers of operations can be negligible. However, this does not hold true for large areas of interest. For example, FDMTF integrated PBP can run faster than DMTF about 230 times for the same area of interest $5120 \text{ m} \times 5120 \text{ m}$ with 1 m sampling. The plots in Fig. 3 also show that the processing time for FDMTF integrated FFBP depends on the number of the mapping-polar stages L and the factorization factor N_f . In this simulation, FDMTF integrated 4-stage FFBP with $N_f = 8$ runs faster than DMTF up

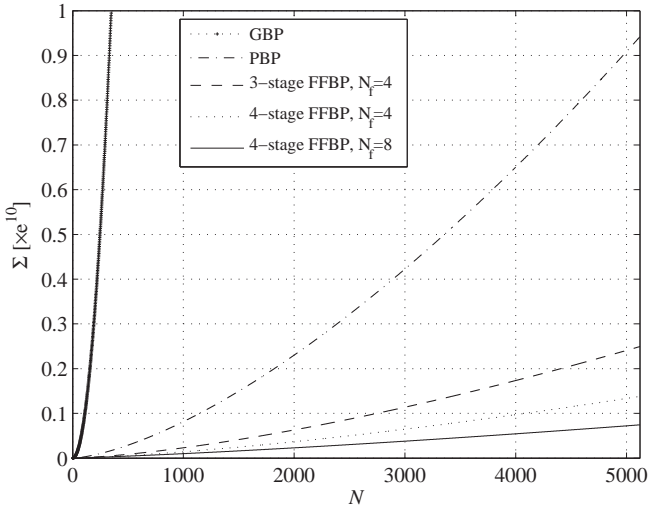


Figure 3: Optimum number operations need for DMTF and different FDMTF versions as functions of the area of interest. The number of the aperture positions is $N_a = 2000$, which refers to an integration angle of $\phi_0 = 15^\circ$, and the number of the tested hypotheses is $N_h = 41$.

to 3000 times for the same area of interest $5120 \text{ m} \times 5120 \text{ m}$. This is a huge improvement in processing time.

5 Conclusion

In this paper, we present theory and simulation results of the FDMTF on single channel SAR data. Two FDMTF versions integrated PBP and FFBP reduce the processing time significantly but retain the ability of detection. Investigations in this paper show that processing time is also affected by the methods to integrate PBP and FFBP in FDMTF. Evaluation results show that FDMTF performs much more efficient than DMTF in terms of processing time, especially on large areas of interest. Although data used in this study is based on the parameters of CARABAS-II system operating in VHF-band, FDMTF is also available for other single- and multi-channel SAR systems. A

combination FDMTF with space-time processing techniques for more reliable detection will be presented in another paper.

References

- [1] V. T. Vu, T. K. Sjögren, M. I. Pettersson, H.-J. Zepernick, and A. Gustavsson, "Experimental results on moving targets detection by focusing in UWB low frequency SAR," in *Proc. IET RADAR'2007*, Edinburgh, UK, Oct. 2007, pp. 562–566.
- [2] V. T. Vu, T. K. Sjögren, M. I. Pettersson, L. M. H. Ulander, and A. Gustavsson, "Moving targets detection by focusing in UWB SAR - Theory and experimental results," *IEEE Trans. Geosci. Remote Sensing*, submitted for publication.
- [3] L. E. Andersson, "On the determination of a function from spherical averages," *SIAM Journal on Mathematical Analysis*, vol. 19, no. 1, pp. 214–232, 1988.
- [4] V. T. Vu, T. K. Sjögren, and M. I. Pettersson, "Moving target detection by focusing for frequency domain algorithms in UWB low frequency SAR," in *Proc. IEEE IGARSS'2008*, Boston, MA, Jul. 2008, pp. 161–164.
- [5] C. Cafforio, C. Prati, and F. Rocca, "SAR data focusing using seismic migration and techniques," *IEEE Trans. Aerosp. Electron. Syst.*, vol. 27, pp. 194–207, Mar. 1991.
- [6] V. T. Vu, T. K. Sjögren, and M. I. Pettersson, "Ultra-wideband chirp scaling," *IEEE Signal Processing Lett.*, submitted for publication.
- [7] O. Frey, C. Magnard, M. Rüegg, and E. Meier, "Focusing SAR data acquired from non-linear sensor trajectories," in *Proc. IEEE IGARSS'2008*, Boston, MA, Jul. 2008, pp. 415–418.
- [8] A. F. Yegulalp, "Fast backprojection algorithm for synthetic aperture radar," in *Proc. IEEE RadarCon'99*, Waltham, MA, Apr. 1999, pp. 60–65.
- [9] L. M. H. Ulander, H. Hellsten, and G. Stenstrom, "Synthetic-aperture radar processing using fast factorized back-projection," *IEEE Trans. Aerosp. Electron. Syst.*, vol. 39, no. 3, pp. 760–776, 2003.

- [10] H. Hellsten, L. M. H. Ulander, A. Gustavsson, and B. Larsson, “Development of VHF CARABAS II SAR,” in *Proc. SPIE Radar Sensor Technology*, vol. 2747, Orlando, FL, Apr. 1996, pp. 48–60.
- [11] L. M. H. Ulander and H. Hellsten, “Low-frequency ultrawideband array-antenna SAR for stationary and moving target imaging,” in *Proc. SPIE Radar Sensor Technology IV*, vol. 3704, Orlando, FL, Apr. 1999, pp. 149–158.
- [12] O. Seger, M. Herberthson, and H. Hellsten, “Real time SAR processing of low frequency ultra wide band radar data,” in *Proc. EUSAR’98*, Friedrichshafen, Germany, May 1998, pp. 489–492.
- [13] M. I. Pettersson, “Optimum relative speed discretisation for detection of moving objects in wide band SAR,” *IET Radar, Sonar & Navigation*, vol. 1, no. 3, pp. 213–220, 2007.

Part III—C

Part III–C

Integrating Space-Time Processing into
Time-Domain Backprojection Process to
Detect and Image Moving Objects

Part III–C is published as:

V. T. Vu, T. K. Sjögren, and M. I. Pettersson, “Integrating space-time processing into time-domain backprojection process to detect and image moving objects,” in *Proc. IEEE IGARSS’2010*, Honolulu, HI, Jul. 2010, pp. 4106–4109.

Integrating Space-Time Processing into Time-Domain Backprojection Process to Detect and Image Moving Objects

V. T. Vu, T. K. Sjögren, and M. I. Pettersson

Abstract

This paper discusses a possibility to integrate space-time processing into the time-domain backprojection process. This combination allows detection as well as imaging moving objects. Two space-time techniques, Displaced Phase Center Antenna (DPCA) and Space-Time Adaptive Processing (STAP), are considered for this integration. Simulated results based on the LORA parameters demonstrate the efficiency of detection and imaging moving objects.

1 Introduction

Detection and imaging moving objects, even hidden by strong clutter on the ground, make Synthetic Aperture Radar (SAR) more and more important for Ground Moving Target Indication (GMTI). Moving target detection is most commonly performed by GMTI radars based on antenna array solutions without imaging capability while SAR systems do not facilitate indicating the presence of moving objects in an imaged SAR scene. Moving targets are usually displaced and defocused in a SAR image. Distinguishing them from strong ground clutter requires much effort.

The possibility to use SAR for moving target detection has been discussed in several publications, which can be divided into two categories: detection techniques for single-channel and multi-channel SAR. For single-channel SAR, the most primitive detection technique has been based on Doppler shift originated by moving objects. However, such techniques only work under certain circumstances. For example the speed of the moving objects needs to be

high enough to produce Doppler shift, which are distinguishable from the surrounding stationary clutter. Another simple detection technique is relied on shadow phenomenon caused by the displacement if moving objects are present at an image scene. The detection is possible in strong ground clutter SAR environment. One of the more advanced detection techniques, named moving target detection by focusing, appears in some recent publications. The principle of the technique is to focus moving targets with correct Normalized Relative Speed (NRS) while defocus ground clutter, i.e. suppress ground clutter, simultaneously. The technique is shown to be suitable for ultrawideband (UWB) SAR systems and can be combined with space-time processing techniques for more reliable detection.

Applying space-time processing techniques to multi-channel SAR for detection and imaging the moving objects is a topic of interest. Displaced phase center antenna (DPCA) [1], i.e. non-adaptive, and space time adaptive processing (STAP) [2] are known as mostly used space-time processing techniques. Using DPCA as a data pre-processing technique for moving target detection in dual-channel UWB SAR has been introduced in [3]. According to this proposal, dual-channel SAR data is first handled by DPCA to suppress ground clutter. The suppressed clutter data is then processed by the moving target detection by focusing technique. This combination is supposed to provide a reliable detection. In [4], STAP is also considered as a pre-process for SAR data to improve as much as possible the signal to clutter noise ratio (SCNR) for detection. Further processing such as filter and estimation can be applied to the SAR data to reconstruct the SAR image of the moving objects.

The goal of this paper is to present a possibility to integrate different space-time techniques into the time-domain local backprojection process for detection and imaging moving objects. Integrating STAP into the local backprojection process in wideband radar have once suggested in [5]. In this paper, two space-time processing techniques, i.e. DPCA and STAP, are subjects for this combination. The integration is expected to lighten the strict requirements as well as improve the practicality of two techniques. The proposal is demonstrated and evaluated by simulations based on the LORA parameters.

The paper is organized as follows. Section 2 reviews two space-time techniques, i.e. DPCA and STAP. Section 3 describes the local backprojection process. Integrating two space-time techniques into local backprojection processing is proposed in Section 4. Simulated results based on the LORA parameters are presented in Sections 5. Section 6 provides the conclusions.

2 Space-time processing

The ability to detect moving targets in an illuminated SAR scene depends strongly on the ability to suppress ground clutter and noise, i.e. ability to filter the signal. The ground clutter is interpreted as the radar backscattering in the illuminated SAR scene while the noise is thermal noise originated from the environment and the SAR system.

The simplest space-time processing technique is known as DPCA [1]. Basically, the technique is based on a side looking array with two antennas aligned along the flight track and spaced by a Pulse Repetition Interval (PRI). Two successive pulses transmitted and received in turn by the forward and backward antennas. The motion of the aircraft after one PRI places the backward antenna to the previous position of the forward antenna. It is obvious that two successive pulses are transmitted and received at the same position in space but separated by one PRI in time. Simple ground clutter suppression is obtained by subtracting the second echo received by the backward antenna from the first echo received by the forward antenna. However, DPCA has very high demands on, for example, the straight flight track, constant platform speed and identical channels. From the detection's point of view, DPCA is quite sensitive to the speed of the moving targets. The subtraction in DPCA can suppress the ground clutter but can also raise the noise level significantly.

STAP refers to an efficient space-time processing technique providing improved detection of moving objects obscured by ground clutter and noise. Let's have a look again at the theory of adaptive radar developed in [2]. According to Theorem 1, the optimum weights, which maximize signal to noise ratio (SNR), are given by

$$\mathbf{w} = \kappa \mathbf{R}^{-1} \mathbf{s}^* \quad (1)$$

where the asterisk denotes complex conjugation operation, κ is a nonzero complex number and \mathbf{R} is the noise covariance matrix. The echo from a target at a given range delay is denoted by \mathbf{s} which can be represented by

$$\mathbf{s} = [s_{11} \cdots s_{1M} \cdots s_{N1} \cdots s_{NM}]^T \quad (2)$$

where N is the number of antennas and M is the number of samples yielded by each antennas. The subscript T denotes transpose operator. The theory can be further extended for the case where an object is obscured by ground clutter and noise. In this case, the NM coefficients of the optimum filter, which maximize signal to clutter noise ratio (SCNR), is also represented by

(1). However, \mathbf{R} is now interpreted as the clutter plus noise covariance matrix

$$\mathbf{R} = \mathbb{E} \left\{ (\mathbf{c} + \mathbf{n})(\mathbf{c} + \mathbf{n})^H \right\} \quad (3)$$

where \mathbf{c} and \mathbf{n} denote clutter and noise vectors, respectively. The subscript H denotes complex conjugate transpose (Hermitian transpose) operation. The main disadvantage of STAP is the computational burden for \mathbf{R}^{-1} .

3 Time-domain Backprojection

In SAR processing, backprojection refers to a linear transformation from the radar echo to a SAR image. The superposition of backprojected radar echo to reconstruct the illuminated scene (x_0, r_0) is represented by the integral

$$h(x_0, r_0) = \int_{-\frac{t_i}{2}}^{+\frac{t_i}{2}} g \left(v_{pl} t, \sqrt{(v_{pl} t - x_0)^2 - r_0^2} \right) dt \quad (4)$$

where t_i is the integration time, v_{pl} denotes the speed of the platform, t indicates azimuth-time (slow-time) and $g(x, r)$ represents the range-compressed radar echoes. To save the processing time, it is recommended to process the data on a subaperture and subimage basis, i.e. local processing. Based on this basis, the complete aperture and the full SAR image are segmented in L subapertures and K subimages, respectively. The selection of subaperture and subimage sizes depends strongly on SAR system parameters, required image quality and processing time. However, any selection must ensure the phase error to be smaller than $\pi/8$ (far field condition). The reconstruction of the imaged scene is therefore split into two stages, beam-forming and approximately backprojection.

In the beam-forming stage, from the center of the l -th subaperture x_l , the k -th beam aiming at the center of the k -th subimage is formed by a superposition of all radar echo data in the l -th subaperture. The k -th subimage is then approximately backprojected by the k -th beam. This procedure will be repeated for all subapertures. The full SAR image is retrieved by a coherent combination of all subimages.

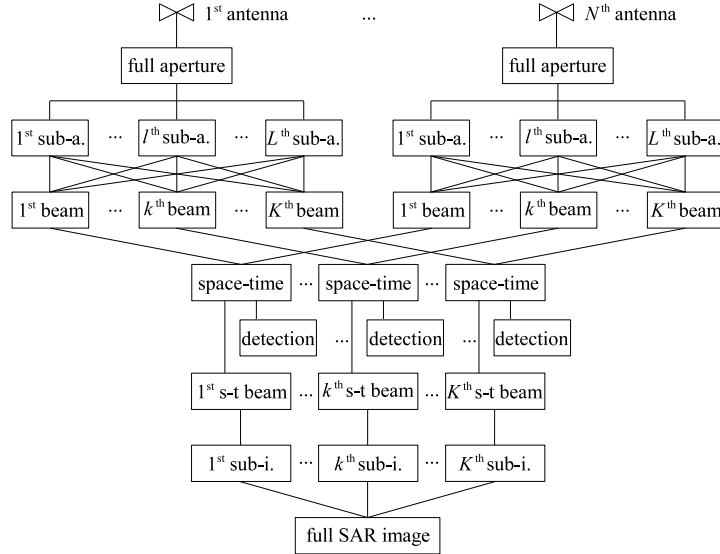


Figure 1: Moving target detection and imaging scheme. In the scheme, the terms sub-a., sub-i., and s-t beam denote subaperture, subimage, and space-time beam respectively.

4 Integrating space-time processing into back-projection process

The integration of the space-time processing techniques, which are mentioned in the previous section, should satisfy several criteria as follows. The integration should lighten the strict demands of DPCA. DPCA might therefore not be considered as a data pre-process as suggested in [3] but a data process after motion compensations. The integration should also reduce the computational burden for \mathbf{R}^{-1} . For these reasons, we propose to integrate the space-time processing techniques into the beam-forming stage in the local backprojection process for detection and imaging moving objects. Fig. 1 sketches the block diagram of the proposal. According to the moving target detection and imaging scheme, the range-compressed SAR data collected by each antenna is processed separately in the beginning of the beam-forming stage. Each antenna creates K beam-matrices with the dimension of $P \times M$ where P is the

number of aperture positions in one subaperture. The k -th beam is formed by summing P rows of the k -th beam-matrix together.

For DPCA implemented on dual-channel SAR data, the k -th beams of the forward-channel and backward-channel, which are at the same positions in space but separated by an integer number of PRI in time, are stacked in a column vector as

$$\mathbf{z} = [z_{11} \cdots z_{1M} \cdots z_{N1} \cdots z_{NM}]^T \quad (5)$$

where $N = 2$. The m -th beam sample of the k -th space-time beam is estimated by

$$\mathbf{y}(m) = \mathbf{w}_m \mathbf{z} \quad (6)$$

where \mathbf{w}_m is a row vector with the dimension of NM and defined by

$$\mathbf{w}_m(n) = \begin{cases} +1 & n = m \\ -1 & n = m + M \\ 0 & \text{elsewhere} \end{cases} \quad (7)$$

Since DPCA is performed on the beams, the effects of the motion errors, which can lead to the poor performance of DPCA, are minimized.

For STAP, the m -th beam sample of the k -th space-time beam is also found from (5). However, the optimum weights \mathbf{w}_m are estimated by (1). The dimension of the clutter plus noise covariance matrices in (1), i.e. $NM \times NM$ decided by the number of the considered antennas and size of subimages. For a small size of subimages, the computational cost for \mathbf{R}^{-1} will be reduced significantly compared to the case where the dimension of the covariance matrices is decided by the number of antennas and the range samples yielded by each antenna. The number of STAP operations for the full SAR aperture is also reduced to a factor of P due to the combination of the aperture positions in one subaperture.

For moving target detection, two hypotheses on \mathbf{z} are given: a moving object exists (hypothesis \mathbf{H}_1) or no moving object exists (hypothesis \mathbf{H}_0) in the processed SAR scene (subimage). If Λ is a detection threshold, the Likelihood Ratio Test (LRT) for moving target detection is given by

$$\begin{aligned} \mathbf{H}_1 : |\mathbf{y}(m)| &\geq \Lambda \\ \mathbf{H}_0 : |\mathbf{y}(m)| &< \Lambda \end{aligned} \quad (8)$$

The space-time beams with clutter suppression can be used further for imaging the moving objects. For UWB SAR, focusing moving targets with NRS is performed in the subimage formation stage.

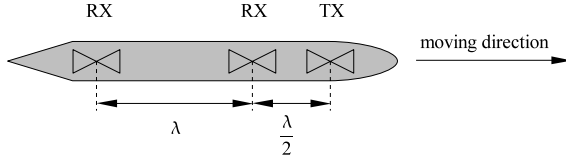


Figure 2: LORA antenna array. λ denotes the wavelength.

5 Simulation results and evaluation

In this section, we demonstrate the proposed integration of the space-time processing techniques into the backprojection process. The reference system for simulations is LORA operating in the frequency range of 200 – 800 MHz. For GMTI purposes, this system is configured as a bistatic SAR system with three antennas (one transmits and two receive simultaneously) and uses the frequency range of 307.2 – 332.8 MHz. Fig. 2 plots this arrangement. With the given element spacing, the displacement of the phase center of the forward and backward antenna is approximately $\lambda/2$, i.e. five aperture positions with LORA parameters. In the simulation, the ground scene is simulated by one arbitrary moving object. The object is point-like scattering and its radar cross section (RCS) is normalized to $\sigma = 1$. The ground clutter is simulated by random stationary point targets spreading over all ground scene. The RCSs of these stationary targets vary in the range $0 < \sigma \leq 4$. The thermal noise is assumed to be AWGN with the noise level is –20 dB. Fig. 3.a plots an example of the beams which are formed only by the forward-channel SAR data. It is almost impossible to detect the moving target from the surrounding ground clutter and noise. Fig. 4.a shows the SAR image reconstructed from the forward-channel beams without space-time processing. No image of the moving target is achieved since it is totally hidden by the ground clutter.

In the first demonstration, we apply DPCA on dual-channel SAR data according to the following procedures. The forward-channel SAR data is delayed by five aperture positions to achieve the transmitted and received pulses at the same position in space but separated in time. The beams are formed separately before stacked into the column vector \mathbf{z} . The subtraction in DPCA is performed by (6) where the weighting vector to perform this subtraction \mathbf{w}_m is given by (7). An example of the space-time beams formed by the dual-channel SAR data with DPCA is plotted in Fig. 3.b. If the detection threshold is set, for example $\Lambda = -6$ dB, the moving object is detected. The

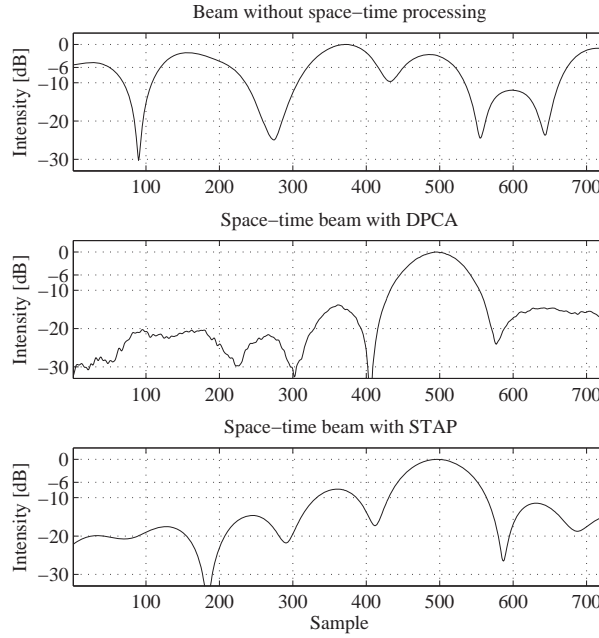


Figure 3: The beams with and without space-time processing. (a) forward-channel beam, i.e. no space-time processing, (b) space-time beam with DPCA, (c) space-time beam with STAP.

image of the moving object, a point-like scattering, is reconstructed from these space-time beams and shown in Fig. 4.b. The noise can be seen clearly in the SAR image. This can be explained by the subtraction in DPCA which also subtracts a part of the signal, especially for slow moving targets such as boat, ferry or ship.

In the next demonstration, STAP is implemented on the same dual-channel SAR data but we do not need to delay the forward-channel like DPCA. For demonstration purposes, the signal behavior and the clutter plus noise covariance matrix estimation are not discussed. We assume that such knowledge is available. The beams are also stacked and form the column vector \mathbf{z} . The space-time beams are found from (5), however, the optimum weights \mathbf{w}_m is

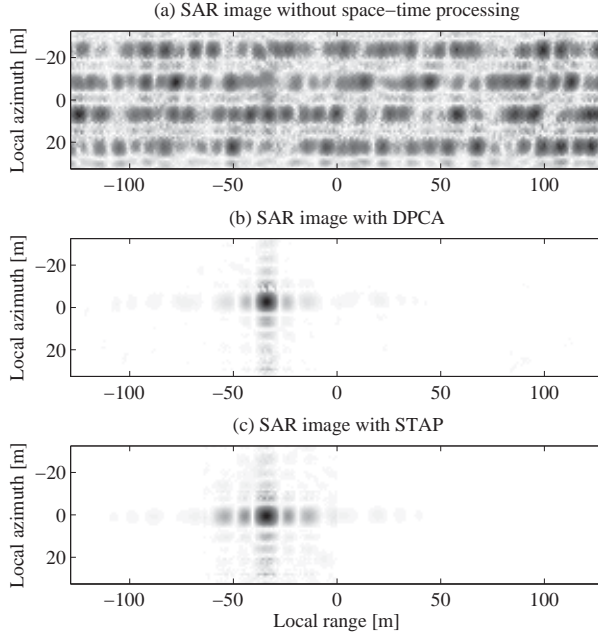


Figure 4: SAR image of the moving object reconstructed from the beams with and without space-time processing. (a) no space-time processing, (b) DPCA processing, (c) STAP processing.

estimated by (1). Fig. 3.c sketches an example of the space-time beams formed by the dual-channel SAR data with STAP. Since the knowledge of the covariance matrices is available, the ground clutter and noise are almost completely suppressed. The moving object can be detected with the same detection threshold $\Lambda = -6$ dB. The SAR image of the object is shown on Fig. 4.c.

6 Conclusion

In this paper, we present a possibility to integrate space-time processing techniques into time-domain backprojection process. DPCA and STAP are two

considered space-time taxonomies. Simulated results indicate that the integration offers reliable detection and provides SAR images of the detected moving objects.

References

- [1] M.I. Skolnik, *Radar Handbook*, 2nd ed. New York, NY: McGraw-Hill, 1990, ch. 16, pp. 8–17.
- [2] L.E. Brennan, L.S. Reed, “Theory of adaptive radar” *IEEE Trans. Aerosp. Electron. Syst.*, vol. AES-9, no. 2, pp. 237–252, 1973.
- [3] V.T. Vu, T.K. Sjögren and M.I. Pettersson, “Fast detection of moving targets in multi-channel ultrawideband SAR,” *EURAD 2009*, Roma, Italy, Sept. 2009, pp. 218–221.
- [4] S. Barbarossa and A. Farina, “Space-time-frequency processing of synthetic aperture radar signals,” *IEEE Trans. Aerosp. Electron. Syst.*, vol. 30, no. 2, pp. 341–358, 1994.
- [5] M.I. Pettersson, “Detection of moving targets in wideband SAR,” *IEEE Trans. Aerosp. Electron. Syst.*, vol. 40, no. 3, pp. 780–796, 2004.

ABSTRACT

This dissertation presents practical issues in Ultrawideband – Ultrawidebeam (UWB) Synthetic Aperture Radar (SAR) signal processing and crucial applications developed on UWB SAR. In the context of this dissertation, UWB SAR refers to the SAR systems utilizing large fractional bandwidth signals and synthesizing long apertures associated with wide antenna beamwidths. On one hand, such specific systems give us opportunities to develop unique applications. On the other hand, signal processing for data collected by these systems is very challenging and therefore requires much effort due to their characteristics. The research results presented in this thesis are divided into two parts: signal processing and application.

In the signal processing part, the tools supporting the UWB SAR system design and evaluation are introduced. They include an Impulse Response Function in UWB SAR imaging (IRF-SAR), azi-

muth and range resolution equations for UWB SAR, and a definition of UWB SAR quality measurements. Pre-processing, processing and post-processing for UWB SAR are also topics that will be examined in the signal processing part. The processing is here defined by SAR algorithms. With this definition, the pre-processing refers to RFI suppression approaches whereas the post-processing implies apodization or sidelobe control methods.

In the application part, Ground Moving Target Indication (GMTI) is selected for study due to its interest to both military and civilian end-users. The GMTI technique developed for UWB SAR relates to the moving target detection by focusing technique which can be combined with the space-time processing such as Displaced Phase Center Antenna (DPCA) and Space-Time Adaptive Processing (STAP).

